Investigation of the core-halo structure of the neutron-rich nuclei ^{6}He and ^{8}He by intermediate-energy elastic proton scattering at high momentum transfer

Farouk Aksouh

To cite this version:

Farouk Aksouh. Investigation of the core-halo structure of the neutron-rich nuclei ^{6}He and ^{8}He by intermediate-energy elastic proton scattering at high momentum transfer. Nuclear Theory [nucl-th]. Université Paris Sud - Paris XI, 2002. English. NNT : . tel-00006027

HAL Id: tel-00006027
https://theses.hal.science/tel-00006027
Submitted on 7 May 2004

Investigation of the core-halo structure of the neutron-rich nuclei ^6He and ^8He by intermediate-energy elastic proton scattering at high momentum transfer

Farouk Aksouh

28th October 2003

Contents

1 INTRODUCTION **9**
- 1.1 Density distribution of nuclear matter in nuclei . . . 9
- 1.2 Proton elastic scattering . . . 10
- 1.3 Halo nuclei - A new phenomenon of nuclear structure . . . 10
- 1.4 Motivation of the present study . . . 13

2 EXPERIMENTAL ASPECTS **17**
- 2.1 Experimental requirements . . . 17
- 2.2 Production of the ^6He and ^8He beams . . . 20
- 2.3 Setup of the experiment S174 at Cave B (GSI) . . . 23
  - 2.3.1 The multiwire proportional chambers . . . 23
    - 2.3.1.1 Description . . . 24
    - 2.3.1.2 Installation and mechanical alignment . . . 24
    - 2.3.1.3 Readout . . . 26
    - 2.3.1.4 Online calibration system - Test events . . . 26
    - 2.3.1.5 MWPCs calibration . . . 26
  - 2.3.2 The liquid hydrogen target . . . 27
    - 2.3.2.1 Target setup description . . . 28
    - 2.3.2.2 Operation principle . . . 29
    - 2.3.2.3 Performance . . . 30
  - 2.3.3 The recoil particle scintillator wall - RPW . . . 30
    - 2.3.3.1 Description . . . 30
    - 2.3.3.2 Calibration . . . 33
  - 2.3.4 The scattered particle scintillator wall - SPW . . . 35
    - 2.3.4.1 Description . . . 35
    - 2.3.4.2 Calibration . . . 35
  - 2.3.5 The ALADIN magnet . . . 36
- 2.4 Beam particles charge identification . . . 36
- 2.5 Trigger logic . . . 36

3 DATA ANALYSIS AND EXPERIMENTAL CROSS SECTIONS **39**
- 3.1 Analysis of the scintillator walls . . . 39
- 3.2 Analysis of the MWPCs . . . 39
  - 3.2.1 Angle determination . . . 39
    - 3.2.1.1 Scattering and recoil angles . . . 39
    - 3.2.1.2 Azimuthal angles . . . 41
  - 3.2.2 Vertex coordinates . . . 41
- 3.3 Angular distribution of elastic events . . . 43
  - 3.3.1 Selection of elastic events . . . 43
  - 3.3.2 Background subtraction . . . 44

3.3.3 Dependence of the dN/dt on the tracking quality 45
3.4 Extraction of the differential elastic cross section 46
3.4.1 Target density 46
3.4.2 Target thickness 47
3.4.3 Number of incident particles 48
3.4.4 Solid angle correction 48
3.4.5 MWPCs efficiency determination 49
3.4.6 Differential elastic scattering cross sections 50

4 RESULTS ON THE RADIAL SHAPE OF THE $^{6,8}HE$ NUCLEI AND THEORETICAL INTERPRETATION 53
4.1 Theoretical description 53
4.2 The nuclear matter distribution ρ_m and its first moment R_m 54
4.2.1 Definition 54
4.2.2 Phenomenological parametrization of ρ_m 55
4.2.2.1 The Woods-Saxon (WS) parametrization 55
4.2.2.2 The symmetrized Fermi (SF) parametrization 55
4.2.2.3 The gaussian - halo (GH) parametrization 55
4.2.2.4 The gaussian - gaussian (GG) parametrization 56
4.2.2.5 The gaussian - harmonic oscillator (GO) parametrization 56
4.3 Description of the fit procedure 56
4.3.1 Fitting with one experimental data set 57
4.3.2 Fitting with combined experimental data sets 57
4.3.3 Uncertainty on the results 58
4.4 Results for ^6He 58
4.4.1 Results for parametrizations which have a common description for all nucleons 58
4.4.2 Results for parametrizations which allow for a separate description of core and halo nucleons 63
4.4.3 Results discussion 67
4.5 Results for ^8He 72
4.5.1 Results for parametrizations which have a common description for all nucleons 72
4.5.2 Results for parametrizations which allow for a separate description of core and halo nucleons 79
4.5.3 Results discussion 81
4.6 Test of theoretical model calculations by the present data 86
4.6.1 Few-body calculations 86
4.6.2 Boson dynamic correlation model 88
4.6.3 Refined resonating group method 88

5 CONCLUSION AND PERSPECTIVES 91

Bibliography 93

A Coordinate determination 97

B Error determination on θ_S and t 101

C Data acquisition 105
C.1 Electronics scheme 105
C.2 Electronics processing 106
C.2.1 Real event cycle 106
C.2.2 Test event cycle 110
C.2.3 Prescaled event cycle (PS) 111

C.2.4 Fastbus system 111

D An overview of the Glauber-Sitenko theory 113
D.1 Nucleon-nucleon profile functions 114
D.2 Profile function Γ 115
D.3 The Coulomb interaction 116
D.4 Density corrections 116

ACKNOWLEDGEMENTS

Dear professors, friends and colleagues,

You are so many that I feel I need to thank but as I am restricted in space, I am quite sure I will not be able to mention everyone. I really apologize for this at the beginning. I would like to express you my warm feelings, to you my family, professors, friends all over these years, for your patience, moral support and a lot of stimulation. It is also a pleasure to be able to acknowledge the help of colleagues and friends who assisted me with their advice and criticism.

I would particularly like to thank Prof. Dr. Peter Egelhof for his excellent direction and for providing me an ideal opprtunity for research. You, Peter, have contributed in several important respects to the final form of this work. I learned a lot with your scientific straight style and I appreciate the perfection you apply on all the subjects you touch. You had continuously many suggestions even right before the final publication. I think we have reached here a compromise between perfection and utility. In a thesis, which remains very close to the living frontier of research, there is much that will soon be superseded, much that will maybe found inadequate even by the time of publication.

I am grateful to Prof. Nimet Frascaria for having accepted the presidency of the jury, for her constant smile which was very comforting me during the presentation. I express all my sympathy to Mr. Marek Lewitowicz and Mr. Nicolas Alamanos who have accepted to report on the thesis in spite of their administrative duties and for their critical comments. I am indebted to Dr. Alex C. Mueller for having assisted me during these years and for his kindness and encouraging discussions. My thanks go as well to Mr. Yorick Blumenfeld for his participation in the jury and his critical analysis of the experimental aspects.

I express also my appreciation to Prof. Gottfried Muentzenberg for his hospitality in the KPII group at GSI and for his constant interest in the development of this work. It is a particular pleasure to thank the devoted GSI staff at Darmstadt and the Paris XI University people for their helpfulness, patience and attention during these years.

In writing this thesis, I have had generous help from my colleagues who either have cleared up questions, have provided me with data, or have read through parts of the manuscript. I hope that this work will be found instructive for students and useful for those physicists who are interested to learn more than what is normally published in the international journals. I would like also to thank several authors for allowing me implicitly to use material which they have already published.

Le mot de la fin ...

La thèse est en fait l'aboutissement de toute une vie. Une synthèse du passé qui peut déboucher pour certains vers un futur fructueux. Elle est aussi l'occasion d'un retour sur soi. Je n'ai pas, pour ma part, failli à cette règle. Je revois encore les années d'enfance, le choix tout naturel pour les choses de l'école qui m'a toujours porté vers plus de savoir. Tout d'abord, un amour fou de la microbiologie et des sciences de la vie en général, à travers les travaux de Pasteur et de Claude Bernard. Durant les années de lycée, mon esprit a opéré un changement de cap vers cette fois-ci, la Physique et la connaissance de la Nature avec tout ce que cela renferme de passionnant et de mystérieux. Après le baccalauréat, je revois même quelques proches et amis incrédules à l'idée de me voir choisir une discipline, qui à l'époque et même maintenant d'ailleurs, offre peu de débouchés sûrs dans la société alors que d'autres disciplines plus prestigieuses s'offraient à moi. La poursuite des études par une thèse de doctorat en Physique Fondamentale découle tout naturellement de ce choix, cette soif de connaitre un peu plus ce monde qui nous entoure. A tous ceux qui m'ont accompagné en pensée, je voudrais vous remercier du fond du coeur et vous assurer que j'en suis toujours aussi heureux malgré la réalité de la vie quotidienne et ses petites contrariétés parfois dures.

Chapter 1

INTRODUCTION

1.1 Density distribution of nuclear matter in nuclei

Ever since the nuclear physics started evolving, the study of the spatial extent of atomic nuclei through the radial distribution of nuclear charge and matter has been one of the major research topics and it still remains challenging. The physical extent of every object is an important concept and it is our natural desire to classify everything we look around in terms of size, weight etc ... Despite this simple motivation, the basic properties of any atomic, nuclear or subnuclear system is reflected in its size. For example, the typical atomic size of 1 to 10 Å[1] is a direct reflection of the electromagnetic interaction strength and the elementary electric charge e.

Before 1911, based on Thompson's atomic model, the atom was believed to be a neutral system of a typical size of around few Å consisting of negatively (electrons) and positively (protons) charged particles. Sir E. Rutherford, who was the first to reject this idea, demonstrated experimentally that the positive charge and also the mass of an atom is concentrated in an extremely tiny nucleus of a typical size of about few fermis[2] surrounded by an electronic cloud which defines the atomic scale. He performed his famous pioneering experiment of 5 MeV α elastic scattering on a gold foil in 1911 [1, 2] and by developing a simple scattering model based on the Coulomb interaction, determined for the first time the Au nucleus size [3].

Since then, following this experimental method, subsequent systematic studies on stable nuclei have been done with most of them based on electron scattering. According to our present knowledge, most nuclei have a central region of practically uniform distribution of protons and neutrons which then decreases relatively sharply. It can be well parametrized by a Woods-Saxon formula :

$$\rho(r) = \frac{1}{1 + exp(\frac{r-R}{a})} \tag{1.1}$$

where the radius $R = r_0 A^{1/3}$, with $r_0 = 1.2 fm$, is the value of r for which the density is the half of the one at $r = 0$, and the diffuseness a is a measure of the surface thickness, A being the isotope mass number. A plot of the density distribution of nuclear matter is displayed in figure 1.1 with different values of R and a showing their influence.

The central uniform density of nuclei reflects the nuclear matter incompressibility or "saturation" effect. The latter arises from the fact that both neutrons and protons being fermions obey the Pauli exclusion principle. The sharpness of the nuclear surface is a result of the short range of the strong interaction.

---

[1] angstroem, $1 \text{Å} = 10^{-10} m$

[2] fermi or femtometer, $1 fm = 10^{-15} m$

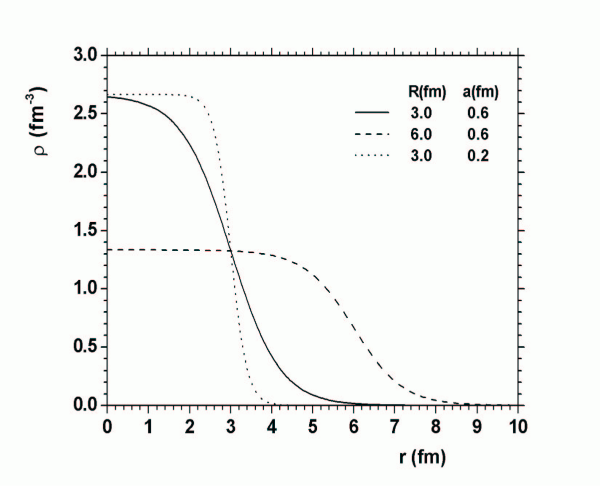

Figure 1.1: *Nuclear matter density distribution parametrized by the Woods-Saxon formula (normalized to unit). The half-density radius R was varied from 3 fm to 6 fm for a=0.6 fm (solid and dashed lines respectively) while the diffuseness a was varied from 0.6 fm to 0.2 fm for R=3 fm (solid and dotted lines respectively).*

1.2 Proton elastic scattering

In principle, many probes can be used together with several experimental techniques to get information on the size and radial shape of nuclei [4]. These probes can be either electromagnetic such as electrons and muons to study the distribution of nuclear charge, or hadronic such as pions, nucleons and α particles for probing the distribution of nuclear matter. In the present work, one has successfully used the elastic scattering of intermediate energy (0.7 GeV) protons with the aim to deduce the radial density distribution of nuclear matter. Since the $^{6,8}He$ lifetimes are short, 806.7±1.5 ms and 119.0±1.5 ms respectively, the measurement is only possible in inverse kinematics where the He isotopes are used as projectiles bombarding a hydrogen target.

The use of $\sim 1\ GeV$ protons as a nuclear probe started at the end of the 60's [5]. Later experiments [6, 7] on heavy and medium weight stable nuclei showed a typical diffraction pattern (Fig. 1.2) that are governed by the matter density distribution parameters of an equivalent sphere of radius R and surface thickness a (figure 1.3).

The advantage of using intermediate energy protons compared to measurements with relatively lower incident energies is that the proton-nucleus elastic scattering can be accurately described by multiple-scattering theories e. g. the Glauber theory which associates measured cross sections and nuclear matter distributions in a direct way. Experimental data are available in the low energy regime but their analysis suffer from ambiguities in the proton-nucleus interaction potential. To infer the nuclear density distributions from the measured cross sections, calculations use experimental data on the elementary proton-proton (pp) and proton-neutron (pn) scattering amplitudes as input (see Appendix D). Various parametrizations for modeling the nuclear density distributions are used as input, their parameters being varied in order to get the best fit to the experimental cross sections.

1.3 Halo nuclei - A new phenomenon of nuclear structure

Halo nuclei [8, 9, 10, 11] were experimentally observed for the first time in 1985 at Bevalac, Berkeley [12]. The total interaction cross section σ_{int} was measured for a variety of very light isotopes by using a transmission method[3] [13] and unexpected large values were found for some very neutron rich nuclei. Table 1.1 shows the measured values for three He isotopes taken from these measurements together with more recent values deduced from elastic proton scattering. In simple terms, the interaction cross sections obtained for light

---

[3] The total interaction cross section includes all the processes where the particle has made an interaction: elastic and inelastic scattering, nucleon(s) transfer, fragmentation and so on. By comparing the flux of incident and transmitted beams it is then possible to derive the number of projectiles that underwent an interaction.

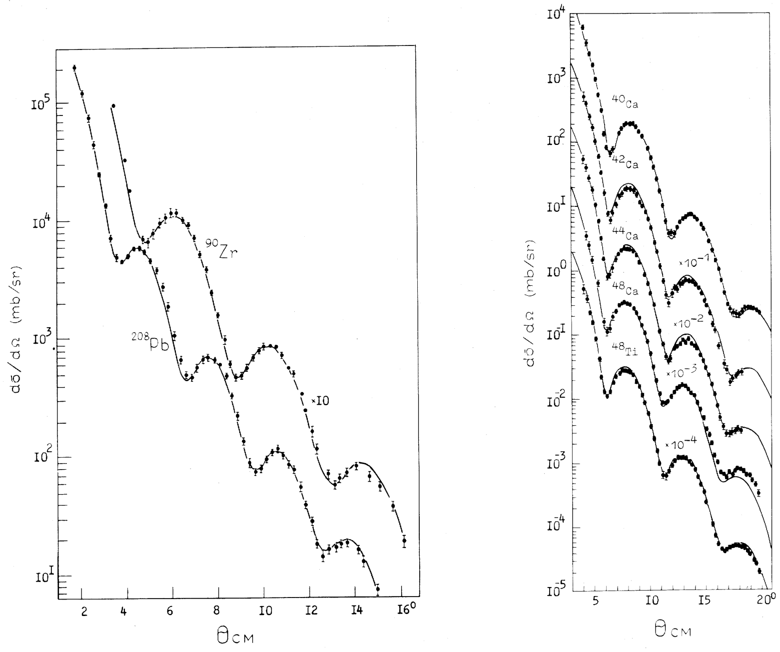

Figure 1.2: *Differential elastic cross section for 1 GeV proton elastic scattering [6] from several stable nuclei*

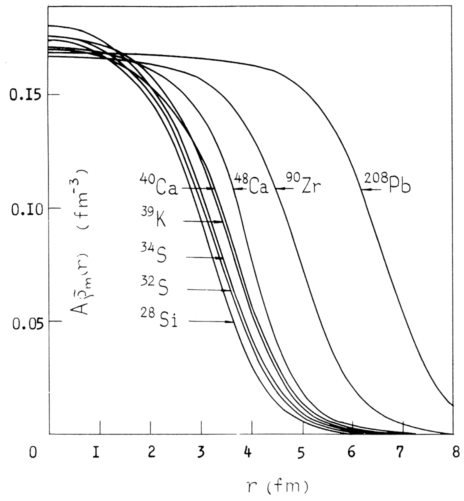

Figure 1.3: *Matter density distributions deduced from elastic proton scattering data [6]*

targets may be used to derive an effective interaction radius:

$$\sigma_{int} = \pi(R_{int,proj} + R_{int,target})^2 \tag{1.2}$$

In other words, one assumes that the projectile and target nuclei, both spherical in shape with respective radii $R_{int,proj}$ and $R_{int,target}$ interact only if their centers are separated by a distance smaller or equal to the sum of their radii.

Nucleus	σ_{int} (mb) on C	σ_{int} (mb) on p
^4He	503 ± 5	131.2 ± 1.5
^6He	722 ± 6	198.9 ± 4.6
^8He	817 ± 6	252.0 ± 4.8

Table 1.1: *Total interaction cross sections of He isotopes measured at 800 MeV/u on a ^{12}C target [13] and from proton elastic scattering at $\simeq$ 700 MeV/u [14].*

Systematic measurements (Fig. 1.4) show that the nuclear radius deviates in some cases from the classical $A^{1/3}$ law which is well established for stable isotopes. This was interpreted in terms of an abnormally extended matter distribution where loosely bound nucleons form a halo around a compact core. In the particular case of $^{6,8}He$ where an α cluster is assumed to be the core, the remaining neutrons (two and four respectively) are characterized by a relatively lower matter density as compared to the normal nuclear matter in stable nuclei. The corresponding "diluted" wave functions indicate that the probability to find a "halo" neutron outside the core is high compared to the situation of a stable nucleus. As example, the halo radius of ^{11}Li of 6.54(38) fm [15] is practically equal to the matter radius of ^{208}Pb (Fig. 1.3 p.11) despite it has 20 times less nucleons.

Consequently, low values of binding energy were theoretically expected and experimentally verified. Table 1.2 shows results for the two-neutron removal energy, S_{2n}, taken from reference [17] which may be compared with the one-neutron removal energy $S_n \simeq 8MeV$ in the most stable nuclei. It turns out that the halo phenomenon can only be understood in terms of quantum mechanics where tunneling effects are predicted and observed for microscopic systems. Since the valence nucleon(s) have a very low binding energy, according

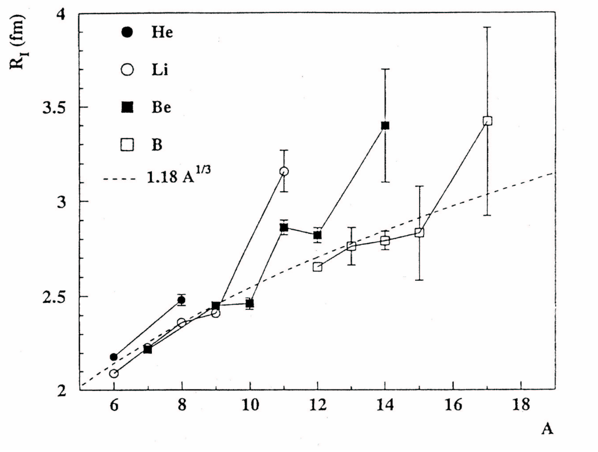

Figure 1.4: *Interaction radii derived from high energy total interaction cross section measurements [12, 13, 16]*

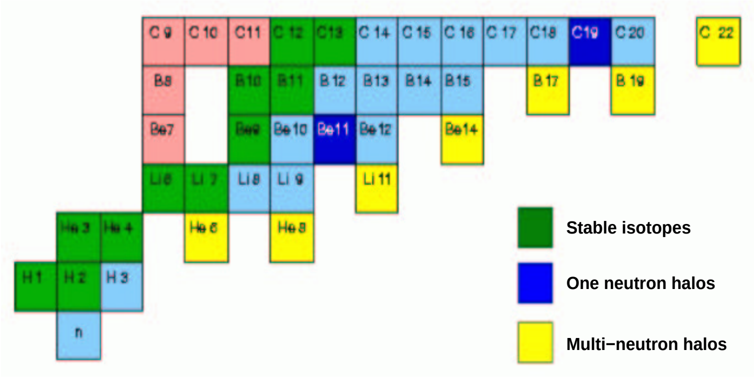

Figure 1.5: *Chart of nuclides showing the stable isotopes (green) and the radioactive nuclei among which were identified one neutron (dark blue) and multi-neutron (yellow) halos (see details in text)*

to the uncertainty principle, they have then more probability to be far away from the core and remain there for a relatively long time.

Nucleus	S_{2n} (keV)
^{6}He	973 ± 1
^{8}He	2139 ± 1
^{11}Li	295 ± 27
^{14}Be	1340 ± 110

Table 1.2: *Experimental two-neutron removal energy for several neutron halo nuclei [17].*

A chart of the lightest nuclides is shown in figure 1.5. The nuclear charge number Z identifies the element and increases in the vertical axis while the horizontal axis corresponds to increasing number of neutrons N. Thus one row contains all the possible isotopes for a given element: as an example, Lithium 11 (^{11}Li) contains 3 protons and 8 neutrons. The stable isotopes, in green, occupy the central region where N$\simeq$Z and are characterized by the largest binding energies compared to the other isotopes hence this region is also called "stability valley". Below this region, one finds the neutron rich elements (light and dark blue, yellow), less stable, which convert into more stable species by β decay. Among them are the neutron halo nuclei : ^{11}Be and ^{19}C are one-neutron halo nuclei, ^{6}He and ^{11}Li are examples of two-neutron halos while ^{8}He is a particular case with four valence neutrons. The nuclei located (pink boxes) above the valley of stability are proton-rich and undergo β^{+} decay to convert into more stable nuclei.

The main feature of ^{6}He concerns its internal structure: the ^{5}He isotope, which would contain one fewer neutron, is unbound, meaning that its two protons and three neutrons will not hold together as a nucleus. Thus ^{4}He and the two neutrons are bound as a three-body system, also called "borromean[4]" system, that splits up if anyone of the three particles is taken away. This fact shows the importance of the pairing [18] of the di-neutron system for the binding of ^{6}He.

From the theoretical point of view ^{6}He is a good candidate for understanding the three body structure (α, n, n). The reason is that the α-n and n-n interactions needed as input in the calculations are well known [19]. This is in contrast with another well studied borromean system, ^{11}Li - formed by a ^{9}Li core and two neutrons - where the ^{9}Li-n interaction is not well known. Hence ^{6}He may serve as a benchmark for the other borromean systems.

---

[4] Refers to Princes of Borromeo, Lake Maggiore, Northern Italy. Their heraldic symbol represents three inseparable rings.

A number of experimental works concerning ^6He and ^8He were performed in the last 17 years since it was possible to produce and transport good quality radioactive beams [20, 21]. The β delayed deuteron emission from ^6He [22, 23] , was interpreted [23] to result from the di-neutron system in an S state. β decay for ^6He and ^8He was also measured [24, 25]. In particular, the results obtained in the β-delayed triton branch from ^8He which originates from a 9.3 MeV resonance in ^8Li indicated that the ^8He ground state has a large overlap with the (α+t+n) structure in ^8Li [26]: this idea supports the (α+4n) picture of ^8He. Fission [27] and fusion cross sections [28, 29, 30] induced by ^6He beams on different targets were measured and the enhanced observed values were interpreted as a signature of an extended matter distribution.

Scattering and reaction experiments are performed with $^{6,8}He$ in inverse kinematics where the probed radioactive nucleus is the projectile and the target being made from a stable material. An attempt to test the ^6He internal wave function was made by transfering two neutrons to ^4He, namely the $^4He(^6He,^4He)$ reaction, at 151 MeV [31], 29.6 MeV and 40 MeV [32]. While Ter-Akopian et al. [31] concluded that this channel is 100% due to the contribution from the "di-neutron" configuration, Raabe et al. [32, 33] found that the exchange process is more complex than the transfer of a single 2n-cluster which confirms that the internal structure of ^6He is more complicated than a di-neutron coupled to the ^4He core. Few nucleons transfer reactions were performed on ^8He at low energy, e. g. (d,p) [34], (p,t) and (p,d) reactions [35], as well as charge exchange reaction (p,n) on ^6He [36].

The fragmentation of $^{6,8}He$ at low [37, 38] and high [39, 40, 41, 42, 43, 44, 45, 46] beam energy was also studied in order to get information on their internal structure. The breakup can be caused by nuclear interactions when low Z targets are used while Coulomb forces dominate the interaction mechanism with high Z targets [45, 46]. The momentum distribution after fragmentation was the main studied observable. According to Heisenberg's uncertainty principle, particles do not have a precise momentum but a range of momenta depending on how they are distributed in space, as reflected by their wave function, i. e. if a halo spans a large distance and a target breaks it away from its core, the momenta of the separated neutrons deviate little from their initial momenta giving therefore narrow distributions as compared to distributions from stable nuclei. Under the assumption that, at high energies, the momentum distribution of the projectile fragment reflects that of the removed nucleons (sudden approximation [47, 48], Kobayashi et al. [49] performed the fragmentation of ^6He on a C target at 400 MeV/u and confirmed the halo structure of ^6He from the observed narrow transverse momentum distribution of ^4He. The same observation was made [39, 41] for the ^5He momentum distribution from the nuclear fragmentation of ^6He on a C target at 240 MeV/u.

Elastic scattering with various probes was also performed both at low [33, 34, 35, 36, 50, 51, 52, 53, 54] and high energy [14, 15, 55, 56]. In particular, the measurement of Neumaier et al. [14], performed with protons as a probe, is the only one available at high energy which has the advantage to offer the simplest and most straightforward theoretical treatment. The radial matter distribution and radii were measured and the halo structure was confirmed by a suitable phenomenological description of the core and halo components of the nuclear matter. However, the data in this case were limited, for experimental reasons, to the low momentum transfer region $0.002 \leq |t| \leq 0.05(GeV/c)^2$ (Fig. 1.6) which implies a sensitivity on the outer boundary of the nucleus. In general, all these measurements, except the one mentioned in reference [31], were sensitive to the outer part of the total wave function which comes from the valence neutron contribution.

1.4 Motivation of the present study

From figure 1.2 (right part), it was shown that a typical diffraction pattern is obtained for the high energy proton elastic scattering on stable nuclei, the position of the first minimum being dependent to first approximation on the size of the diffracting nucleus. Generally speaking, one learns from optical diffraction that the angular position of the first minimum is proportional to λ/R, where λ is the De Broglie wave length associated to the incident photon which depends inversely on the energy, and R is the dimension of the diffracting object. Of course, the p-nucleus scattering at 0.7 GeV is more complex and must be treated as a multiple scattering phenomenon (App. D p.113) but this basic idea still holds in first approximation.

In the special case of a halo nucleus where a strong evidence for a core-halo spatial structure exists, Chulkov et al. [58] have shown, by applying the Glauber approach to the $p(^8He,^8He)$ scattering at 674

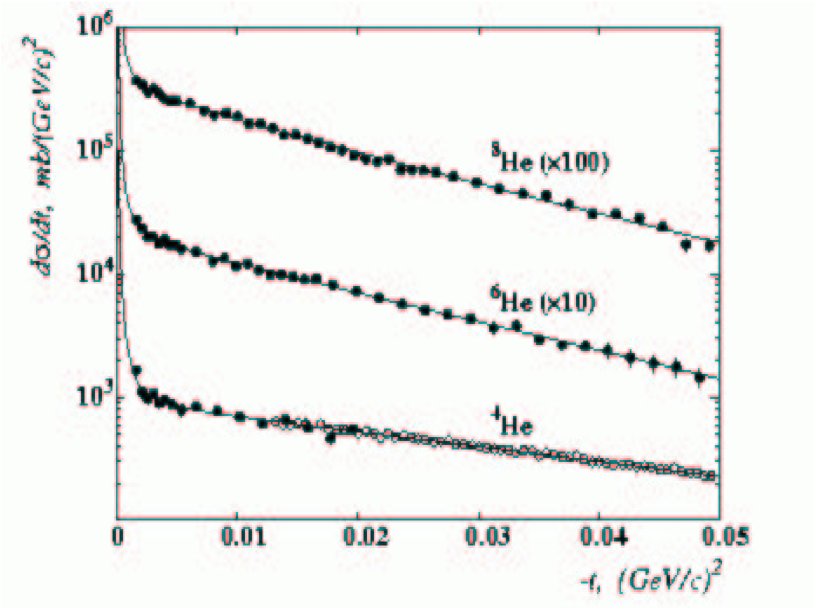

Figure 1.6: *Absolute differential cross sections* $d\sigma/dt$ *versus the four momentum transfer squared for* $p(^4He,^4He)$ *at 699 MeV/u,* $p(^6He,^6He)$ *at 717 MeV/u and* $p(^8He,^8He)$ *at 674 MeV/u elastic scattering (full dots from [14] in inverse kinematics and open dots from [57] in direct kinematics). The lines are result of a fit [55]*

MeV/u, that the position of the first diffraction minimum is sensitive to the size of the nucleus core which might help to learn about the structure of ^8He. Similar calculations of the differential elastic cross sections were performed by using the same scattering approach and applied to $p(^6He,^6He)$ scattering at 717 MeV/u. The cluster orbital shell model approximation (COSMA) described in reference [59] was used to derive the required core and halo density distributions for ^6He and ^8He nucleons.

Figure 1.7 shows the results of Glauber calculations [60] for the $p(^8He,^8He)$ at 674 MeV/u. The differential cross section is displayed versus the momentum transfer squared $-t$. The scale-parameter of the model was varied in order to have a ^8He total matter radius[5] $R_m = 2.52fm$. The COSMA assumptions with a well defined α core lead to an extended distribution of neutrons compared to the protons and especially valence neutrons. Indeed, the proton distribution extends to $R_p = 1.69fm$ and the neutron (including core and halo neutrons) to $R_n = 2.75fm$, while the valence neutron distribution exhibits almost twice the size than that of the protons $R_{n,valence} = 3.10fm$.

In a second calculation (DISSolved), the COSMA parameter was modified in order to obtain a neutron distribution almost equal to that of protons but keeping the same total matter radius for ^8He. The α-core is then completely dissolved which leads to $R_m = R_p = R_n = 2.52fm$. These two calculations represent two extreme descriptions of what might be the reality. They also show that the region of small momentum transfer [14] does not have enough sensitivity to study the inner structure of halo nuclei. A more complete study of its internal structure should examine the region where a possible minimum can be expected by extending the measurement of Neumaier et al. [14] to the region of higher momentum transfer. Besides the data shown in Fig. 1.7, the new experimental measurement should be performed in the range $0.05 \leq |t| \leq 0.3(GeV/c)^2$ which corresponds to the region $15° \leq \theta_{CM} \leq 31°$ in terms of the center-of-mass scattering angle.

The situation of ^6He is similar to that of ^8He. The figure 1.8 shows the results of the two calculations (COSMA, DISS) performed for ^6He. For both calculations, two values of the total matter radius R_m, 2.30 fm from Ref. [14] and a larger one, 2.40 fm, were used in order to get an estimate on the influence of R_m on the differential elastic cross section: it shows clearly that the position of the first minimum is more sensitive to the core radius R_c than to R_m. This observation reasserts the idea that a better determination of the elastic scattering distribution around the region of the first minimum will lead to a better determination of the internal spatial structure of these isotopes.

---

[5] The radii mentioned in this work are root-mean-square (rms) radii as defined in section 4.2 p.54

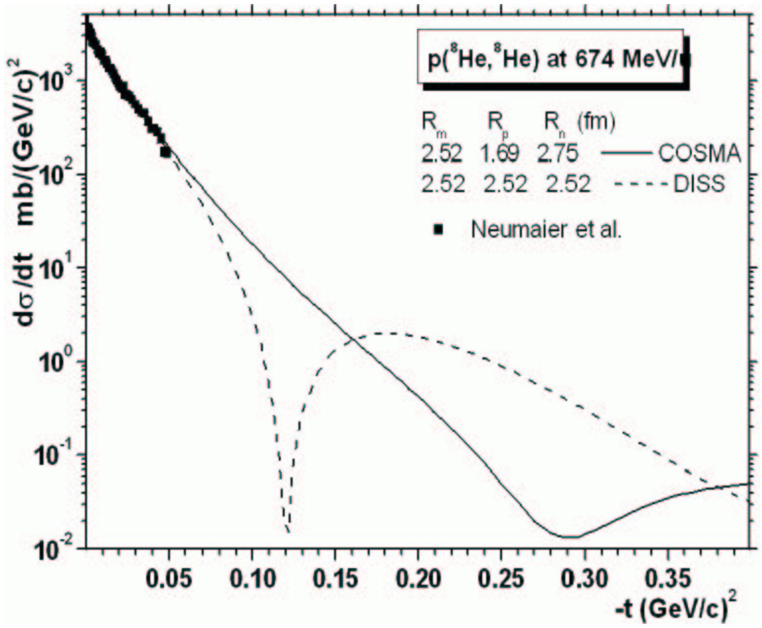

Figure 1.7: *Calculated differential elastic cross section for the* $p(^{8}He,^{8}He)$ *scattering at 674 MeV/u. Experimental data (full squares) are taken from reference [14]. The* ^{8}He *nucleus is depicted as an* $\alpha+4n$ *system (COSMA) with spatially well defined core and halo nucleons and as a system where all the nucleons are dissolved (DISS)*

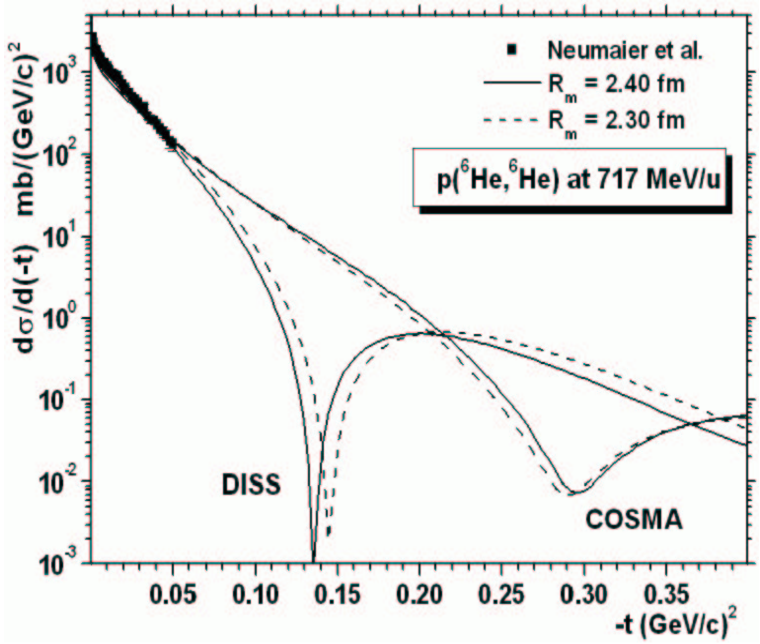

Figure 1.8: *Calculated differential elastic cross section for the* $p(^{6}He,^{6}He)$ *scattering at 717 MeV/u. Experimental data (full squares) are from Neumaier et al. [14]. The* ^{6}He *is depicted as an* $\alpha+2n$ *system (COSMA) with spatially well defined nucleons and as a system where all the nucleons are dissolved (DISS). Two values for the total matter radius were assumed (see text for details)*

Chapter 2

EXPERIMENTAL ASPECTS

2.1 Experimental requirements

The figure 2.1 outlines the principle of a two-body collision in the laboratory frame where all the quantities are experimentally measured. For the case of inverse kinematics, needed to investigate the exotic nuclei, an incident ^{A}He nucleus with a given kinetic energy T_{in} is scattered at an angle Θ_S with a kinetic energy T_S while the recoil target proton is emitted at an angle Θ_R with a kinetic energy $T_R = T_{in} - T_S$. Since the two colliding particles neither reach any excited state nor convert into different nuclei, the energy is transfered only in its kinetic form. If $\mathbf{q}_i$ and $\mathbf{q}_f$ are the ^{A}He initial and final momenta vectors and $q = \| \mathbf{q}_f - \mathbf{q}_i \|$ the momentum transfer, then one can use the second Mandelstam invariant [61]:

$$t = -|q|^2 \tag{2.1}$$

as the quantity used to define the differential cross section $\frac{d\sigma}{dt}$. For the elastic scattering case, this is expressed as:

$$\mid t \mid = 2M_p T_R \tag{2.2}$$

It is also related with a simple form to the CM scattering angle Θ_{cm} as:

$$t = (\cos\Theta_{cm} - 1) \cdot \frac{\{s - (M_{He} + M_p)^2\} \cdot \{s - (M_{He} - M_p)^2\}}{2s} = C \cdot (\cos\Theta_{cm} - 1) \tag{2.3}$$

Here M_{He} and M_p are the masses of the projectile and recoil proton respectively and s the first Mandelstam variable given by $s = M_{He}^2 + M_p^2 + 2M_p \cdot (M_{He} + T_{in})$. C is then a constant which depends only on M_{He}, M_p and T_{in}.

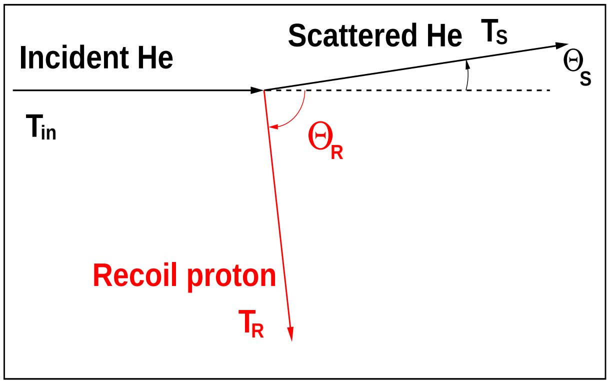

Figure 2.1: *Two-body elastic scattering sketched in the laboratory frame*

From the energy and momentum conservation laws one can easily derive the relationship between the different kinematical parameters as shown in figure 2.2. The goal of the present measurement is, as was previously discussed (see Sec. 1.4 p.13), to extend the measurements of Neumaier et al. [14] to the region of momentum transfer $0.05 \leq |t| \leq 0.3 (GeV/c)^2$ for the reactions $p(^8He,^8He)$ and $p(^6He,^6He)$. In the case of $p(^8He,^8He)$ at 671 MeV/u this signifies a measurement in the range $15^\circ \leq \Theta_{cm} \leq 31^\circ$ which corresponds to $67.0^\circ \leq \Theta_R \leq 78.6^\circ$ for the recoil proton and $1.56^\circ \leq \Theta_S \leq 3.15^\circ$ for the scattered projectile in the laboratory system. For $p(^6He,^6He)$ scattering at 717 MeM/u, the measurement has to be performed in the range $12^\circ \leq \Theta_{cm} \leq 29.8^\circ$ which corresponds to $68.1^\circ \leq \Theta_R \leq 81^\circ$ and to $1.58^\circ \leq \Theta_S \leq 3.85^\circ$ in the laboratory frame (Fig. 2.2).

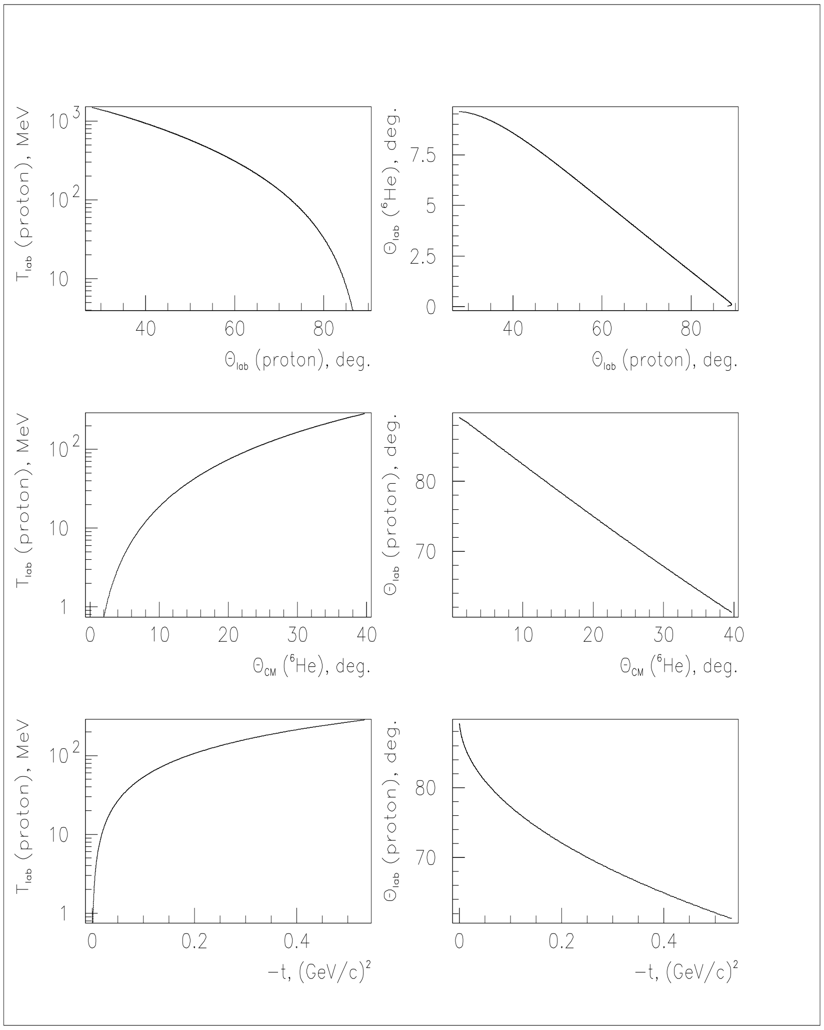

Figure 2.2: *Interplay between different kinematical parameters for $p(^6He,^6He)$ scattering at 717 MeV/u. In the two figures on the top are plotted the proton lab. kinetic energy $T_{lab}(proton)$ and the lab. scattered projectile angle $\Theta_{lab}(^6He)$ versus the proton lab. angle $\Theta_{lab}(proton)$. On the middle are shown the proton lab. kinetic energy and angle versus the CM scattering angle $\Theta_{CM}(^6He)$. On the bottom, the same variables as in the middle are displayed versus the four-momentum transfer squared $-t$.*

The comparison of these data shows that for our requirement, the elastic proton scattering on ^6He and ^8He have almost similar kinematical characteristics: a very forward peaked scattered projectile - $1.5^\circ \leq \Theta_S \leq 4^\circ$ - and laterally emitted recoil protons - $65^\circ \leq \Theta_R \leq 85^\circ$ - in the laboratory frame.

At intermediate energies, ^6He and ^8He can reach all possible excited states. Fortunately, these states are particle unbound (life-times less than $10^{-21} sec$) i. e. the nuclei can not hold all their nucleons together. The inelastic scattering of ^6He leads then to breakup in the following channel:

$$^6He \longrightarrow ^4He + 2n \qquad (2.4)$$

while the ^8He leads to:

$$^{8}He \longrightarrow ^{6}He + 2n \longrightarrow (^{4}He + 2n) + 2n \tag{2.5}$$

$$^{8}He \longrightarrow ^{4}He + 4n \tag{2.6}$$

Other reaction channels like one-two nucleon transfer are to be expected. The discrimination of these events needs the use of a magnetic spectrometer after the interaction in the target (Sec. 2.3.5 p.36) prior to their detection in a scintillator wall (Sec. 2.3.4 p.35).

The recoil energy of interest starts from low values typically 30 MeV and extends to intermediate energies around 200 MeV which enabled us to use a thick target in order to compensate for the relatively low beam fluxes[1]. Taking into account the low value ($\sim 0.01\ mb/sr$) of the expected cross section at the first diffraction minimum (Figs. 1.7 and 1.8), the expected beam rates, a measurement period of 4 days for each isotope and a statistical error of 5%, a typical target thickness of 10 cm was chosen. Because of the extended target, one has to guarantee a good tracking in order to identify the interaction point (vertex).

A pure liquid hydrogen target was prefered instead of a classical one made of paraffin ($\sim (CH_2)_n$) due to the several limitations arising from the use of the latter. Indeed, in order to subtract the interaction events due to carbon nuclei, the use of a paraffin target demands generally an additional measurement with a pure carbon target which means additional beam time. Finally, the carbon (Z=6) induces much more energy and angular straggling than hydrogen (Z=1) and this point can be an important limiting factor when thick paraffin targets are used.

The angular distribution has to be measured with an optimum angular resolution of $\Delta\Theta_{cm} = 1^\circ$ which corresponds to resolutions of $\Delta\Theta_S = 0.1^\circ (1.7 mrad)$ for the scattered projectile and $\Delta\Theta_R = 0.72^\circ (12.5 mrad)$ for the recoil proton. All the trajectories are tracked by multi-wire proportional chambers (MWPCs) with a position resolution $\Delta x = 150 \mu m$. For the He ions, a typical tracking requires to use two detectors per track separated by a distance of 2m where the particles pass normally air, the angular resolution being then typically $\Delta\Theta_{lab} = (4.3 \times 10^{-3})^\circ = 0.08 mrad$. The recoil protons are tracked by two MWPCs very close to the target and less spaced ($\simeq 24 cm$) in order to limit the energy and angular straggling. The angular resolution is then typically $\Delta\Theta_{lab} = 0.04^\circ = 0.6 mrad$.

The tracking resolution is limited by angular straggling of both colliding particles in the target, of which the thickness is principally defined by count rate considerations and in the sections between the target and the detectors. In order to reduce it one uses generally large bags filled with He gas[2].

A second position sensitive detector (resolution $\Delta x = 1.25 cm$, $\Delta\Theta_{lab} = 0.36^\circ = 6.25 mrad$) with higher efficiency (Sec. 2.3.3 p.30) covering the needed proton large solid angle is placed at $\simeq$ 2m from the target. It can in principle give an additional tracking information, in addition to the energy loss and time-of-flight measurements. The recoil protons emitted at the center of the target (Sec. 2.3.2.1 p.28) traverse then several media : liquid hydrogen, Mylar, air and He gas (Tab. 2.1). If one assumes a negligible influence from the gaseous chambers then the total amount of multiple scattering before reaching the final position sensitive detector is 10.33 mrad for protons emitted at 50 MeV. This calculation considers an intermediate case of low energy protons where the angular straggling is the highest and shows that the tracking on the scintillation wall is still possible. For higher energy protons - 200 MeV protons have a total angular straggling of 2.62 mrad - the situation is much better but for lower energies - 30 MeV gives a straggling of 19 mrad - the tracking is impossible. In any case, the tracking remains possible with the MWPCs. The situation is much better for the scattered He (Tab. 2.2). In the expected angular range, the angular straggling is much smaller than the needed measurement resolution.

The determination of the differential elastic cross section requires a precise measurement of the momentum transfer q. q, t and Θ_{cm} are related in a univocal way meaning that the knowledge of one of these quantities fully determines the two others. It is then possible to express the differential cross section in the three equivalent forms: $\frac{d\sigma}{dq}$, $\frac{d\sigma}{d\Theta_{cm}}$ and $\frac{d\sigma}{dt}$ which was chosen in this work. Once an elastic event is identified, it is

---

[1] For a 3 cm diameter, protons at 30 MeV do not stop in the liquid H2 target while at 10 MeV they stop

[2] Indeed energy loss and angular and energy straggling are due to multiple scattering from interactions between atomic electrons of the projectile and the medium constituents. To limit them, one should use low Z and chemically stable elements (noble gases with high ionization potential) such as helium.

Medium	liquid H_2	Mylar	Mylar	Mylar	Air	He gas
Δx	$15mm$	$100\mu m$	$5 \times 5\mu m$	$125\mu m$	$50cm$	$2m$
$\Delta x(mg/cm^2)$	106.20	13.90	3.48	13.90	64.3	35.70
$\Delta E(MeV)$	2.84	0.17	0.04	0.17	0.74	0.46
$\Delta\Theta_{R,rms}(mrad)$	6.15	6.77	6.92	7.49	9.87	10.33

Table 2.1: *Typical cumulative angular straggling $\Delta\Theta_{R,rms}$ (rms) and specific energy loss ΔE for 50 MeV recoil protons. The thicknesses of the different media (two first rows) are shown in length units and in surface density units.*

Medium	Air	He gas	liquid H_2	He gas
Δx	$1m$	$2m$	$100mm$	$2m$
$\Delta x(mg/cm^2)$	128.6	35.7	708.0	35.7
$\Delta E(MeV/u)$	0.18	0.06	0.35	0.06
$\Delta\Theta_{S,rms}(mrad)$	0.27	0.28	0.33	0.34

Table 2.2: *Typical cumulative angular straggling $\Delta\Theta_{S,rms}$ (rms) and specific energy loss ΔE for 717 MeV/u ^6He ions. The thicknesses of the different media (two first rows) are shown in length units and in surface density units. The contribution from the MWPCs and the Mylar windows was neglected.*

in principle, sufficient to measure only one variable (e. g. T_R, T_S, Θ_R or Θ_S) in order to get the transfered momentum. Despite of these considerations, it was decided to measure all these quantities in order to separate the different interaction channels and to reduce the background, meaning that one determines the angles, energy losses and total energies (time-of-flight) for the scattered projectile and the recoil proton. At this time, the break-up channels were identified and their analysis is still going on. It is worth to mention that the break-up of ^6He and ^8He with a concidence analysis of the recoil nucleus was performed for the first time at high energy during this experiment. Up to now in high energy fragmentation, the fragments are detected only in coincidence with the emitted halo neutrons.

2.2 Production of the ^6He and ^8He beams

The study of nuclei far from the stability valley is a challenge with respect to the actual experimental techniques. No stable target of ^6He or ^8He can be technically produced due to their small lifetimes, so it is clear that one has to perform the proton elastic scattering in the inverse scheme: the ^AHe are produced and conducted towards a hydrogen target. At the present time, the GSI (**G**esellschaft fuer **S**chwer**i**onenforschung, Darmstadt, Germany) is the only installation where radioactive beams can be produced and filtered at high energy ($\sim$ 0.2 to few GeV/u).

First a primary intense ^{18}O[3] beam is developed and accelerated through the UNILAC (Fig. 2.3) linear sections and injected to the SIS (**S**chwer**I**on **S**ynchrotron) to be accelerated at $\simeq$ 820 MeV/u and 730 MeV/u (Tab. 2.3) for the production of ^6He and ^8He respectively. In the slow extraction mode, the SIS is blocked during the acceleration stage and then, when the demanded energy is reached, opened for beam delivery during a time interval ranging from a fraction up to few seconds which results in a typical 'spill' (bunch) structure. It is then directed to a ^9Be fragmentation target which is located at the entrance of the **FR**agment **S**eparator (FRS) [62]. The FRS (Fig. 2.4) is a magnetic spectrometer where heavy ion beams with magnetic rigidities from 5 to 18 Tm can be analyzed in-flight. It consists basically of four independent stages, each consisting of a dipole magnet and a set of quadrupoles before and after the dipole. One should mention that the combination of a high energy, heavy ion beam with a relatively thin production target has an important advantage through the fragmentation mechanism: the reaction products are confined to the very forward directions with velocities very close to that of the beam.

The ^8He (M/Z=4) can be easily separated from other fragmentation products by a simple magnetic analysis despite it is at the maximum rigidity limit of the fragment separator. The ^6He case needs in addition the analysis of the energy loss of the fragments. This is accomplished by the use of a profiled energy

---

[3] ^{18}O is the neutron richest stable oxygen isotope

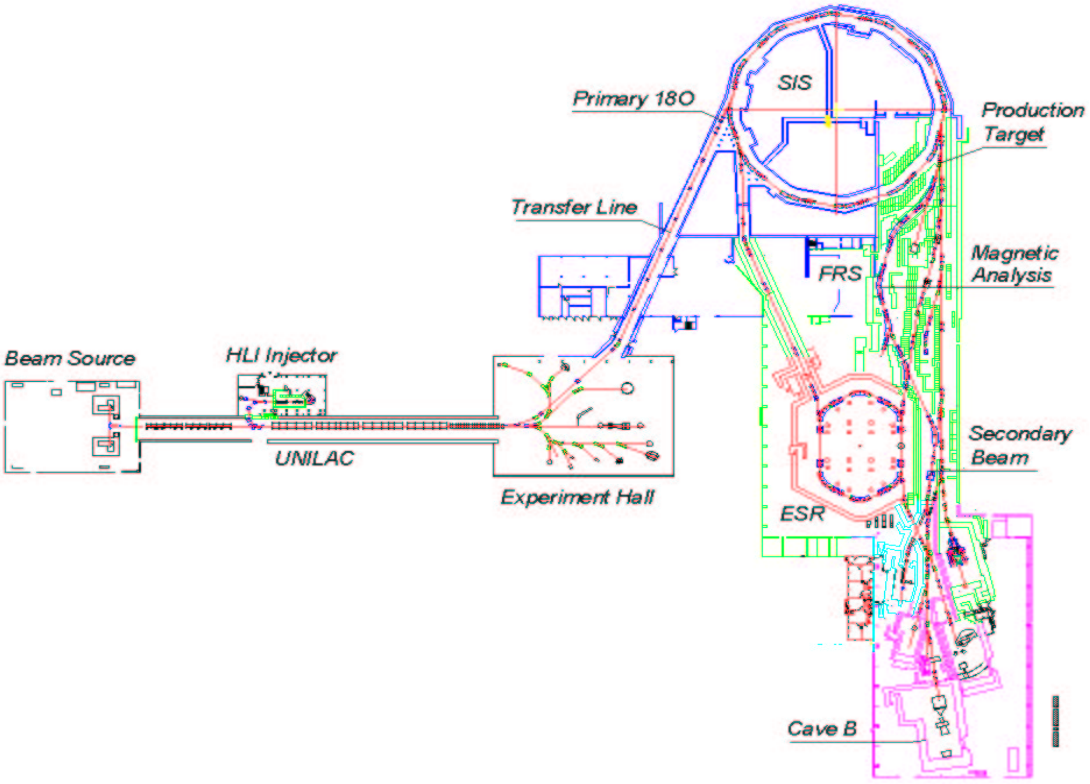

Figure 2.3: *Secondary beam production through the GSI accelerator facility.*

Isotope	$E(^{18}O), MeV/u$	$E, MeV/u$	$B\rho, T/m$
^{6}He	820	717 ± 9	13.9
^{8}He	730	670 ± 9	17.5

Table 2.3: *Incident beam energies at the target (calculated with a Monte-Carlo method [63] assuming a constant primary beam energy)*

degrader made of aluminum located at the dispersive focal plane F_2. The first two dipole stages of the FRS perform an A/Z selection thus the fragments with the same magnetic rigidity are focussed on the same position of the energy degrader. The different atomic energy loss of the ions penetrating the degrader provides the additional selection basis needed for the separation of a selected nuclide ($B\rho - \Delta E - B\rho$ method). An experimental example demonstrating the selection method is presented in the lower part of figure 2.4 taken from reference [64] showing the result of the first and the second extraction. The combination of the two-fold $B\rho$ analysis and the energy loss provided a secondary beam of ^6He with only few contaminants that were subtracted later during the offline analysis (Sec. 2.4 p.36).

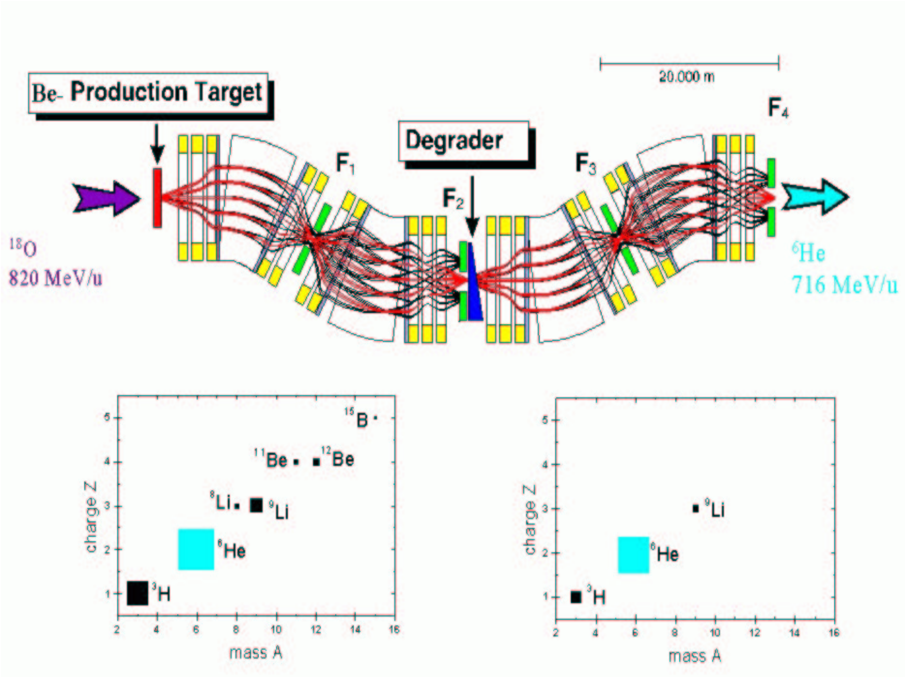

Figure 2.4: *Schematic view of the* ***FR****agment* ***S****eparator (FRS). The isotopic separation principle is illustrated with the experimental conditions for a ^6He beam (from Ref. [64])*

The ^9Be fragmentation target used was about $8g/cm^2$ thick which represents $5.3 \times 10^{23} atoms/cm^2$ and the typical primary ^{18}O intensity was $2 \times 10^{10} particles/sec$. The exotic nuclei passed through the FRS and then traveled about 80 m to the cave B where the experimental setup is installed. Before performing the experiment, one needs to simulate the transport of the secondary beams through all these elements. For this purpose, a Monte-Carlo code, MOCADI [63] including the needed beam optics and the atomic and nuclear interaction processes was used. The table 2.4 resumes the following relevant quantities:

- the production cross section σ_{prod} determined from the EPAX empirical relations ([65], [66])
- the total transmission factor ϵ_{trans} determined from MOCADI [63]
- the expected particle rate Φ_{calc} at the experimental setup
- the measured particle rate Φ_m

Isotope	$\sigma_{prod}(barn)$	ϵ_{trans}	$\Phi_{calc}(pps)$	$\Phi_m(pps)$
^6He	2.19×10^{-3}	0.01	2×10^5	1.9×10^5
^8He	4.21×10^{-5}	0.03	14000	16000

Table 2.4: *Secondary beam production parameters*

Finally, the calculated beam divergency, $\Theta_X \simeq 3.4mrad$ and $\Theta_Y \simeq 6.8mrad$ (Fig. 2.5) is another important reason that requires to have a precise beam particle tracking.

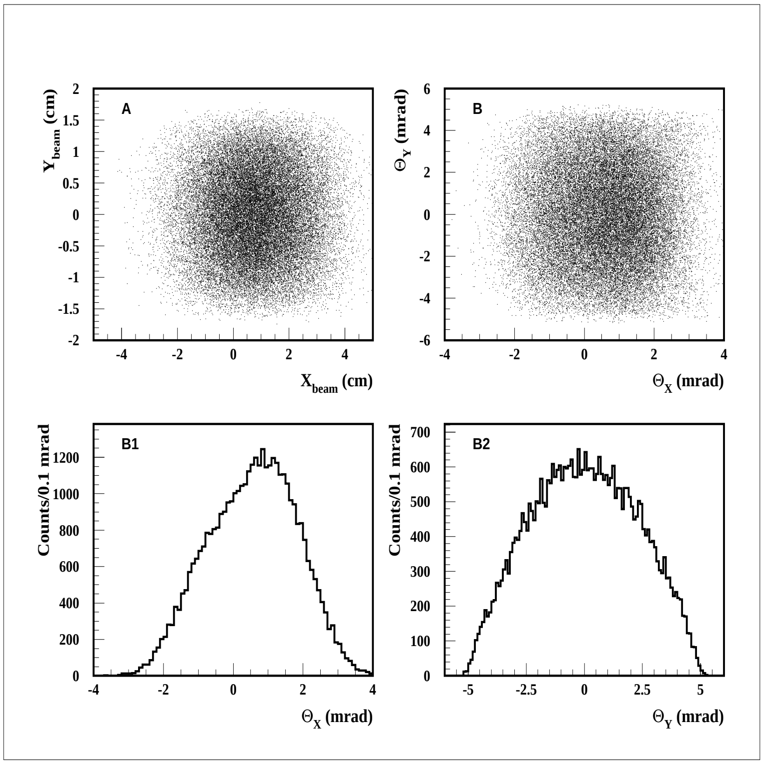

Figure 2.5: *Calculated beam parameters for 717 MeV/u* ^6He *[63] at the entrance of the experimental setup,* $\sim 28cm$ *before reaching the first counter S1. The figure A shows the correlation of the beam coordinates* X_{beam} *and* Y_{beam}*. The figure B shows the correlation of the X and Y component of the incident angle* Θ*. Their distinct spectra in figures B1 and B2, obtained from the projection of the spectrum B, show the beam divergency in both directions.*

2.3 Setup of the experiment S174 at Cave B (GSI)

The setup used for the present measurements is sketched in figure 2.6. The beam projectile nuclear charge Z is determined from the energy loss (ΔE) measured by means of two small and thin scintillators S1 ($5cm \times 6cm \times 1mm$), S2 ($6cm \times 6cm \times 3mm$) and a bigger one, S3 ($20cm \times 20cm \times 2cm$). It is collimated right before interacting at the target by a $20cm \times 20cm \times 1cm$ scintillator with a 2 cm diameter hole at its center (Veto). These four detectors also serve to define the beam trigger (Sec. 2.5 p.36).

The He beam particles are tracked by the MWPCs P1-P2 before interaction and P3-P4 after interaction thus, one is able to determine the lab. scattering angle Θ_S and the interaction vertex position. They are identified after the scattering process via ΔE measurement in S3 and a magnetic analysis using the Aladin dipole magnet and a position sensitive scintillator wall (SPW) behind it: this enables to separate the elastic scattering from beam fragmentation products and other reaction processes.

The proton tracking is performed by the MWPCs P5 and P6 which also serve for the second level trigger (Sec. 2.5 p.36). A position sensitive scintillator wall (RPW) serves for their identification (ΔE and TOF). In addition, three PVC bags (not represented on the figure) filled with He gas at 1 atm are used: two cylindrical ones between chambers P1 and P2, P3 and P4 respectively. The third one was placed between chamber P6 and the recoil particle scintillator wall. They had the purpose to reduce multiple scattering of the He and protons within the experimental setup.

2.3.1 The multiwire proportional chambers

The tracking of beam particles and recoil protons was performed by the use of six MWPCs[4] designed and constructed at PNPI St-Petersburg (Russia). Four are small sized and two, P4 and P6 are bigger in order to cover the large scattering and recoil angular ranges.

---

[4] also called cathode strip chambers (CSC) since the readout is based on cathode strips

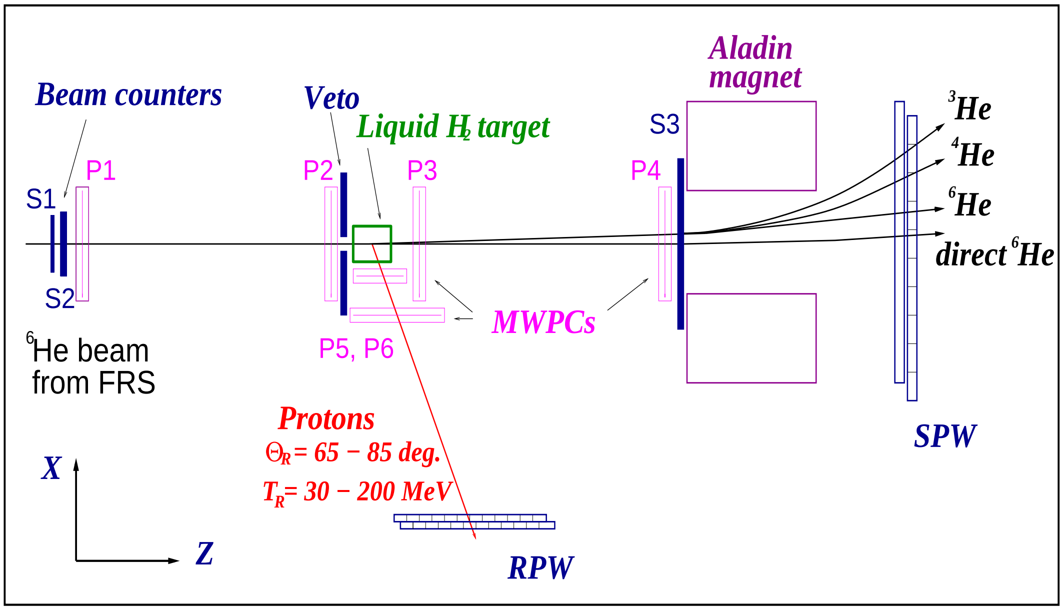

Figure 2.6: *Schematic representation of the S174 experiment. The laboratory coordinates system used is shown in the bottom left corner, the origin being at the center of the target. The direction* $\Theta_R = 75°$ *is used as a guideline to position the recoil arm devices.*

2.3.1.1 Description

Each chamber consists of a closed isolated volume maintained at atmospheric pressure with a permanent gas flow (75 % argon + 25 % CO_2). The gas mixture is realized through a dedicated device built at GSI. The entrance and exit windows are made from $50\mu m$ aluminized Mylar. The MWPC has two coordinate planes, similar in structure and perpendicular to each other, one for each position coordinate X and Y (Fig. 2.7). One coordinate plane is shown in figure 2.8 with two views perpendicular to each other.

It is formed by three planes of thin wires: cathode strip plane, anode plane and cathode plane. It forms a complete independent detector which is able to get the information related to one coordinate, typically X or Y, Z being the direction of incident beam. The typical distance between the cathode and the anode planes is $d = 2mm$, also known as gas gap, and the two coordinate planes within one chamber are separated by typically $6 \times d$ to avoid any electromagnetic induction. The cathode plane wires are grounded while the anode plane wires are set to +1.7 kV. One cathode strip unit is formed by a group of 5 (small chamber) or 6 (big chamber) wires connected electrically to a shaping preamplifier. The anode wires made from gold plated tungsten are $S = 30\mu m$ diameter (except $25\mu m$ for chamber P1) and spaced by $D_S = 2mm$. The cathode and cathode strips planes are made with copper/beryllium wires $W = 50\mu m$ diameter and spaced by $D_W = 0.5mm$; they are stressed perpendicularly to the anode wires. The strip units are then 2 mm wide (2.5 mm for a big chamber) which defines the pitch readout with a periodicity of 2.5 mm (3 mm for a big chamber). The small chambers (P1, P2, P3, P5) have then 64 readout channels for a sensitive area of 16 cm × 16 cm. The big chambers (P4, P6) have 86 channels for an area of 26 cm × 26 cm.

2.3.1.2 Installation and mechanical alignment

Chambers P1, P2 and P3 were aligned on the center of the beam trajectory while chamber P4 was shifted $5cm$ in the direction of positive X in order to cover the solid angle of interest. The beam particles coordinates are later used offline for a final precise zero alignment (Sec. 2.3.1.5 p.26). The chamber P5 was placed parallel to the target lateral window located on the side of negative X in order to have the maximum possible overlap.

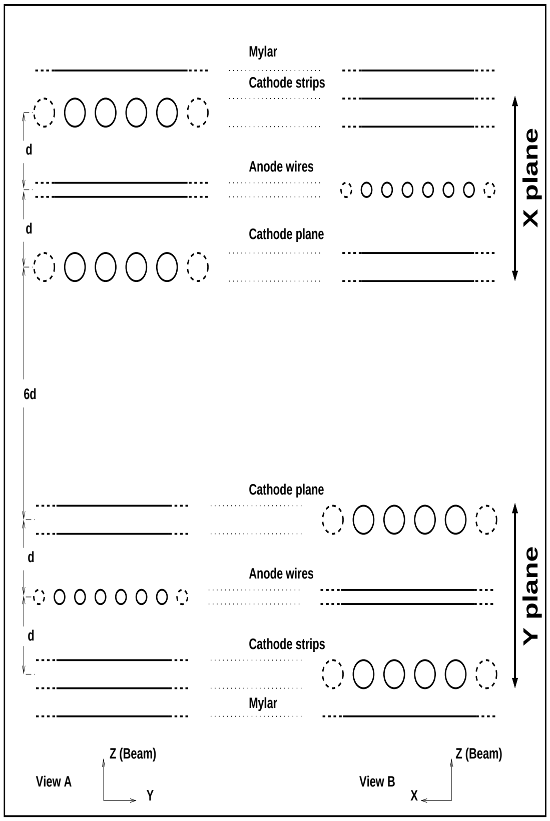

Figure 2.7: *Transversal cut showing the schematic structure of one MWPC. The coordinate planes are similar and only rotated by $\pi/2$ to each other. The chamber sensitive volume is delimited by the Mylar foils.*

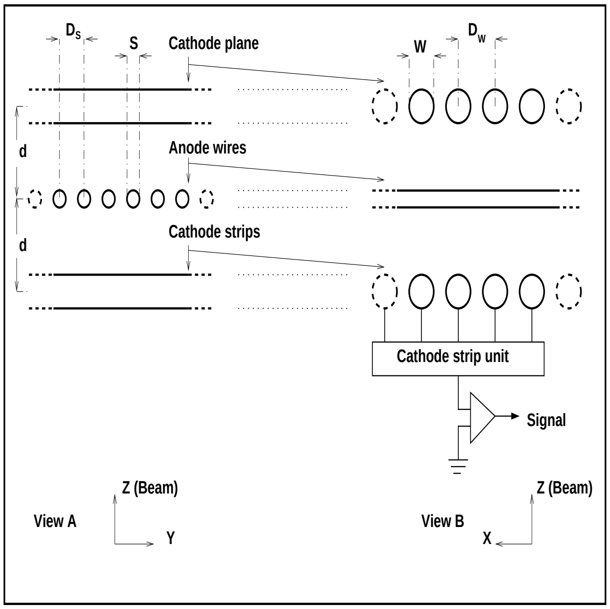

Figure 2.8: *Schematic transversal cut of one chamber coordinate plane showing two perpendicular views A and B. The unit shown is used for the measurement of the Y coordinate.*

The direction $\theta_R = 75^\circ$ was used as a guideline to install the proton arm devices. In particular, the chamber P6 was placed perpendicular to it at about 24 cm center-to-center from P5.

2.3.1.3 Readout

The total anode charge is registered and analyzed later to get information on the energy loss and thus on the particle charge if needed[5]. The charge from every cathode strip is sent first to a GASSIPLEX-chip [67] . It has 16 input channels that consist of a charge sensitive amplifier (CSA), a switchable filter, a shaper and a track&hold-stage. After shaping and pre-amplification, these channels are multiplexed to one output allowing a sequential readout of all channels. The outputs from all the units are buffered and then sent to an 8 bit flash ADC (FADC) unit. Due to this relatively low resolution (256 digitizing channels) the chambers were not used with the full possible gain in order to avoid the FADC charge overload. The HV set on the anode wires was then limited to +1.7 KV which is to be compared to the breakdown voltage 2.5 kV.

After the main control unit (Sec. 2.5 p.36) has generated a start the GASSIPLEX sequencer (GPS) generates a track&hold (T/H) signal which enables the GASSIPLEX to store the signal amplitude for every cathode strip. $3\mu s$ later the GPS generates a clock (CLK) signal in the form of a serie of 200 pulses at a frequency of 400 kHz ($2.5\mu s$ period) to output the information to the FADC. After each CLK, one strip is read at once. A common line is used for the readout of one coordinate plane. The FADC has one input and a clock generator which is set to 400 kHz : it is tuned to trigger only when the input has the right amplitude. After digitization, the information is sent to a dedicated memory module. This channel-by-channel readout allows multiplicity measurement and the coordinate reconstruction is still possible in case of high input rates (10^5 events/s).

2.3.1.4 Online calibration system - Test events

For a given readout channel, the knowledge of the relative electronic gain in neighboring channels is necessary to get the right corresponding input charges. The calibration system is triggered by a TEST pulse from the Control Unit (Sec. 2.5 p.36) at regular intervals ($\leq$1 Hz). The data are recorded as a "test event" and identified by a specific pattern register value. Precise pulses with 30 stepping amplitude values sweeping the whole dynamic range in use were produced by a dedicated DAC (Digital to Analog Converter) unit coupled to a common test strip made from 3-4 wires perpendicular to the cathode strips through an input capacity C_{in}. A test signal with a known amplitude A induces charges in all the cathode strips. The total charge can then be deduced from the relation $Q = A \cdot C_{in}$. Finally, the resulting output analog response from every strip is digitized and recorded. The linearity as well as the noise level from the pedestal peak position can then be checked for every channel.

2.3.1.5 MWPCs calibration

The induced charge on each cathode strip is determined from the raw flash ADC (FADC) values following two major steps: pedestal subtraction and then data absolute/relative calibration. This procedure, especially the pedestal subtraction step, is very similar to the one applied in the calibration of the two scintillator walls hence it will be exposed only here.

The pedestal peak is identified by accumulating "empty" events, i. e. the events which are not triggered by a beam particle. Regular pedestal runs were made during the period of several days that lasted the experiment. The pedestal peaks typically spread over few ADC channels. Their position was checked and no shift was observed during the running period. These peaks are fitted for every readout channel and the deduced values are systematically subtracted from the signal peak.

For every readout channel, one has a series of precisely known amplitudes and the corresponding response in ADC channels (Sec.2.3.1.4 p.26). These data are fitted with a first order polynomial and the resulting calibration coefficients have 1 % or less of relative uncertainty. An example of calibration plot is shown in figure 2.9.

---

[5] The anode signals from chambers P5 and P6 were used through a constant fraction discriminator to trigger the recoil particle passage.

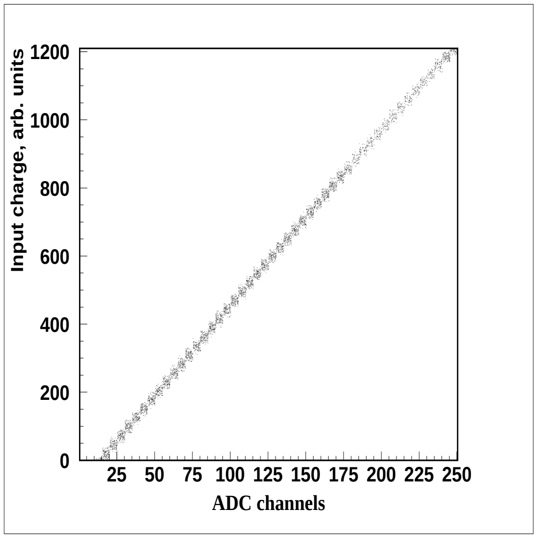

Figure 2.9: *Calibration plot for one given MWPC readout channel showing the charge injected into the cathode strip during test runs versus the registered ADC channel.*

An offline alignment is performed on chambers P1, P2, P3 and P4 by using a ^4He beam. It consists of the identification, for each coordinate plane, of the strip associated to position zero. One assumes that the beam particles have no interaction and hence follow a straight line. From a set of 50000 events, the beam center-of-gravity is determined for each plane from a gaussian fit. The figure 2.10 shows the beam profiles in the X and Y planes of the considered chambers. The cathode strip associated to the distribution centroid is then identified as the reference strip in the MWPC local coordinate system. The obtained alignment uncertainty was $30\mu m$.

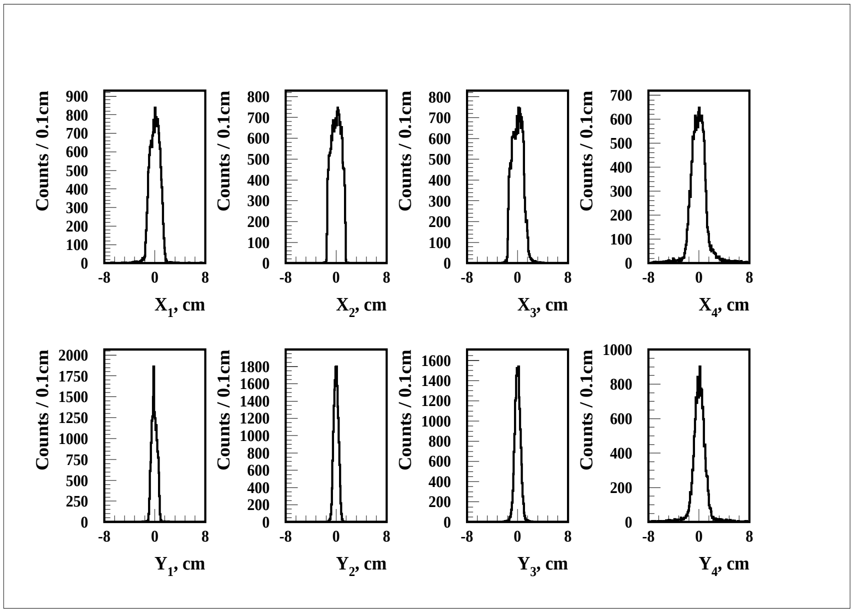

Figure 2.10: ^4He *beam profile during the alignment run of chambers P1, P2, P3 and P4. The beam distribution in X (resp. Y) direction is shown in the first (resp. second) row*

2.3.2 The liquid hydrogen target

The liguid hydrogen (LH_2) target and the whole ensemble were built by the cryogenics team of CEA, Saclay, France and successfully tested at 3 bar. It was installed at GSI in March 2000. The system was designed to be modular in order to work with different target cell geometries[6]. The main requirements for such a target were:

- to have thin windows for the scattered and recoil particles in the whole solid angle of interest
- to have a thick cell in order to compensate for the beam low rate. For the high energetic beam particles, the induced angular straggling was much below the needed angular resolution while the energy loss was negligible (Tab. 2.2 p.20) when choosing 10 cm of LH_2. On the contrary, for the low energy protons the thickness had to be limited to 2-3 cm in order to have a complete overlap with the beam spot and to limit angular straggling and energy loss.

The choice of the LH_2 rather than a paraffin $\sim (CH_2)_n$ was necessary because of the large angular straggling and energy loss induced on the beam particle and the recoil proton when CH compounds are used. To illustrate this point, one can compare the results from two equivalent targets that represent a hydrogen thickness of 708 mg/cm^2 (Tab. 2.5 for a beam particle) and 106.2 mg/cm^2 (Tab. 2.6 for a recoil proton) and recalling that hydrogen represents 1/6 of the paraffin in terms of mass. It is clear that the measurement in the cases considered here is impossible with a thick paraffin target.

$^{A}He, T_S$ (MeV/u)	ΔE (MeV/u) $[(CH_2)_n]$	$\Delta\Theta_S$ $(mrad)$ $[(CH_2)_n]$	ΔE (MeV/u) $[LH_2]$	$\Delta\Theta_S$ $(mrad)$ $[LH_2]$
^{6}He, 717	6.7	1.3	2.3	0.5
^{8}He, 671	5.1	1.0	1.8	0.4

Table 2.5: *Typical angular straggling* $\Delta\Theta_S$ *(rms) and energy loss* ΔE *for He beam particles. Two calculations were performed for* 100 mm LH_2 *and* 47.8 mm *paraffin representing the same hydrogen thickness of* 708 mg/cm^2.

T_R (MeV)	ΔE (MeV) $[(CH_2)_n]$	$\Delta\Theta_R$ $(mrad)$ $[(CH_2)_n]$	ΔE (MeV) $[LH_2]$	$\Delta\Theta_R$ $(mrad)$ $[LH_2]$
30	15.1	39.1	4.5	10.7
50	8.5	19.0	2.8	6.2
100	4.7	9.1	1.6	3.1
200	2.8	4.7	1.0	1.6

Table 2.6: *Typical angular straggling* $\Delta\Theta_R$ *(rms) and energy loss* ΔE *for recoil protons for energies between 30 and 200 MeV. Two calculations were performed for* 15 mm LH_2 *and* 7.2 mm *paraffin representing the same hydrogen thickness of* 106.2 mg/cm^2.

2.3.2.1 Target setup description

The target cell consists of a vessel filled with liquid H_2 and sealed at one extremity to a stainless steel body by a vacuum jacket made of Alumene[7] (Fig. 2.11). The vessel has a cylindrical shape of 100 mm length which represents a thickness of 708 mg/cm^2 and has a rounded appendage, the arch of which has a rise of 3 mm. The vacuum jacket part which is in contact with LH_2 is 10 mm wide, thus from the entrance to the exit window, the total target length on the Z axis is 113 mm. It is 30 mm diameter and is surrounded laterally by a 100 μm Mylar foil while the entrance and exit windows are made from 90 μm Mylar. The outer diameter of the vacuum jacket part which is in contact with the inox body is 40 mm. The thermal insulation of the vessel is assured by 5×25 μm standard aluminized Mylar. The filling and return gas tubes are connected on the inox body.

---

[6] At this moment, another bigger cylindrical target cell (20 cm height × 6 cm diameter) is available for spallation cross section measurements at GSI

[7] Alumene or Aluminium 5083 is made of 94% Al, 4.5% Mg, 0.4% Si, 0.04% Fe, 0.5% Mn, 0.25% Zn, 0.15% Cr and 0.15% Ti.

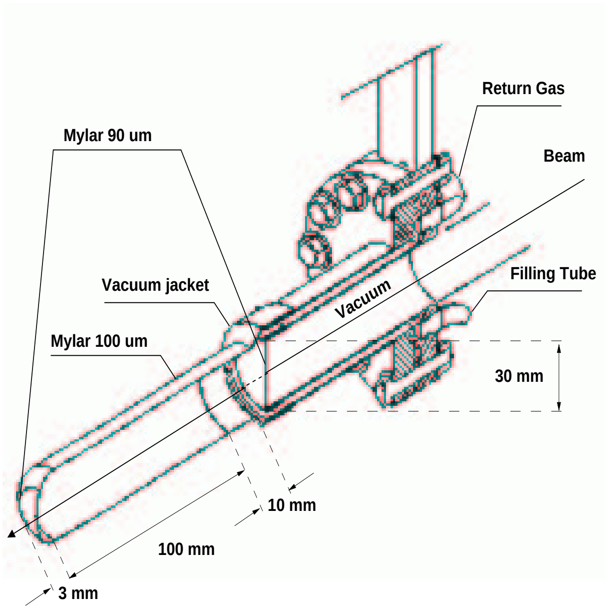

Figure 2.11: *Liquid hydrogen target cell*

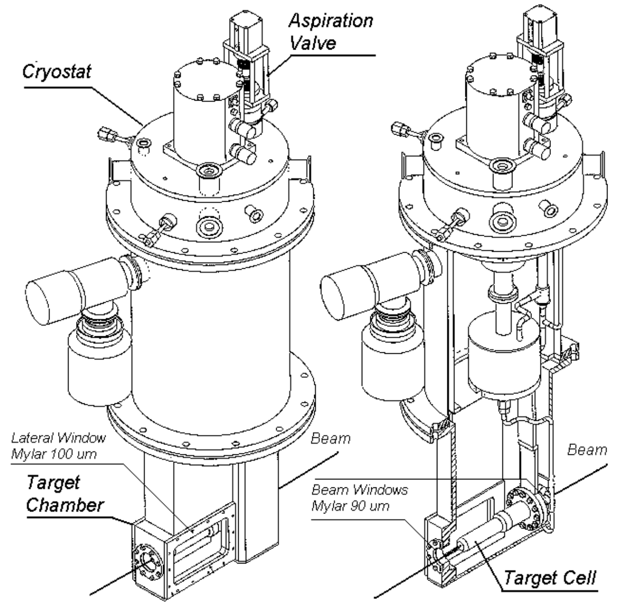

Figure 2.12: *Liquid hydrogen target - cryostat ensemble*

The system target+cryostat is in a residual 52 l vacuum chamber (Fig. 2.12) which provides a secondary containment volume in case of target flask rupture. The volume of the insulating vacuum space available for the release of hydrogen must be at least 52 times the volume of liquid H_2 contained in the vessel. Hydrogen expands about 52 times as liquid is vaporized to cold gas at atmospheric pressure. The vacuum chamber is equipped with an entrance and exit beam windows of 40 mm diameter (90 μm Mylar) and two lateral windows to let the recoil protons reach the detectors. The lateral windows (100 μm Mylar), rectangular in shape, are 95×160 mm and located at 42 mm from the beam axis which offers an acceptance of $\varphi = \pm 47^\circ$ and $60^\circ \leq \Theta_R \leq 90^\circ$ for the recoil arm. The acceptance for the scattered projectiles is $0^\circ \leq \varphi \leq 360^\circ$ and $0^\circ \leq \Theta_S \leq 4^\circ$.

The target is connected to a 175 l storage tank through two separate check valves. The final pressure in the storage tank is 1.05 bar and is always maintained slightly above the atmospheric pressure. This eliminates any risk of explosion fueled by oxygen leaking into the system. This pressure is at the same time the vapor pressure of the liquid corresponding to a temperature of 20.5 K for hydrogen. The condenser is a copper cylinder, 8.7 cm long and 14.1 cm in diameter, thermally isolated by a copper shield.

The gas handling system is composed of the plumbing, valves and controls necessary for transfering the hydrogen gas from the storage tank to the target cell and vice-versa. It is housed in one rack which contains manual valves, relief valves, pressure indicators and transmitters. This 'cryogenic' rack, the gas tanks and the instrumentation rack are located, for safety reasons, outside and above the experimental area on the concrete roof of cave B where the airing conditions are better. The main H_2 supply bottles with which the tanks were fed, were kept outside the building and connected with a special high purity $(1/10^6)$ pipe.

2.3.2.2 Operation principle

The cooling and the condensation of the gaseous hydrogen is managed by the refrigerating power of liquid helium and its cold vapors [68] in the temperature range 4-20 K. Helium gas is liquified by compression and sent to the cryostat. This operation takes generally 30 hours. Then hydrogen liquefaction by heat exchange between the cold head (helium) and the condenser (hydrogen) starts and last few hours. Filling the target with H_2 requires about 110 l of gas at NTP[8]. As a result, the storage tank is at pressure of 1.65 bar before the H_2 liquefaction. The total amount of H_2 gas used in the entire system is 290 l.

A so called "cold" (or aspiration) valve (Fig. 2.12) is mounted on the return tube between the target and the condenser. Opening this valve creates a rapid increase of the volume and induces a passage from liquid to gas phase at constant temperature within few seconds and vice-versa. This mode is called 'empty target' mode despite the target is filled with hydrogen gas at 20.5 K and enables to evaluate the background arising from sources other than liquid hydrogen. The thickness of the hydrogen gas present in the target is then 12.9 mg/cm^2. Two level sensors (470 type carbon resistor) allow detection of the thermal exchange between gas and liquid in order to determine the two operation states (empty - full target).

One of the main priorities when the setup was produced was its reliability and safety during operation [69] thus the strength coefficients of the inner vessel and other sensitive materials were always set better or equal to the recommended values [70]. The basic idea behind safe handling of any flammable or explosive gas is to eliminate oxygen and to avoid exposure to any energy source that could cause ignition. The most probable fuel gas is oxygen present in the atmosphere and the most likely ignition sources are from electrical equipment. When the target is filled up and stabilized, the connected setup does not use any electrical power. The electrically driven vacuum pumps are switched off and only cryopumping is working. Automatic regulation of the H_2 level is done by pneumovalves. The used gas is always contained in the closed target-storage tank circuit. After an experiment is finished, the gas is kept into the storage tank with only some losses due to a normal over-pressure evacuation.

2.3.2.3 Performance

One of the main advantages to use a pure liquid H_2 target is obviously the low level of background that arises for example when one uses targets made from hydrogenated-carbon compounds. This is sketched in figure 2.13 showing the energy loss spectra of the recoil protons in the front layer of the scintillator wall for the two target operating modes, both spectra being normalized to the incident beam flux. Despite the residual hydrogen gas present in the "empty target" mode, which is taken into account in the background subtraction during offline analysis (Sec.3.3.1 p.43).

2.3.3 The recoil particle scintillator wall - RPW

2.3.3.1 Description

The recoil particle wall is designed in 2 layers of 12 modules each. One module (Fig. 2.14) consists of 8 vertically aligned slats of 1 cm thickness, 110 cm length and 2.5 cm width BC408 plastic scintillator each. The BC408 [71] is made of a polyvinyltoluene base with a density of 1.032 g/cm^3 and a refractive index of $n = 1.58$. The mass composition can be assumed to be 10 carbon for 11 hydrogen atoms and is characterized by a light attenuation length of typically $L_{att} = 2.10\ m$.

Every slat is readout by 2 photomultipliers (PMs) from the top and bottom ends, yielding the needed energy loss (ΔE_{top} and ΔE_{bottom}) and TOF (TOF_{top} and TOF_{bottom}) information. The 8 slats, their PMs and HV bases are mounted in a common metal housing and shielded against δ electrons by a thin metal layer. The 8-fold modules are complete and independent detectors with high mechanical stability and easy handling. Only 6 modules were used which was sufficient to cover the entire angular range of interest.

The recoil particles meet the first (front) layer which is shifted by a half slat width with respect to the second (rear) layer (Fig. 2.15). The x_{wall} local coordinate is determined from the slats position. With this structure, one can achieve a position resolution of half slat width which corresponds to an angular resolution of about 5.43 mrad (0.3^o). The wall was positioned at about 2.3 m from the center of the target and tilted by an angle of 15^o in order to have its planes perpendicular to the direction $\vartheta = 75^o$ which is the average recoil angle.

The partial perspective view of the experimental setup (Fig. 2.16) shows the recoil arm section together with the surrounding of the target up to the last counter S3. The He gas bag in the recoil arm is a semi-

---

[8] Normal temperature and pressure conditions

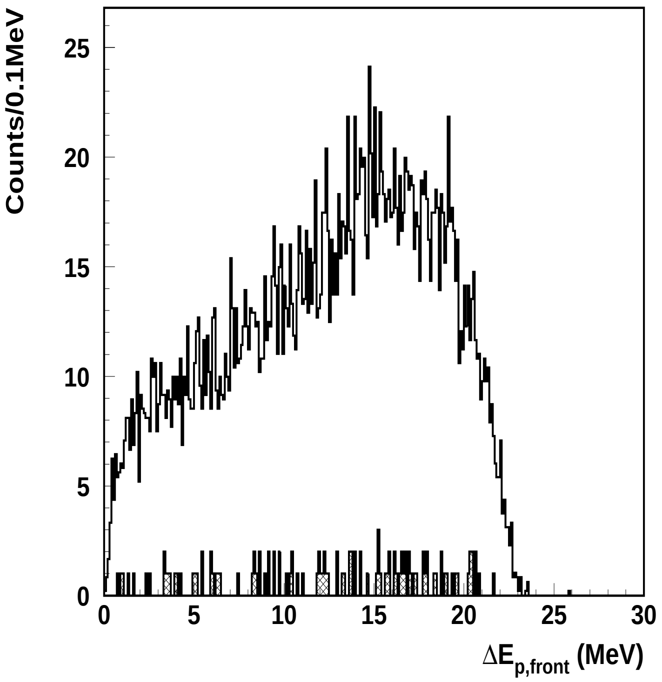

Figure 2.13: *Spectra of the elastic proton energy loss $\Delta E_{p,front}$ in the RPW front layer with filled and empty (hatched) target from interaction of ^6He. The spectra are normalized to the same flux of incident particles.*

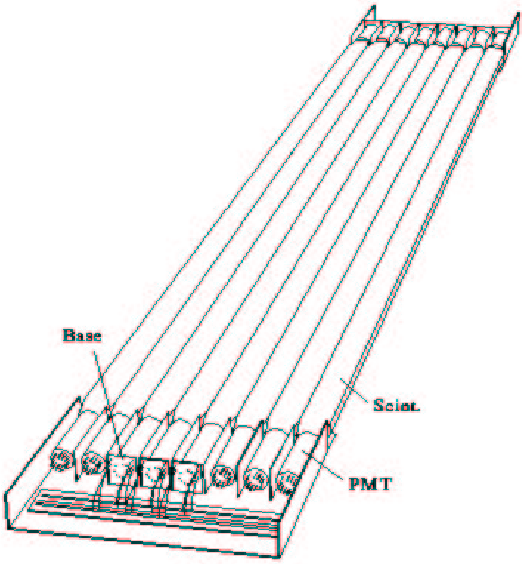

Figure 2.14: *Perspective view of one 8-pack scintillator module of the recoil particle wall*

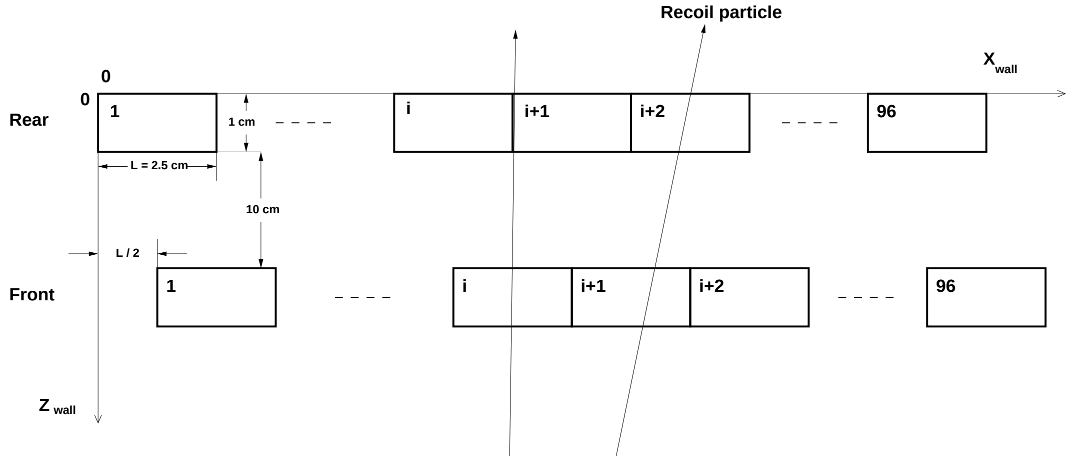

Figure 2.15: *Aladin TOF wall top view showing the local coordinate system (X_{wall}, Y_{wall}, Z_{wall}). The front layer is shifted by one slat half width $l/2$ in the X_{wall} direction. This architecture enables a refined analysis and in particular to disentangle the "grazing shots" like the one shown in the figure and hitting rear slats i and $i+1$.*

pyramid made from 5 mm thick PVC. It is 1.8 m height and has a 40×40 cm^2 entrance window and a 80×80 cm^2 exit window. The windows are made from 30 μm mylar.

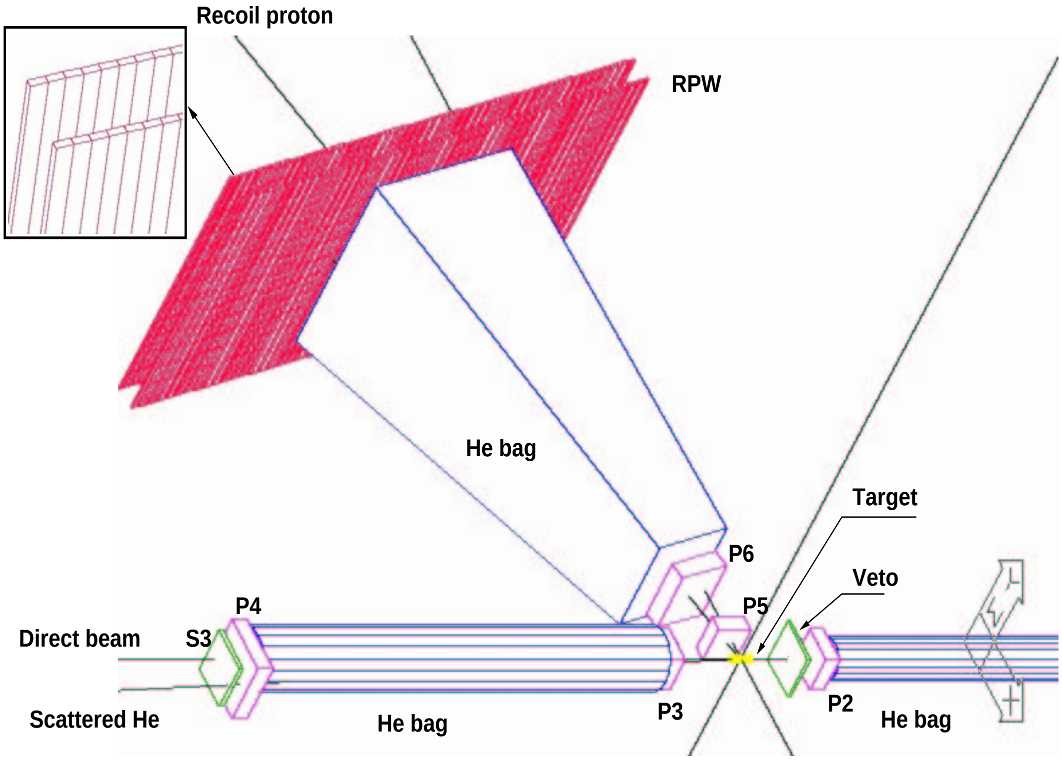

Figure 2.16: *Perspective view of the target area and the recoil proton wall (RPW)*

2.3.3.2 Calibration

The energy loss was calibrated by a primary deuteron beam at energies of 100, 200 and 400 MeV/u. The scintillator wall is positioned after the dipole magnet and therefore all the slats can be illuminated by the sweeped beam. The expected energy losses in the front and rear layer are shown in table 2.7. The energy of the beam being in the range of few hundreds MeV/u and the recoil protons expected in the range , it is then needed to extrapolate the calibration to higher energy losses, up to 32 MeV[9] (Fig.2.17). Typical ΔE calibration curves are shown in figure 2.18 for four neighbouring PMs from the top side of the front layer: as an example, ft25 stands for the PM located on **t**op of slat number 25 in the **f**ront layer.

$T_{d,in}(MeV/u)$	100	200	400
$\Delta E_{front}(MeV)$	8.1	4.7	3.1
$\Delta E_{rear}(MeV)$	8.4	4.7	3.1
$\delta(\Delta E)_{rms}(MeV)$	0.38	0.39	0.42

Table 2.7: *Calculated energy losses of deuterons with kinetic energy $T_{d,in}$ crossing the RPW at different incident energies in the front and rear layers (ΔE_{front} and ΔE_{rear} respectively). $\delta(\Delta E)_{rms}$ is the common energy straggling obtained at those energies.*

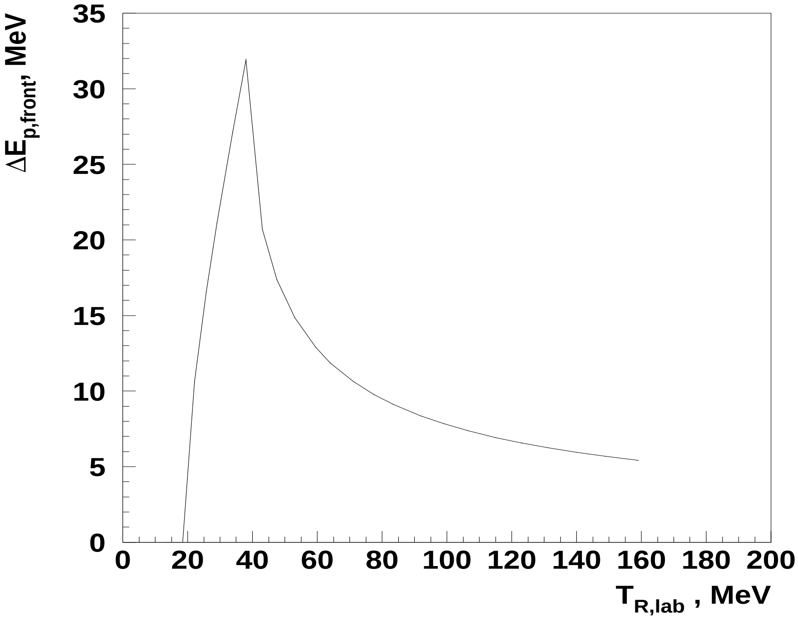

Figure 2.17: *Calculated recoil proton energy loss in the RPW front layer $\Delta E_{p,front}$ as a function of their kinetic energy $T_{R,lab}$ after interaction. All the media crossed by the protons were taken into account. Less energetic protons are stopped before reaching the wall (see e. g. Fig. 2.19), the low limit being roughly 20 MeV.*

Energy loss in one slat

If ΔE is the energy released in one slat at a given impact point B and assuming no external losses, then every PM will receive half of it but attenuated. One can write the energy amplitudes at the top and bottom PMs as:

$$\Delta E_{top} = \frac{\Delta E}{2} \exp^{-\alpha(L/2 - y_{wall})}$$

---

[9] Indeed, 38 MeV recoil protons have the maximum energy loss of 31.8 MeV

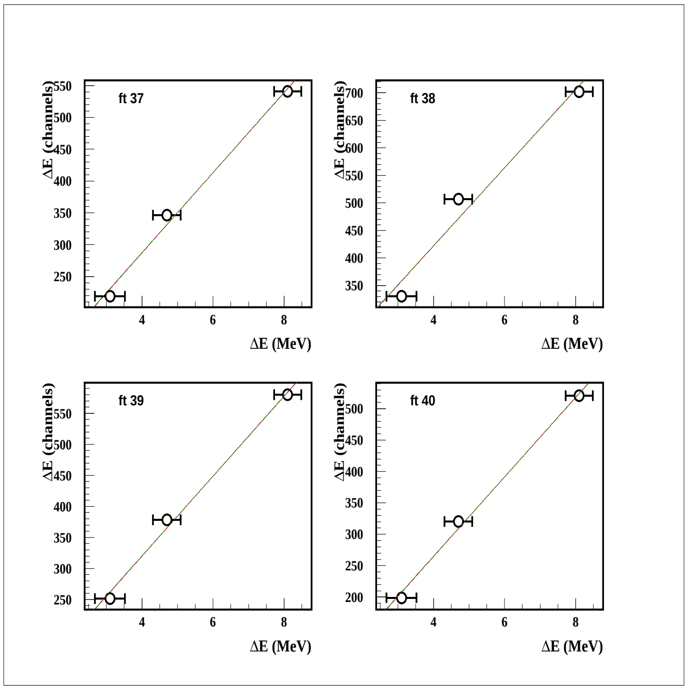

Figure 2.18: *Typical ΔE calibration curves of four photomultipliers in the RPW obtained from the deuteron run. The channel number of the peak position is plotted versus the calculated energy loss. In each plot, the three lines show the central fit estimate and the low and high estimates due to uncertainties of the expected energy losses (horizontal error bars)*

$$\Delta E_{bottom} = \frac{\Delta E}{2} \exp^{-\alpha(L/2+y_{wall})}$$

where $\alpha = 1/L_{att}$ is the attenuation coefficient per unit scintillator length and L the slat length. y_{wall} is the y coordinate of the point B, the Y_{wall} axis, parallel to the slat, being directed from bottom to top. The energy loss is then given by:

$$\Delta E = 2\sqrt{\Delta E_{top}\Delta E_{bottom}} \exp^{-\alpha L/2} \tag{2.7}$$

and y_{wall} can be expressed as :

$$y_{wall} = \frac{1}{2\alpha} \ln \frac{\Delta E_{top}}{\Delta E_{bottom}} \tag{2.8}$$

The expected energy losses of the elastic recoil protons are shown in figure 2.19 made from a Monte-Carlo simulation of scattering from a 717 MeV/u ^6He beam plotted in function of the recoil kinetic energy T_R. From the front layer (Fig. 2.19.A) one identifies - from left to right - the following contributions:

- protons stopped before reaching the wall ($\Delta E_{p,front} = 0$) for $T_R \leq 19MeV$
- protons stopped in the first layer for $19MeV \leq T_R \leq 37MeV$ ($\Delta E_{p,rear} = 0$ from Fig. 2.19.B) where of course the energy loss increases with increasing T_R. A maximum energy loss of $\sim 33MeV$ is reached for protons emitted at $\sim 37MeV$.
- protons that crossed the front layer for $T_R \geq 37MeV$ where typically the energy loss decreases with increasing T_R. Some of these protons are stopped in the second layer (Fig. 2.19.B) for $37MeV \leq T_R \leq 53MeV$ while the rest escape the scintillator wall.

Time of flight in one slat

For the relative TOF calibration purposes, the RPW is equipped with a dedicated laser system which fires all slats at once through a network of optical fibers. The calibration was linear:

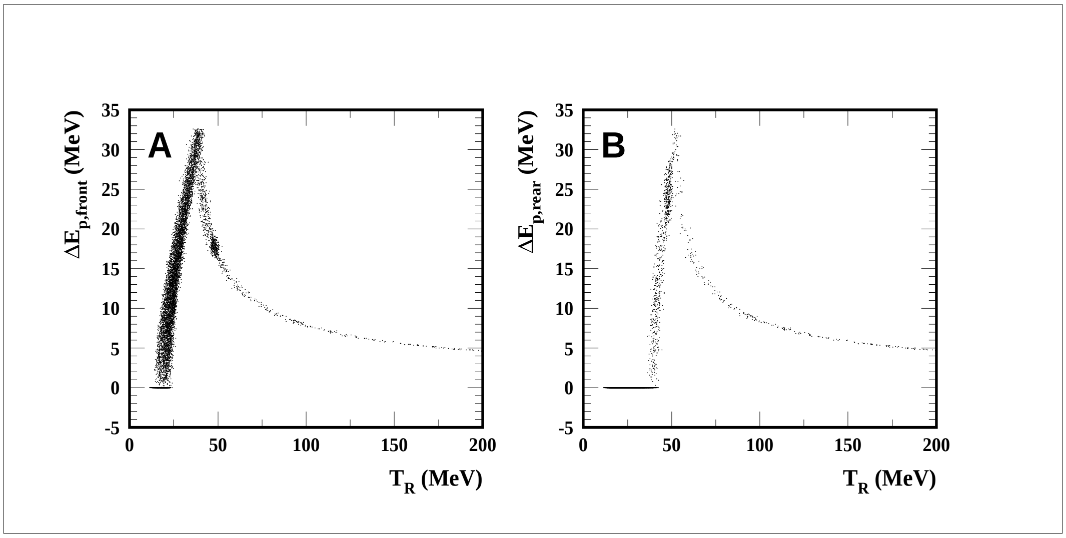

Figure 2.19: *Calculated energy losses on the recoil scintillator wall front (A) and rear (B) layers from the 717 MeV/u* ^6He *elastic scattering function of the recoil kinetic energy* T_R. *The different contributions are explained in the text.*

$$TOF_{ns} = a.TOF_{channels} + b$$

The calibration constant a was determined by making two laser runs with a 122.4 ns delay while the offset b was gathered from the different deuteron beam energies having therefore different possible TOF. If TOF_{top} and TOF_{bottom} are the TOFs recorded at the top and bottom PMs respectively and assuming that the two signals reach the PMs at a speed c/n, then one writes:

$$TOF_{top} = TOF + \frac{n(L/2 - y_{wall})}{c}$$

$$TOF_{bottom} = TOF + \frac{n(L/2 + y_{wall})}{c}$$

then the time-of-flight TOF of the event is given by:

$$TOF = \frac{1}{2}(TOF_{top} + TOF_{bottom} + nL/c) \tag{2.9}$$

2.3.4 The scattered particle scintillator wall - SPW

2.3.4.1 Description

The scattered particle wall is made of two large (1.8m length ×1.4 m width) layers. The front layer has 14 horizontally aligned scintillators (1.8m long × 10cm wide × 0.5cm thick) made from the same material (BC 408). The rear layer is made of 18 vertically aligned scintillators (1.4m long × 10cm wide × 0.5cm thick). It was positioned perpendicular to the beam direction at 2.3 m upstream from the exit window of the dipole magnet.

2.3.4.2 Calibration

A relative energy calibration was performed enabling an easy identification of the scattered particles nuclear charge. With a direct sweeped beam - the wall being positioned after the dipole magnet -, it was only possible to calibrate the vertical slats and the three central horizontal slats due to difficulties to move it up and down. For the TOF calibration, one used a ^4He beam at 700 MeV/u. One run with a 41 ns delay in the electronic chain and another one without delay were performed to get the calibration parameters.

2.3.5 The ALADIN magnet

The ALADIN [72] (**A** **LA**rge **DI**pole mag**N**et) spectrometer has a gap height of 40 cm and a horizontal acceptance of 120 cm. The bending power of 2.3 Tm satisfies the experiment requirements and allows to obtain the necessary resolution in mass and momentum. As an example, ^8He at 674 MeV/u with a magnetic rigidity of 18 Tm is deflected by an angle of 7.3°. A typical result can be seen in Fig. 3.5 p.44. The dipole magnet entrance frame is positioned $3m$ downstream from the target and is tilted by 7° with respect to the incoming beam direction to the side of positive X. The gap height limits the θ_S vertical acceptance to 4° while the horizontal acceptance is much larger than the required range. The spectrometer acceptance is thus full. It also enables to cover the entire range of rigidities which can vary by a factor 4. In the case of ^8He and assuming the same velocity then the following isotopes with nuclear charge $Z = 2$ are expected and separated: ^3He, ^4He, ^6He and ^8He. The stray field of the magnet affected neither the S3 photomultiplier nor the nearest MWPCs circuits. It varies on the beam axis from 200 G at the center of the magnet to a value of about 20 G at a distance of 1 m from the magnet.

2.4 Beam particles charge identification

The available ^6He beam is not isotopically pure (Fig. 2.4 p.22), so one needs to identify the beam particles and separate the corresponding scattering events. For the charge identification, the energy loss ΔE from counters S1 and S3 is used since $\Delta E \propto Z^2$ according to the Bethe-Bloch formula, Z being the nuclear charge of the incident particle (See e. g. Sec. 2.2.2 of Ref. [73]). Additionally, one uses the energy loss in the SPW which is the last detector met by the scattered particles in order to identify the reaction of beam particles happening after the target. Before making such an analysis, one ensures that the energy amplitudes did not vary during the measurement. In particular, S3 was not perturbed by the magnetic field of the ALADIN magnet.

For analyzing the beam composition before and after interaction in the target, the ΔE amplitudes measured on S1 and S3 were used. Such a correlation spectrum is shown in figure 2.20 taken from the ^6He run. Already at the beginning of the setup (S1) one distinguishes the three particle stable components with M/Z=3 which passed the separation procedure of the FRS (Fig. 2.4 p.22): ^3H , ^6He (the main peak in the spectrum) and ^9Li with respective charge numbers Z=1, 2 and 3. One also identifies, in S3, 20.2 % of ^6He events that got converted to Z=1 due to nuclear reactions within the experimental setup. These events are represented by the two peaks located below the main peak which are interpreted as due to the detection of one Z=1 event (lower peak) and two Z=1 events in coincidence in S3 (upper peak).

2.5 Trigger logic

The whole data acquisition (DAQ) system (Appendix C p.105) is triggered by a two-level logic:

1. a first level signal T1 delivered by a coincidence between the scintillators S1, S2 and S3 and an anti-coincidence from the veto counter. The generated signal is lead by the S1 signal rise edge.
2. a second level signal T2 delivered by a coincidence between the X and Y anode planes of the MWPCs P5 and P6.

We generally refer to the first one as the "beam trigger" and the second as the "proton trigger" or “scattering trigger”. At this stage and in order to have a reasonable acquisition speed, it is not possible to separate the elastic scattering events from the breakup and other reaction channels since their analysis needs a rather longer time. The figure 2.21 shows spectra of the scattered particles X coordinate in the last chamber P4 from the ^6He run, that means after a possible interaction in the target. We have chosen three distinct cases:

- case A: first level trigger only (direct beam) - target empty. Here one can identify the position of the direct beam.

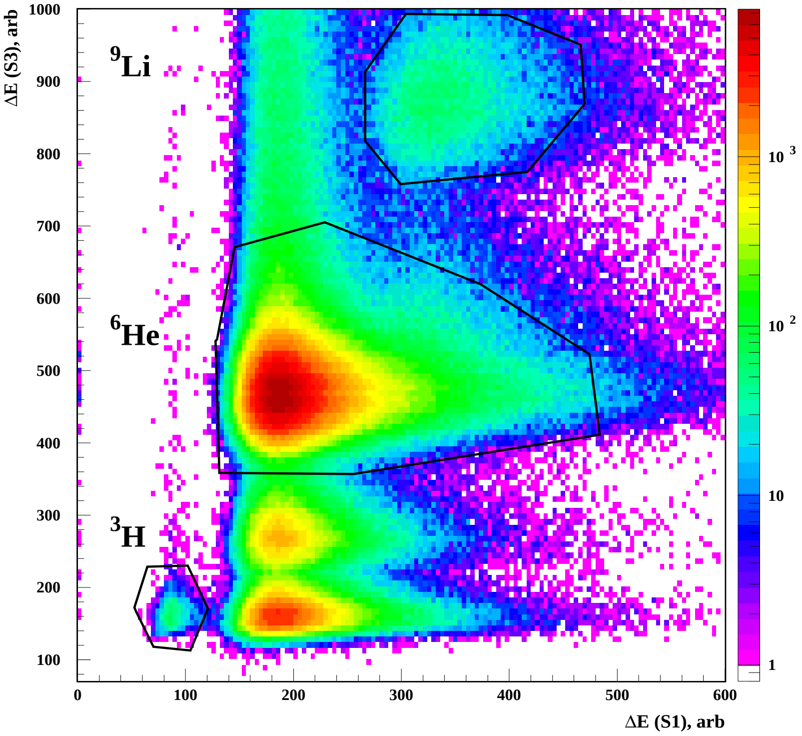

Figure 2.20: *Energy loss amplitude correlations of beam particles before (S1) and after (S3) interaction in the target (^6He run) showing, in particular, the presence of ^9Li and ^3H contaminants*

- case B: first and second level trigger - target empty. Only a few scattered events are observed which one can associate to the residual cold hydrogen gas in the target.
- case C: first and second level trigger - target filled. The contribution of the scattered events becomes now much more important.

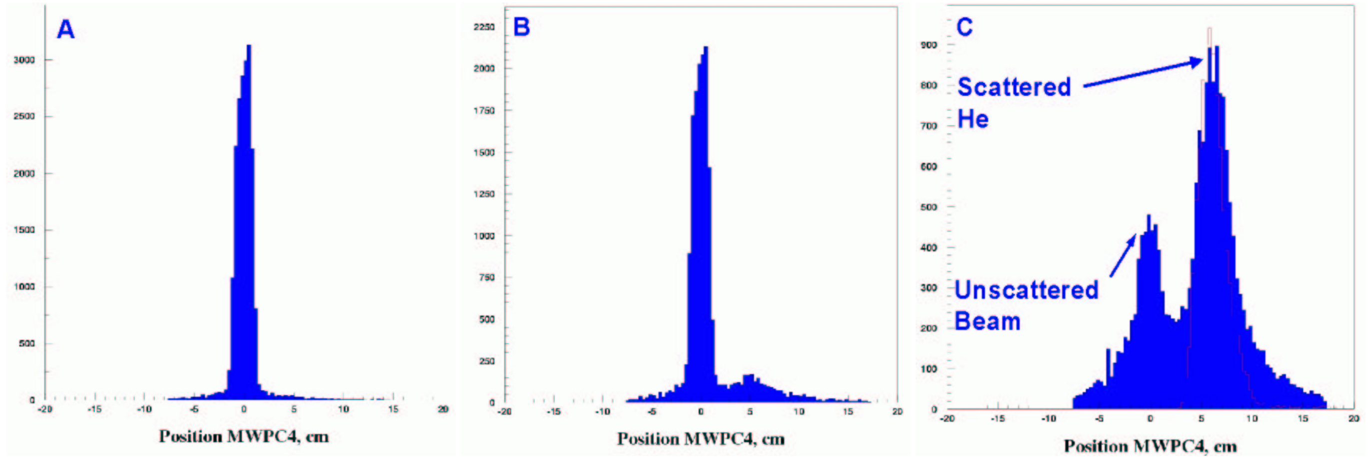

Figure 2.21: *X position spectra from the chamber P4 for different conditions on the target operation mode and the trigger. Figures A and B show contributions from an "empty" target while figure C corresponds to a filled target. In figure A, one considered only the first trigger T1 and in figures B and C, the triggers T1 and T2 were required simultaneously.*

Chapter 3

DATA ANALYSIS AND EXPERIMENTAL CROSS SECTIONS

Through this chapter, one will discuss mostly the case of ^6He hence most of the plots were made for this isotope. The situation for ^8He is almost similar and some plots will be shown for the completeness and the homogeneity of the analysis. The ^6He run lasted 55.2 hours (background run: 11.7 hours) while the ^8He lasted 59 hours (background run: 2.4 hours). A secondary ^4He beam at 700 MeV/u was sweeped on the vertical slats of the SPW for the purpose of calibration.

3.1 Analysis of the scintillator walls

One typical event shows a cluster of hits. A hit in a given PM is defined whenever the energy and TOF signal amplitudes meet basic requirements, e.g. raw TOF signal amplitude greater than 0 and the raw ΔE greater than the noise level, obviously when both the amplitudes are not saturating. An analysis of the different hits is performed in order to identify a candidate particle and to derive its time-of-flight and energy loss.

3.2 Analysis of the MWPCs

After having realized the chamber alignment (zero position calibration), follows then the procedure of position coordinate determination (Appendix A p.97), determination of scattering and recoil angles and finally the interaction vertex is searched. These topics are explained in the next subsections.

3.2.1 Angle determination

In a two-body kinematic scattering, the incident, scattered and recoil tracks are all contained in the so called interaction plane. The scattering and recoil angles θ_S and θ_R on one hand, and the azimuthal angles φ_S and φ_R are correlated since they must fulfill momentum and energy conservation laws.

3.2.1.1 Scattering and recoil angles

The scattering angle θ_S is given by:

$$\theta_S = \sqrt{\theta_x^2 + \theta_y^2}$$

where θ_x and θ_y result from the projection of the particle momentum in the (XZ) and (YZ) planes respectively. They are determined with the following:

$$\theta_x = \theta_{x,out} - \theta_{x,in}$$

$$\theta_y = \theta_{y,out} - \theta_{y,in}$$

Here, the subscripts *in* and *out* refer to the incident and scattered particle tracks respectively. These incoming and outgoing angles are related to the particle coordinates x_i and y_i where $i = 1, 2, 3, 4$ refer to the chamber number as:

$$\theta_{x,in} = \arctan\left(\frac{x_2 - x_1}{z_{2x} - z_{1x}}\right)$$

$$\theta_{x,out} = \arctan\left(\frac{x_4 - x_3}{z_{4x} - z_{3x}}\right)$$

$$\theta_{y,in} = \arctan\left(\frac{y_2 - y_1}{z_{2y} - z_{1y}}\right)$$

$$\theta_{y,out} = \arctan\left(\frac{y_4 - y_3}{z_{4y} - z_{3y}}\right)$$

For a chamber i, z_{ix} and z_{iy} refer to the z position of the X and Y coordinate planes respectively. Numerically, one has $z_{2x} - z_{1x} = 196.9$ cm, $z_{4x} - z_{3x} = 209.7$ cm, $z_{2y} - z_{1y} = 196.9$ cm and $z_{4y} - z_{3y} = 228.8$ cm with a typical uncertainty $\Delta z = 0.5$ cm. The recoil angle θ_R is defined with the following relation:

$$\cos\theta_R = \mathbf{U}_{12}.\mathbf{U}_{56}$$

where $\mathbf{U}_{12}$ and $\mathbf{U}_{56}$ are the momentum unit vectors in the direction of incoming and recoil particle tracks, respectively. U_{56} is computed directly from the chambers 5 and 6 coordinates. The scatter plot in figure 3.1 shows the correlation between the scattered and recoil angles for elastic events, selected as shown in section 3.3.1 p.43. As can be seen, the experimental correlation reproduces well a simple two-body kinematic expectation. For small scattering angle, the spread on the recoil angle values is larger because of the more important multiple scattering.

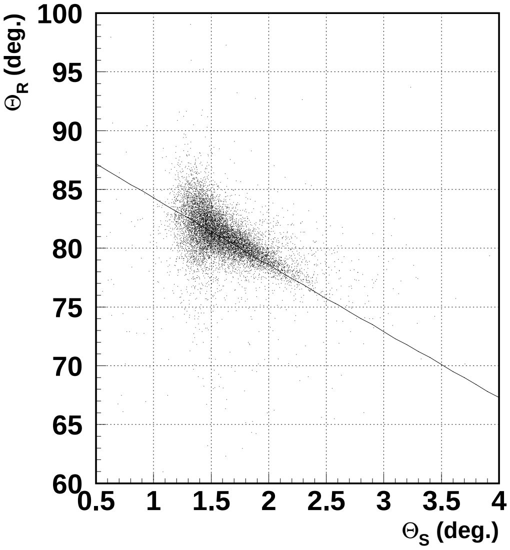

Figure 3.1: *Recoil angle θ_R versus scattering angle θ_S for elastic events. The continuous line is a two-body kinematic calculation.*

Uncertainty determination on θ_S and t

The experimental errors on θ_S and $|t|$ were determined from the propagation error formula (Appendix B p.101)

3.2.1.2 Azimuthal angles

The azimuthal angles are defined in the plane perpendicular to the interaction plane. Instead of taking the original definition, the following quantities were defined and used for further selection:

$$\varphi_S = \arctan\left(\frac{y_4 - y_3}{x_4 - x_3}\right) \tag{3.1}$$

$$\varphi_R = \arctan\left(\frac{y_6 - y_5}{x_6 - x_5}\right) \tag{3.2}$$

With those definitions, one ensures that $\varphi_S = \varphi_R$ as shown in Fig. 3.2. These correlation property was used as an additional selection criterion in the determination of the cross sections.

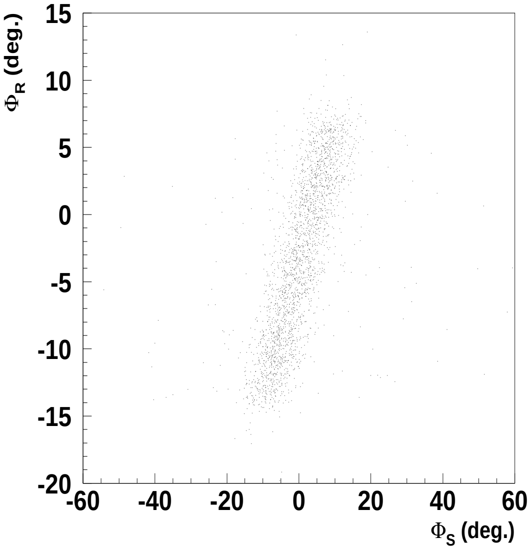

Figure 3.2: *Off-plane angles φ_S (scattered particle) and φ_R (recoil particle) correlations. A subset of the ^6He data was taken and elastic processes were selected (Sec. 3.3.1 p.43)*

3.2.2 Vertex coordinates

In the ideal case, the vertex should be the intersection point between the input and output beam tracks. In reality and due to the experimental uncertainties, it is defined by the region of space in the target where the interaction has most probably occured[1]. This corresponds to the region where the approach distance between the input and output tracks is minimum. It is given by[2]:

$$R_{DCA} = \sqrt{(x_{DCA}^2 + y_{DCA}^2)} \tag{3.3}$$

Here $x_{DCA} = Min(x_{out} - x_{in})$ and $y_{DCA} = Min(y_{out} - y_{in})$ where x_{in} , x_{out} , y_{in} and y_{out} are determined along the considered tracks. The target was divided into 30 slices along the Z (beam) direction. If in one given

---

[1] Events with more than one output tracks were identified, the mean multiplicity per event being 1.4. The search for the interaction vertex will also enable one to find out the right set of tracks.

[2] DCA = distance of closest approach

slice, $x_{in.out}$ or $y_{in,out}$ exceeds the veto aperture, the corresponding track is rejected. The slice corresponding to the minimum approach distance is then further divided into 10 slices to look for the final minimum. In case where two vertices were found, the one with the smaller approach distance is kept. The vertex coordinates x_v , y_v , z_v and the two variables x_{DCA} and y_{DCA} are then stored for further use. The figure 3.3 shows the x_{DCA} and y_{DCA} distributions for a partial set of the ^6He data in the range of $\pm 1mm$ together with the one for R_{DCA} in the interval $[0, 0.5mm]$.

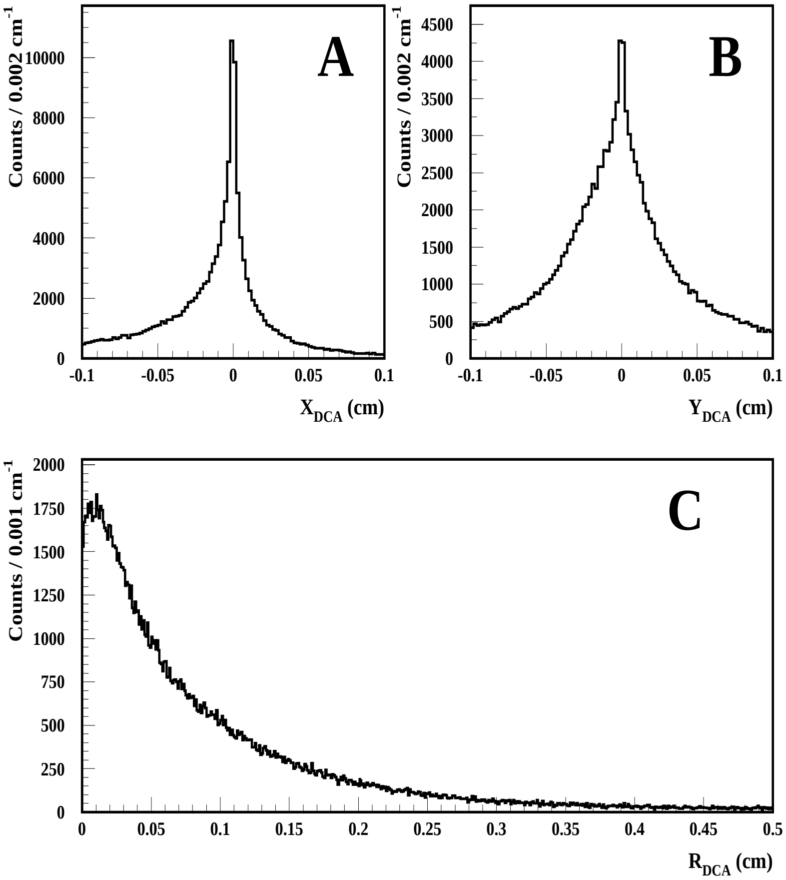

Figure 3.3: *Spectra showing the distance of closest approach (DCA) distribution along the X (A) and the Y (B) direction. The figure C shows the R_{DCA} (Eq. 3.3) distribution. A subset of the ^6He data was used and beam particles with nuclear charge Z=2 were selected.*

Here the scattering events which are close to the ideal case $x_{DCA} = y_{DCA} = 0$ can be considered as the ones holding the best tracking quality. This criterion is important when evaluating the angular distributions serving for the cross section extraction[3]. One may notice that the quality of the x_{DCA}distribution (FWHM$\simeq$0.008 cm) is better than the one of y_{DCA} (FWHM$\simeq$0.04 cm). The determination of $x_{DCA}, y_{DCA}, R_{DCA}$ and consequently the vertex precision, depends on the scattering angle θ_S. At low θ_S, the tracks are almost parallel. The different input and output coordinates are almost equal and close to 0, therefore the relative uncertainties are high. The figure 3.4 shows clearly this effect for the Y coordinate. This can be explained simply by considering our setup geometry which enables, through the trigger, to record higher values for $\vartheta_{X,S}$ than it does for $\vartheta_{Y,S}$. By looking more closely to figure 3.4 one can see from the top part the direct beam component located at $\vartheta_{X,S} = 0$ and symetric in x_{DCA}direction and the scattered part component located at $\vartheta_{X,S} > 0$ and asymetric in x_{DCA}direction[4]. This asymetry is only a consequence of the setup geometry and

---

[3] In particular, it will be shown in a later section (Sec. 3.3.3 p.45) that the angular distribution of the elastic events does not vary by requiring different selections on those variables, therefore it does not depend on the event tracking quality.

[4] In principle, one cannot determine a vertex for the unscattered beam particles but due to experimental uncertainties $\vartheta_{X,S} \neq 0$, therefore the searching procedure used here is successful. This artefact does not of course, influence the final cross sections.

the trigger logic; it disappears completely when looking the same spectra with only a direct beam.

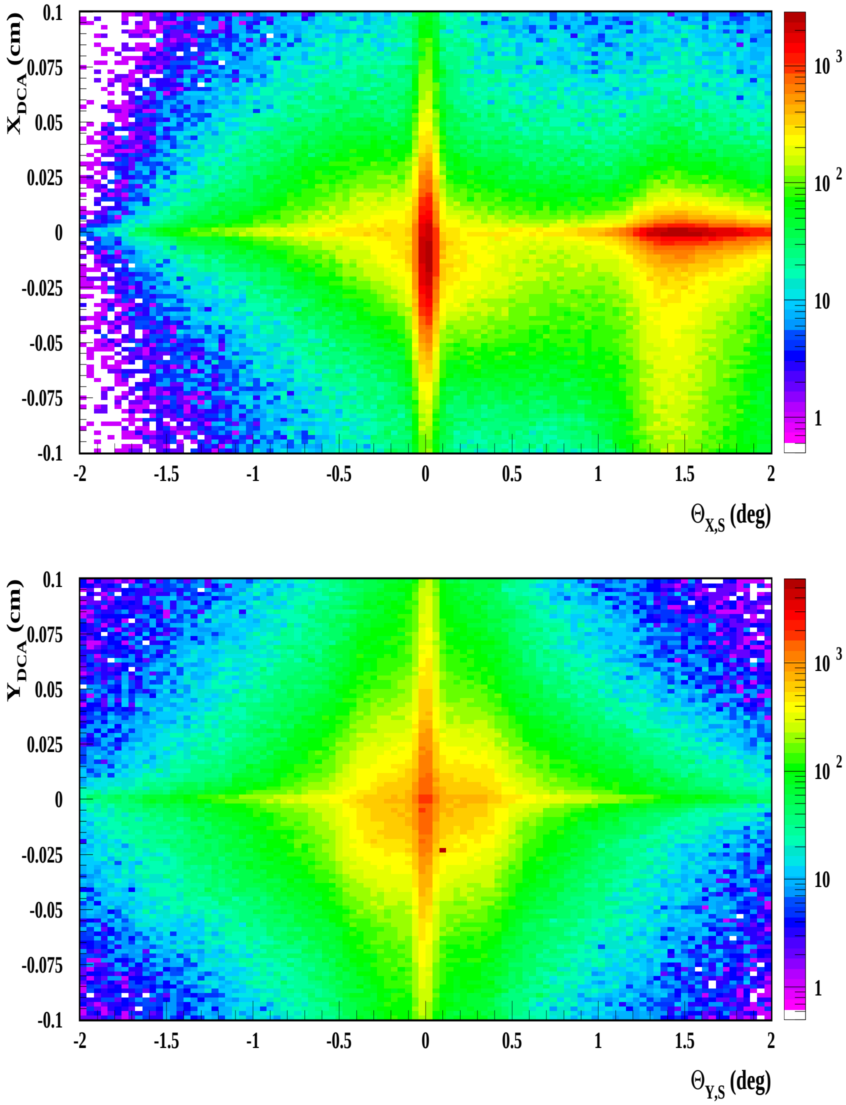

Figure 3.4: *Distance of closest approach coordinates* x_{DCA} *and* y_{DCA} *versus the corresponding scattering plane angles* $\vartheta_{X,S}$ *and* $\vartheta_{Y,S}$

3.3 Angular distribution of elastic events

The tracking and the particle ΔE information are used to separate the elastic scattering events from the other possible reaction channels. It is then possible to correct for the remaining background coming from the scattering of beam particles in the target body and to check that the angular distribution pattern is independent from the event tracking characteristics.

3.3.1 Selection of elastic events

In order to separate elastic scattering events from the breakup channels, two major conditions were required[5]:

---

[5] An additional cut using the correlation property between the recoil and scattered azimuthal angles (Fig. 3.2 p.41) was additionally used.

- the ΔE from the counters as well as from the SPW was used for particles with nuclear charge $Z = 2$ (He). In the same way, only particles with $Z = 1$ were selected from the ΔE recorded in the RPW.
- the tracking information before and after the magnetic analysis was used. An example in Fig. 3.5 shows how the elastically scattered ^6He can be separated from the other stable isotopes ^3He and ^4He[6]. This correlation is a direct consequence of the fact that at these relativistic energies, beam particles, the elastic scattered particles and the fragments have almost the same velocity when they pass the dipole magnet and thus the separation between them is possible.

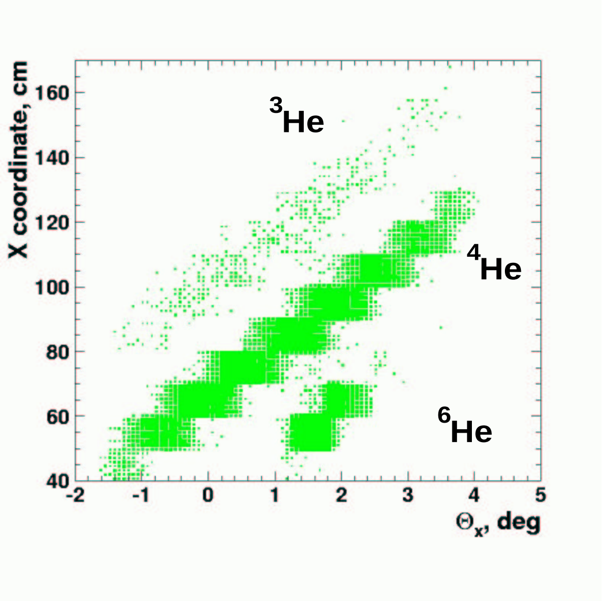

Figure 3.5: *Correlation plot showing the X coordinate from the SPW versus the X component Θ_x of the scattering angle for the ^6He run. The "stair" structure corresponds to the 10 cm width of a vertical slat. The events from the direct beam (no interaction in the target) are located at $X = 30$ cm and therefore, do not appear on the plot. The ^6He resulting from elastic scattering is clearly separated from the products of break-up and other reactions.*

From the measured scattering angle θ_S, one determines the recoil kinetic energy for the elastic process as:

$$T_R = T_{in}\left(T_{in} + 2M\right) \frac{m + \left(T_{in} + M\right)\sin^2\theta_S - \cos\theta_S\sqrt{m^2 - M^2\sin^2\theta_S}}{\left(T_{in} + M + m\right)^2 - T_{in}\left(T_{in} + 2M\right)\cos^2\theta_S} \tag{3.4}$$

and then the determination of the experimental momentum transfer squared $-t$ is straightforward through Eq. 2.2 (p.17). This calculation coincides with the one made when the correlations between the recoil proton energy loss $\Delta E_{p,front}$ in the RPW front layer and the recoil kinetic energy T_R are used. The resulting $(\theta_R, -t)$ correlation plot is shown in Fig. 3.6 where one notices a good agreement with two body kinematics expectations.

3.3.2 Background subtraction

The background considered here concerns all the contributions which were not directly related to an interaction in the liquid hydrogen contained in the target. It was estimated by making an additional run with an empty target. With the working conditions, a small amount of gaseous hydrogen still remains in the cell and has to be taken into account in the background subtraction. One can write the number of events N_F and N_E from the full and empty target runs as the sum of the corresponding backgrounds (BG_F and BG_E respectively) and the pure corresponding liquid and gaseous hydrogen contributions, N_L and N_G respectively:

$$N_F = BG_F + N_L \tag{3.5}$$

---

[6] In the ^8He run, an equivalent plot shows a similar spectrum with the expected four particle stable isotopes $^{3,4,6,8}He$.

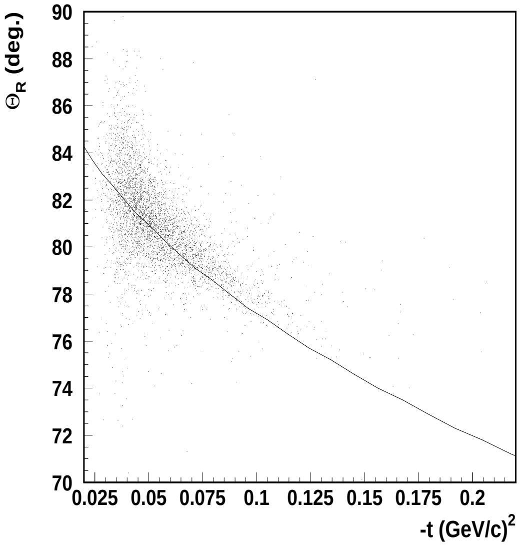

Figure 3.6: *Recoil angle Θ_R versus transfered momentum squared $-t$. The continuous line shows a two body kinematical calculation.*

$$N_E = BG_E + N_G \tag{3.6}$$

If F is the ratio of the number of incident beam particles in the two runs and $F_g = \rho_G/\rho_L$ is the gas-to-liquid hydrogen density ratio, then one writes:

$$BG_F = F \cdot BG_E \tag{3.7}$$

$$N_L = F \cdot N_G/F_g \tag{3.8}$$

then the background corrected contribution can be expressed as:

$$N_L \equiv N = \frac{N_F - FN_E}{1 - F_g} \tag{3.9}$$

The quantities N_F and N_L are in reality the determined $dN_{F,L}/dt$ distributions obtained from two dimensional (2D) plots such as the one shown in figure 3.6 and where $dN_{F,L}$ are the numbers measured in the interval dt. The number N is then correspondingly, the corrected dN/dt distribution.

3.3.3 Dependence of the dN/dt on the tracking quality

As already seen, for very small scattering angles, the incident and scattering tracks are almost parallel and thus, the determination of the vertex has relatively, bigger uncertainties and it is numerically evaluated through the distance of closest approach. Must one then operate a new selection on this basis ? To answer this question, it is helpful to study the statistical distribution dN/dt with different conditions on variables such as x_{DCA} and y_{DCA} (Fig. 3.3 p.42). In figure 3.7, for a given ^6He run data subset, the total distribution is shown together with distributions made with two inclusive cuts:

- Cut 1 $\equiv -0.5 \leq x_{DCA}, y_{DCA} \leq 0.5cm$
- Cut 2 $\equiv -0.1 \leq x_{DCA}, y_{DCA} \leq 0.1cm$

Whatever the selected region is, one sees clearly that the interacting particles are scattered with the same probability to a given direction. This means that, in order to determine the differential cross section, one can use all scattered particles whatever is the corresponding vertex precision.

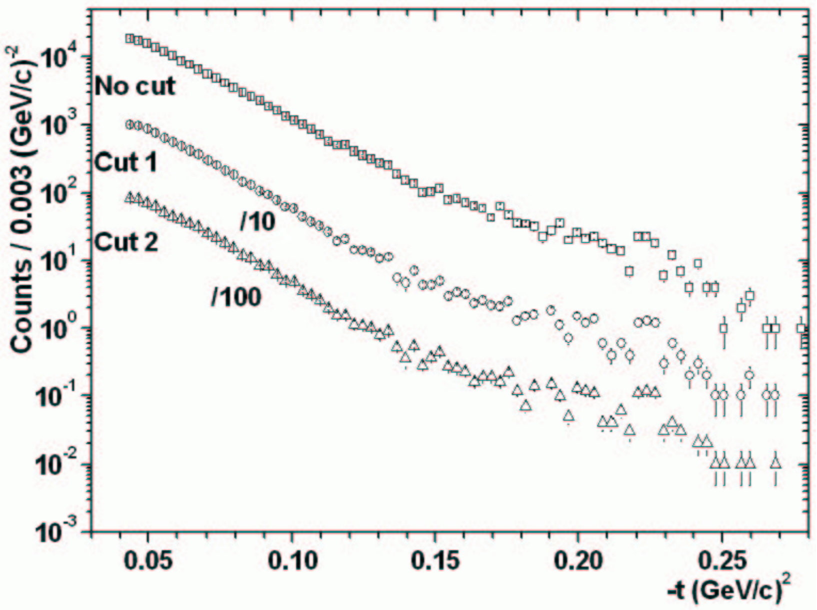

Figure 3.7: *Scattered particles total distribution dN/dt (no cut) from a subset of ^6He run data with distributions made after selecting two different regions from the x, y_{DCA} variables. The distributions from cuts 1 and 2 were scaled by, respectively, a factor 0.1 and 0.01.*

3.4 Extraction of the differential elastic cross section

The general procedure consists of sampling the data shown in Fig. 3.6. For a given interval $[t_i, t_{i+1}]$ and assuming a thin target (Sec. 3.4.2 p.47), one can write the following equation:

$$\frac{dN_{t_i,t_{i+1},0,2\pi}}{dt} = N_B \cdot N_T \cdot \frac{d\sigma}{dt} \tag{3.10}$$

where

- $dN_{t_i,t_{i+1},0,2\pi} \equiv dN$ is the total number of events detected in the interval $[t_i, t_{i+1}]$ and in the total φ angular range namely $[0, 2\pi]$
- $dt = t_{i+1} - t_i$
- N_B is the total number of incident beam particles identified as ^6He (^8He) and recorded by the DAQ system thus delimiting only that portion of the beam which was overlapping completely with the target area, this condition being necessary for Eq. 3.10.
- N_T is the number of proton nuclei in the target per unit area
- $\frac{d\sigma}{dt}$ is the differential cross section at t

3.4.1 Target density

The H_2 molecule has chemically two possible different configurations [74]: paranormal and orthonormal with respective abbreviations para and ortho. The hydrogen gas natural composition is 75% ortho and 25% para at standard conditions of temperature and pressure. When it converts into liquid, the composition evolves to approximately only para: after several days, a saturation is reached with 0.21% ortho. The table 3.1 shows, for a natural composition, the density at liquid-gas phase equilibrium and at the beginning of the liquefaction process [74]. The table 3.2 shows the same densities at the end of the process, i. e. for a para composition. The density of the target is determined by interpolation from these data.

$T_{eq}(K)$	32.0	30.0	28.0	26.0	24.0	22.0	20.38	19.0	17.0	15.0
$\rho_L(kg/m^3)$	46.648	54.207	59.167	63.037	66.222	68.964	70.939	72.472	74.487	76.322
$\rho_G(kg/m^3)$	19.570	10.565	7.110	4.792	3.163	2.006	1.3305	0.9011	0.4677	0.2096

Table 3.1: *Natural H_2 liquid and gas density at different equilibrium temperatures*

$T_{eq}(K)$	32.0	30.0	28.0	26.0	24.0	22.0	20.38	19.0	17.0	15.0
$\rho_L(kg/m^3)$	45.983	53.925	58.965	62.835	66.001	68.722	70.778	72.169	74.165	75.999
$\rho_G(kg/m^3)$	17.498	10.888	7.2975	4.9208	3.2557	2.0703	1.3377	0.9380	0.4919	0.2225

Table 3.2: *Para H_2 liquid and gas density at different equilibrium temperatures*

It is necessary to know how the equilibrium pressure evolves with the boiling point temperature. This is shown in tables 3.3 and 3.4. The hydrogen was liquified approximately 5 days before the ^6He run started. At this stage, the composition is still evolving which is a factor of uncertainty. The target temperature varied in the range [20K, 22K] which also introduces errors in the estimation of the density. Taking all these arguments into account and using the tabulated values, the deduced liquid hydrogen density is then:

$\rho_{H_2,L} = 0.0700 \pm 0.0013\ g/cm^3$

$T_{eq}(K)$	17.0	18.0	19.0	20.0	20.38	21.0	22.0	23.0	23.94	24.445
$P(mbar)$	313.52	461.08	654.23	900.71	1013.25	1208.2	1584.9	2038.9	2529.2	2833.5

Table 3.3: *Evolution of the liquid-gas equilibrium pressure at different boiling point values for natural H_2*

$T_{eq}(K)$	17.0	18.0	19.0	20.0	20.28	21.0	22.0	23.0
$P(mbar)$	327.92	482.55	679.16	932.03	1013.25	1246.75	1631.19	2093.48

Table 3.4: *Evolution of the liquid-gas equilibrium pressure at different boiling point values for para H_2*

3.4.2 Target thickness

The differential cross section defined in Eq. 3.10 is, in principle, valid for a thin target approximation where the amount of beam interaction is negligible therefore one uses a constant beam flux. If the interaction reaches few percent of the beam flux, this approximation is no more valid. In that case, the total number of detected particles from a reaction channel $'a'$ is given by:

$$N = \frac{N_B}{\sigma_{int}}\{1 - e^{-A.\sigma_{int}.\Delta z}\}\sigma_a \tag{3.11}$$

where:

- σ_a is the cross section for the reaction channel $'a'$
- the total interaction cross section σ_{int} includes all the reaction processes where the nature of the incident particle has changed. According to Ref. [14], for $p(^6He,^6He)$ at 717 MeV/u and $p(^8He,^8He)$ at 674 MeV/u, it is about $198.9 \pm 4.6\ mb$ and $252.0 \pm 4.8\ mb$ respectively
- N_B is the total number of incident beam particles on a target with thickness Δz
- $A = \frac{\rho_{H_2L} \times \aleph_{AV}}{M_H}$ is a constant characteristic of the target material
- ρ_{H_2L} is the density of liquid hydrogen (g/cm^3)
- $M_H = 1.00798\ g/mole$ is the molar mass of element H
- and $\aleph_{AV} = 6.022 \times 10^{23}\ mol^{-1}$ is the Avogadro number

The particular case of a thin target approximation can be made by the following:

$$A.\sigma_{int}.\Delta z \ll 1 \tag{3.12}$$

which means that the probability of interaction in the target is low. Then using $e^x \simeq 1 + x$ for $x \ll 1$ one has:

$$N \simeq N_B.A.\Delta z.\sigma_a \tag{3.13}$$

The determination of the interaction probability $P_{int} = A.\sigma_{int}.\Delta z$ gives 0.09 (9%) for $\Delta z = 10.8cm$ which means that the target must be assumed to be thick. Considering now the elastic scattering process σ_{el} and making sure that the shape of the recoil particles angular distribution does not vary with the interaction location, one can then use the thin target approximation of Eq. 3.13 to calculate the cross section. This of course underestimates σ_{el} . One can then use Eq. 3.11 to correct this difference. The correcting factor was found to be 1.05 ± 0.02.

3.4.3 Number of incident particles

The monitor number N_B is given by:

$$N_B = N_{coinc} - N_{EKR} \tag{3.14}$$

where

N_{coinc} is the total number of beam particle coincidences on scintillators S1, S2 and S3 and the anti-coincidence of the veto

N_{EKR} is the number of events killed by the control unit rationer. Here the real rates taking into account the dead time of the data acquisition system are used (Appendix C p.105).

3.4.4 Solid angle correction

The geometrical acceptance of the setup is total in the scattering arm since particles are accepted in the total φ range $[0, 2\pi]$ and for $1.5^\circ \leq \Theta_S \leq 4^\circ$ as already mentioned in the requirements, while it is limited in the proton arm. As the second level trigger is defined by P5 and P6, the experimental solid angle $\Delta\Omega_{exp}$ being limited by P6, it has to be evaluated for every interval $[t_i, t_{i+1}]$ used in the cross section calculation. No variation of the acceptance in the recoil arm was found in the interval of interest $0.05 \leq |t| \leq 0.3(GeV/c)^2$, the vertex of the interaction being either at the center or at the limits of the target cell. It was also more precisely checked in the central beam line and no noticeable variation was found. Therefore, the center of the target was used as a reference point for the acceptance determination. $\Delta\Omega_{exp,i}$ being the experimental solid angle in the interval $[t_i, t_{i+1}]$, the solid angle correction factor is then defined as:

$$F_{\Omega,i} = \Delta\Omega_{tot,i}/\Delta\Omega_{exp,i} \tag{3.15}$$

where $\Delta\Omega_{tot,i}$ is the total solid angle defined in the interval $[\theta_i, \theta_{i+1}]$ which is given by:

$$\Delta\Omega_{tot,i} = \int_0^{2\pi}\int_{\theta_{i+1}}^{\theta_i} \sin\theta d\theta d\varphi = 2\pi\left(\cos\theta_{i+1} - \cos\theta_i\right) \tag{3.16}$$

θ_i and θ_{i+1} being the recoil angle values corresponding to the interval $[t_i, t_{i+1}]$.

3.4.5 MWPCs efficiency determination

A last correction has to be applied, taking into account for the efficiency loss of the MWPCs used in the second level trigger. The most energetic recoil particles are detected with the lowest efficiency due to their low energy loss. For this aim, a Monte Carlo simulation [75][7] was used to determine the dependence of the MWPCs efficiency function on the momentum transfer squared t. The protons with different kinetic energies spanning the range of interest are conducted through the chambers. The mean energy loss varies from 2 keV for high energy protons up to 10 keV (Fig. 3.8). The gas gain was measured by using 5.9 keV γ emitted from a ^{55}Fe radioactive source.

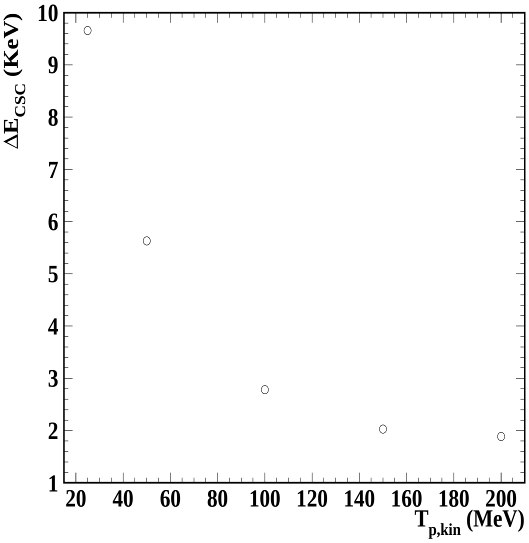

Figure 3.8: *Protons energy loss ΔE_{CSC} in a MWPC versus their incident kinetic energy $T_{p,kin}$ as calculated from a Monte Carlo simulation [75] taking into account all the MWPC characteristics.*

The same parameters as the ones used during the experiment are applied in the calculation: gas gain, gas mixture composition, high voltage and the MWPC geometry. Realistic errors taking into account the parameter fluctuations are also included. A threshold amplitude level, similar to the CFD (constant fraction discriminator) threshold used during the experiment, is set over which the amplitude signal is accepted and the event counted. The signal at the pre-amplifier (PA) output is used for comparison therefore the PA transfer function was measured and fitted for this purpose. The variation of the efficiency with the momentum transfer is shown in Fig. 3.9. The correction is negligible at $-t \simeq 0.05 (GeV/c)^2$ with an efficiency factor of about 1.00 ± 0.03 while it is important at $-t \simeq 0.19 (GeV/c)^2$ with a factor around 0.08 ± 0.04 meaning 50% of additional relative uncertainty on those data.

---

[7] This program was frequently tested and is considered to have a good reliability in the description of gaseous detectors. As these chambers were in the trigger, there was no other possibility to extract the efficiency than to simulate it.

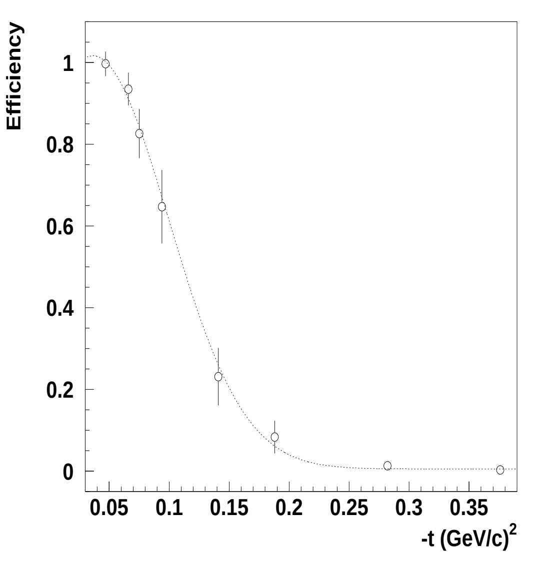

Figure 3.9: *MWPCs efficiency factor determined with a Monte-Carlo simulation [75] versus* $-t$*. The fitted curve was used for the correction of the differential cross section.*

3.4.6 Differential elastic scattering cross sections

The experimental differential cross sections $d\sigma/dt$ determined for $p(^6He,^6He)$ and $p(^8He,^8He)$ scattering are shown in figures 3.10 and 3.11 respectively. The data from the present work are plotted with open squares. In both figures, the data at lower transfered momentum $0.002 \leq |t| \leq 0.05(GeV/c)^2$ are also displayed in full squares. The errors shown represent contributions from statistical errors and errors from the MWPCs efficiency correction. These errors are t dependent and in particular, are higher in the region of high momentum transfer where the count rate is much lower. On the other hand, one identifies other sources of 'systematic' errors independent of t, i. e. they have the same constant effect on the absolute normalization of the data in the whole measurement range. They are of the order of 2.4 % for both isotopes and arise principally from uncertainties in the determination of the:

- target thickness
- density of the target nuclei
- number of the incident particles

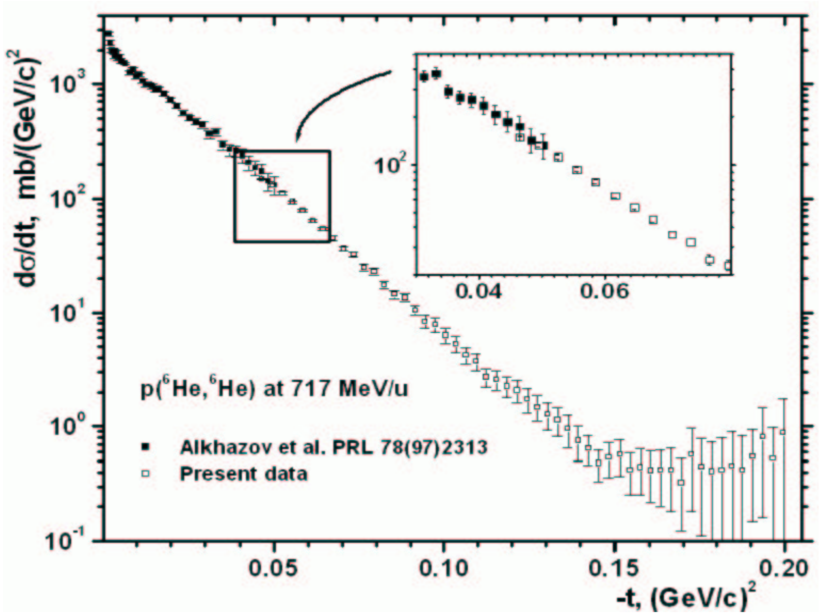

Figure 3.10: *Experimental* $p(^6He,^6He)$ *differential cross section at 717 MeV/u versus the four-momentum transfer* $-t$. *The actual data (open square) coincide with the data at low momentum transfer (black square, taken from Ref. [55]). The insert shows the region of overlap in more detail.*

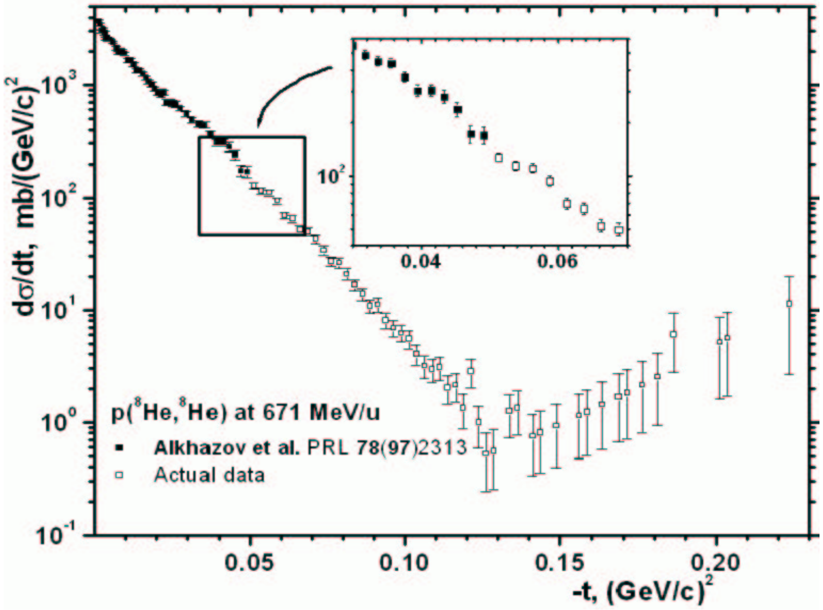

Figure 3.11: *Experimental* $p(^8He,^8He)$ *differential cross section at 671 MeV/u versus the four-momentum transfer* $-t$. *The actual data (open square) coincide with the data at low momentum transfer (black square, taken from Ref. [55]). The insert shows the region of overlap in more detail.*

Chapter 4

RESULTS ON THE RADIAL SHAPE OF THE $^{6,8}HE$ NUCLEI AND THEORETICAL INTERPRETATION

4.1 Theoretical description

At high energy, the collision of an incident proton with a complex nucleus ^A_ZX consisting of many nucleons, despite not easy to solve, can be treated relatively simply by assuming a multiple-scattering mechanism where the scattering amplitude is described as the sum of the contributions from the elementary collisions on the A nucleons. The proton-nucleus scattering amplitude is thus determined from the elementary proton-neutron (pn) and proton-proton (pp) scattering amplitudes. In addition to single-collision terms, contributions arising from multiple scattering are taken into account. The physical conditions which hold at high energy permits the use of several approximations:

- Adiabatic or impulse approximation [76] : the projectile energy ($\sim 700\ MeV/u$) is high enough compared to the nucleons mean kinetic energy ($\sim 10 - 40\ MeV/u$) to assume that they are frozen or fixed during the interaction

- Large inter-nucleon distance compared to the p-N (proton - nucleon) interaction distance. This assumption is fulfilled even better for the case of a halo nucleus where the binding energies of the valence nucleons are low and their typical distance to the core is large.

One of the most used theories in this field was derived by Glauber [77] in the 50's and allows to relate the measured differential cross section to the nuclear matter distribution in an unequivocal way. The reader will find a short overview of the version used here in the appendix D p.113 together with a discussion on the validity of the used approximations. It is important to remind the reader that several input parameters are used in the calculation of the cross section. Their values were gathered from experimental work and for some of them parametrized which means that they carry systematic uncertainties that contribute to the uncertainty on the final results.

The Glauber calculation used in the fit analysis requires the free pp and pn scattering amplitudes which are then folded over the nuclear matter density distribution. Phenomenological model parametrizations with $N = 2$ free parameters are then used for modeling the nuclear matter distribution. In the fit procedure, these parameters are varied independently from each other and the resulting calculated cross section is compared to the experimental data in order to get the best χ^2.

4.2 The nuclear matter distribution ρ_m and its first moment R_m

4.2.1 Definition

The nucleons - both protons and neutrons - are assumed to be the elementary constituents of atomic nuclei and any other subnuclear structure is ignored. They are considered independent - in-medium effects neglected - and frozen - adiabatic approximation - during the interaction. The total matter density distribution ρ_m is then the sum of the neutron and the proton density distributions:

$$\rho_m(r) = N \cdot \rho_n(r) + Z \cdot \rho_p(r) \tag{4.1}$$

N and Z are the number of neutrons and protons respectively. The one-proton (resp. neutron) densities ρ_p (resp. ρ_n) are normalized to unity so that the matter density ρ_m is normalized to the total number of nucleons. Generally, the matter and charge distributions may have non spherical components due to the intrinsic dynamical structure and a complete discussion must include a description of deformation [78]. From theoretical and experimental considerations[1], the ground state of ^6He and ^8He can be assumed to be spherical and consequently one will restrict the analysis to that case only. For cases where the model parametrization enables to separate core and halo nucleons, the protons are always assumed to be localized in the core. Part of the neutrons (2) are localized in the α-like core while the remaining ones are considered to be halo nucleons. Two model parametrizations, GG (Sec. 4.2.2.4 p.56) and GO (Sec. 4.2.2.5 p.56) use this description with an α-like core (2p+2n) and two (^6He) or four (^8He) halo neutrons so that one writes the respective densities as :

$$\rho_{m,^6He}(r) = 2\rho_{p,core}(r) + 2\rho_{n,core}(r) + 2\rho_{n,halo}(r) \tag{4.2}$$

$$\rho_{m,^8He}(r) = 2\rho_{p,core}(r) + 2\rho_{n,core}(r) + 4\rho_{n,halo}(r) \tag{4.3}$$

All model descriptions will be presented individually in the next sections. For a given distribution $\rho(r)$, one defines the root mean square (rms) radius as the following quantity:

$$R_{rms} = < r^2 >^{1/2} = \left\{ \frac{\int r^2 \rho(r) 4\pi r^2 dr}{\int \rho(r) 4\pi r^2 dr} \right\}^{1/2} \tag{4.4}$$

In principle, one can then consider specifically the distribution of protons, neutrons, core or halo nucleons, the distribution of neutrons restricted to the core or the halo. Correspondingly several quantities defined in the same way as in Eq. 4.4 can be infered:

- $R_{p,rms}$ and $R_{n,rms}$: proton and neutron radii from the corresponding densities, ρ_p and ρ_n respectively
- $R_{c,rms}$ and $R_{h,rms}$: core and halo nucleons radii from the corresponding densities, ρ_c and ρ_h respectively

The total matter radius $R_{m,rms}$[2] is the ultimate quantity which determines the nucleus size. It is defined by the relation:

$$R_{m,rms} = \left\{ \frac{Z < r_p^2 > + N < r_n^2 >}{A} \right\}^{1/2} \tag{4.5}$$

---

[1] One assumes these two isotopes in their ground state to be formed by an α core - which is spherical - and the remaining halo neutrons in s or p shell orbitals: the s orbital is spherical while the p orbital is not spherical but has no static deformation. The latter assumption was confirmed experimentally from quadrupole moments measurements [79] for ^{11}Li.

[2] In the next sections we will skip the 'rms' subscript since we only consider rms radii, e. g. $R_{m,rms} \equiv R_m$

4.2.2 Phenomenological parametrization of ρ_m

Several phenomenological model parametrizations of the density distribution were used in the analysis of the $^{6,8}He$ experimental cross sections. Different analytical expressions using two free descriptive parameters describe, every model in its specific way, the halo structure: the first two, namely WS and SF use a diffuseness parameter while the GH uses a specific parameter included in the total matter distribution. The WS, SF and GH parametrizations assume the same distribution for all nucleons. The GG and GO are slightly different in the principle since they assume separate distributions for the core and halo nucleons. In addition, while the GG parametrization assumes a halo distribution with a maximum centered at the origin, the GO provides another perspective with a maximum shifted from the center. The corresponding analytical forms are introduced in the following sections.

4.2.2.1 The Woods-Saxon (WS) parametrization

This distribution has been mentioned in the introduction since it is frequently used in nuclear physics (Sec. 1.1 p.9). It is given by :

$$\rho_m(r) = \left\{a \ln(1+e^{R/a})\right\}^{1/2} \frac{1}{1+exp(\frac{r-R}{a})} \tag{4.6}$$

where the radius R is the value of r for which the density reaches the half value of that at the origin i. e. $\rho_m(R) = \rho_m(0)/2$. The parameter a is called diffuseness and describes the degree of density distribution dilution at the surface of the nucleus. The density distribution given in equation 4.6 is normalized to unity, that means:

$$\int_0^{+\infty} \rho_m(r) 4\pi r^2 dr = 1 \tag{4.7}$$

4.2.2.2 The symmetrized Fermi (SF) parametrization

The matter density distribution is given by [80, 81]:

$$\rho_m(r) = \frac{3}{4\pi R^3} \frac{1}{1+(\pi a/R)^2} \frac{\sinh(R/a)}{\cosh(R/a)+\cosh(r/a)} \tag{4.8}$$

This distribution is very similar to the WS and the parameters R (half-density radius) and a play the same role. It differs slightly from the usual Fermi distribution by a uniform density (horizontal slope) at the origin. The nuclear matter radius is then given by:

$$R_m = R\sqrt{\frac{3}{5}\{1+\frac{7}{3}(\frac{\pi a}{R})^2\}} \tag{4.9}$$

4.2.2.3 The gaussian - halo (GH) parametrization

For every nucleon, the distribution of the total matter density is defined through its formfactor:

$$S(q) = (1+\alpha z^2)e^{-z} \tag{4.10}$$

where $z = q^2 R_m^2/6$ and α is a parameter describing the halo component. The analytical expression of the matter density is then given by :

$$\rho_m(r) = \left(\frac{3}{2\pi R_m^2}\right)^{3/2} (1+\alpha\varphi(r))\, e^{\frac{-3r^2}{2R_m^2}} \tag{4.11}$$

where the function $\varphi(r)$ is defined by :

$$\varphi(r) = \frac{3}{4}\left\{5 - 10(\frac{r}{R_m})^2 + 3(\frac{r}{R_m})^4\right\}$$

For a physical description i. e. in order to have $\rho_m(r)$ positive for $r \geq 0$ one should have $0 \leq \alpha \leq 0.4$. The two extreme cases correspond to one gaussian distribution with no halo ($\alpha = 0$) or a gaussian with a very pronounced halo ($\alpha = 0.4$).

4.2.2.4 The gaussian - gaussian (GG) parametrization

As previously mentioned, one assumes $^{6,8}He$ comprising of core nucleons (two protons and two neutrons) and halo nucleons (two and four neutrons for $^{6,8}He$ respectively). The core and halo density distributions $\rho_{c,h}$ with rms radii $R_{c,h}$ are given by:

$$\rho_{c,h}(r) = \left(\frac{3}{2\pi R_{c,h}^2}\right)^{3/2} e^{-\frac{3r^2}{2R_{c,h}^2}} \tag{4.12}$$

The density distributions in Eq. 4.12 are normalized to unity. The total matter density distribution normalized to A nucleons and the rms matter radius are then given by:

$$\rho_m(r) = 4\rho_c(r) + (A-4)\rho_h(r) \tag{4.13}$$

$$R_m = \left(\frac{4R_c^2 + (A-4)R_h^2}{A}\right)^{1/2} \tag{4.14}$$

4.2.2.5 The gaussian - harmonic oscillator (GO) parametrization

As in the GG parametrization, one assumes here two different distributions for the core and halo nucleons. The core density distribution is a gaussian as in Eq. 4.12. For the halo density, one assumes a 1p-shell harmonic oscillator distribution:

$$\rho_h(r) = \frac{5}{3}\left(\frac{5}{2\pi R_h^2}\right)^{3/2}\left(\frac{r}{R_h}\right)^2 e^{-\frac{5r^2}{2R_h^2}} \tag{4.15}$$

For a p-orbital, this halo description is more realistic than a pure gaussian since it forbids the halo nucleon to be at the origin, i. e. $\rho_h(r=0) = 0$. The parameter R_h is related to the position of maximum density R_{max} which corresponds to the maximum probability of the nucleon presence by $R_{max} = \sqrt{2/5}R_h$.

4.3 Description of the fit procedure

For a given model parametrization, the aim of the fitting procedure is to find those parameter values for which the calculated theoretical differential cross section describes the experimental data in the best way. The measured differential cross sections for the low [14] and high (present data) t range are available with the same incident lab. energy. Both data sets are analyzed separately and studied in combination, thus it is possible to study the sensitivity of the fit parameters and their uncertainties on the t range. It is to be noted that from high t data alone, one must be cautious with results on R_m since it is known that the nucleus size is determined by the slope of $d\sigma/dt$ at the origin. The application of the model parametrizations SF, GH, GG and GO on the data at low t repeats an earlier work [82]. These data are reanalyzed with a different fit routine and the results are reported here for completeness.

4.3.1 Fitting with one experimental data set

The χ^2 method was applied with a χ^2 function defined as follows:

$$\chi^2 = \sum_{j=1}^{N} \left\{ \frac{A \cdot \sigma_{exp}(t_j) - \sigma_{th}(t_j)}{\Delta\sigma_{exp(t_j)}} \right\}^2 + \left(\frac{A-1}{\Delta A_{exp}} \right)^2 \tag{4.16}$$

where:

- N is the number of cross section data points
- $\sigma_{exp}(t_j) \equiv \frac{d\sigma}{dt}(t_j)\|_{exp}$ and $\Delta\sigma_{exp}(t_j)$ are the experimental differential cross section at the transfered momentum t_j and its error respectively
- $\sigma_{th}(t_j) \equiv \frac{d\sigma}{dt}(t_j)\|_{th}$ is the calculated differential cross section at the transfered momentum t_j
- A is a normalization factor and ΔA_{exp} (3% and 2.4% for low and high t data, respectively) is the uncertainty in the experimental absolute normalization of the data. The last term in Eq. 4.16 is then interpreted as a search for the best normalization factor with A being an additional free parameter. In the case of an ideal normalization, one should obtain $A \simeq 1$.

The expression in Eq. 4.16 is slightly different than the one used in Ref. [82] which is given by:

$$\chi^2 = \sum_{j=1}^{N} \left\{ \frac{\sigma_{exp}(t_j) - \sigma_{th}(t_j)/A}{\Delta\sigma_{exp(t_j)}} \right\}^2 + \left(\frac{A-1}{\Delta A_{exp}} \right)^2 \tag{4.17}$$

where A appears before σ_{th} instead of σ_{exp}. This small difference induces no fundamental change on the results, except of slightly different values for the normalization parameter. It is also worthwhile to recall that all the terms in eq. 4.16 are weighted by the inverse of the corresponding experimental errors, therefore it is expected a relatively small influence on the results when skipping the data points at higher t ($t \geq 0.15(GeV/c)^2$) which have the largest error bars. The reduced chi-square χ_r^2:

$$\chi_r^2 = \frac{\chi^2}{N - N_{free}} \tag{4.18}$$

is the relevant quantity by which the fit quality was estimated, the optimal value being close to 1. Here N_{free} is the number of free parameters used in the model parametrization.

4.3.2 Fitting with combined experimental data sets

For this specific purpose, a new expression for the χ^2 function was derived:

$$\chi^2 = \sum_{i=1}^{N_L} \left\{ \frac{A_L \cdot \sigma_{exp}(t_i) - \sigma_{th}(t_i)}{\Delta\sigma_{exp(t_i)}} \right\}^2 + \sum_{j=1}^{N_H} \left\{ \frac{A_H \cdot \sigma_{exp}(t_j) - \sigma_{th}(t_j)}{\Delta\sigma_{exp(t_j)}} \right\}^2 + \left(\frac{A_L-1}{\Delta A_{L,exp}} \right)^2 + \left(\frac{A_H-1}{\Delta A_{H,exp}} \right)^2 \tag{4.19}$$

where one assumes two free normalization parameters A_L and A_H for the low and high t data sets respectively, independent from each other. $\Delta A_{L,exp}$ and $\Delta A_{H,exp}$ are the corresponding experimental normalization uncertainties. N_L and N_H are the number of data points from the two measurements.

4.3.3 Uncertainty on the results

In the case of two free parameters $a \pm \sigma_a$, $b \pm \sigma_b$ (σ_a and σ_b being the rms errors) and a correlation parameter $\sigma_{a,b}$ and by using the error propagation formula, one determines the absolute uncertainty on the matter density distribution $\rho_m(r)$ by the following function:

$$\Delta\rho_m(r) = \left\{ (\frac{\partial\rho_m(r)}{\partial a} \cdot \sigma_a)^2 + (\frac{\partial\rho_m(r)}{\partial b} \cdot \sigma_b)^2 + 2 \cdot \frac{\partial\rho_m(r)}{\partial a} \cdot \frac{\partial\rho_m(r)}{\partial b} \cdot \sigma_a \cdot \sigma_b \cdot \sigma_{a,b} \right\}^{1/2} \tag{4.20}$$

where $\frac{\partial\rho_m(r)}{\partial a,b}$ denotes the partial derivative of $\rho_m(r)$ respective to a (resp. b) when b (resp. a) is kept constant. It is thus possible to plot the resulting densities $\rho_{m,c,h}$ together with their error corridor set by the limits $\rho_{m,c,h} \pm \Delta\rho_{m,c,h}$. The same operation is used for the calculation of the uncertainty on the matter radius.

4.4 Results for ^6He

The results for ^6He are presented first for model parametrizations assuming the same density distribution for all nucleons, then for models having a separate description for core and halo nucleons. The style of presentation is similar in order to facilitate the interpretation. The results from data at low t, high t (present measurement) and the combined data are reported systematically.

4.4.1 Results for parametrizations which have a common description for all nucleons

The WS parameter values of the ^6He fit results are shown in table 4.1. The results concern the fits performed with the low t data in the first row, the present data in the second row and finally results from the combined data in the last row. The quantities shown are, from left to right, the matter radius and its uncertainty $R_m \pm \sigma_m$ and the two free descriptive parameters $R \pm \sigma_R$ and $a \pm \sigma_a$ defined in Sec. 4.2.2.1 p.55, the correlation parameter $\sigma_{R,a}$, the normalization factors A from one data set, A_L and A_H from combined data sets and the reduced chi-square χ^2_r. The obtained values of χ^2_r and the resulting calculated cross sections shown in figure 4.1 prove that the Woods-Saxon is an appropriate description of the ^6He nucleus.

Data	$R_m(fm)$	$R(fm)$	$a(fm)$	$\sigma_{R,a}$	A, $[A_L, A_H]$	χ^2_r
Low t	2.30 (4)$^{(1)}$	1.27 (49)	0.56 (6)	-0.993	1.03 (2)	0.75
Present	2.45 (2)	1.15 (6)	0.62 (1)	-0.941	0.97 (2)	0.53
Combined	2.39 (2)	1.26 (5)	0.59 (1)	-0.974	1.02 (1), 1.01 (2)	0.82

Table 4.1: ^6He *fit values for the WS parametrization. The results are shown separately for the low t and the present data in the two first rows and for the combined data set in the last row. The normalization factor A and its error is displayed for the two first cases while the two factors* $A_{L,H}$ *are shown for the last one (combined data set).*
$^{(1)}$ *The fit uncertainties are given into parentheses. They represent the error in the least significant digit(s). For example,* $2.30(4)$ fm *stands for* 2.30 ± 0.04 fm.

The parameter values determined from the three fits are consistent with each other, the only apparent inconsistency seen here concerns the values of R_m determined from the two measurements taken separately. One notices the increase in the parameters precision when the data are extended to the high t region. The last observation can also be confirmed from the observation of the deduced matter density distributions shown in figure 4.2 where inserts were added to give a more detailed view at the center of the nucleus. The 'error corridor', resulting from the uncertainty in the determination of the fit parameters does not contain any contribution from systematical errors arising from uncertainties in the estimation of the Glauber model

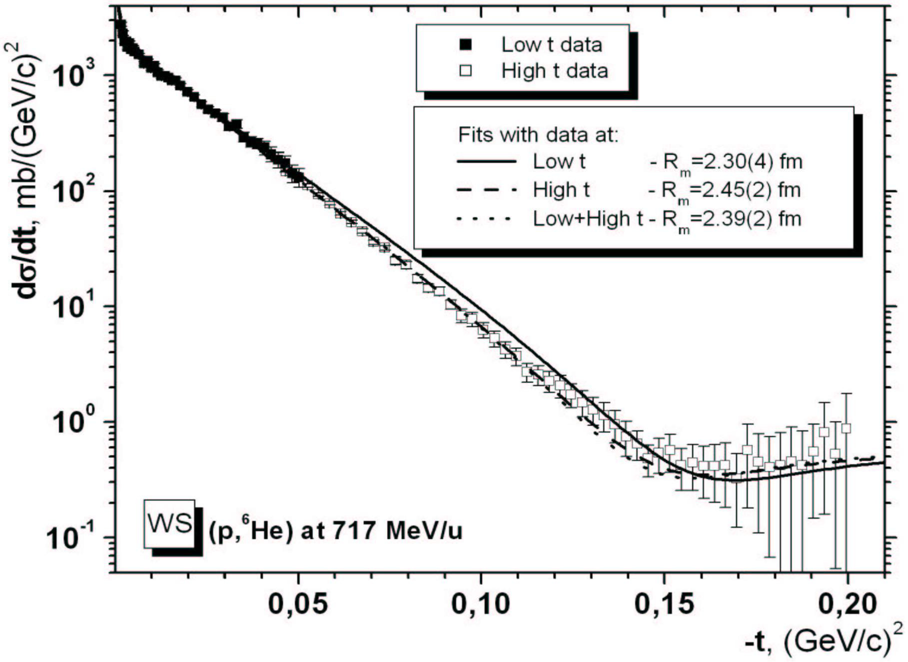

Figure 4.1: *Calculated differential cross sections versus the four-momentum transfer squared* $-t$ *from the WS parametrization of* ^6He*. The results use the data sets at low* t*, high* t *and the combined data set.*

input parameters[3]. It is subtantially reduced, mainly in the central region as expected and for $r \geq 6fm$. The uncertainty is reduced by a factor ~ 10 at the origin. Finally, one notices that R_m increases when the data used for fitting are extended to the region of high t.

The parameter values of the ^6He fit results for the SF parametrization are shown in table 4.2 and the corresponding cross section plots in figure 4.3. The deduced SF matter densities are shown in figure 4.4 with the same observation on the gain in precision while extending the data to the high t region.

Data	$R_m(fm)$	$R(fm)$	$a(fm)$	$\sigma_{R,a}$	A, $[A_L, A_H]$	χ_r^2
Low t	2.31 (6)	1.25 (54)	0.56 (7)	-0.993	1.03 (2)	0.75
Present	2.45 (2)	1.09 (7)	0.62 (1)	-0.950	0.97 (2)	0.54
Combined	2.39 (2)	1.22 (6)	0.59 (1)	-0.944	1.01 (1), 1.03 (2)	0.83

Table 4.2: ^6He *fit values for the SF parametrization. The results are shown separately for the low* t *and the present data in the two first rows and for the combined data set in the last row. The normalization factor* A *and its error is displayed for the two first cases while the two factors* $A_{L,H}$ *are shown for the last one (combined data set).*

The fit parameters for the GH parametrization are shown in table 4.3: the relevant quantities shown are the matter radius $R_m \pm \sigma_m$, the halo parameter $\alpha \pm \sigma_\alpha$ as the two free descriptive parameters (Sec. 4.2.2.3 p.55) and the resulting correlation parameter $\sigma_{m,\alpha}$. From the analysis of the α parameter, one remarks that all the values are consistent and that the core and halo contributions are better determined now and are slightly different than the ones obtained at low t. In addition, the total matter radius R_m undergoes an increase as observed for the two preceding model parametrizations if the analysis of the low t region is extended by combining it to the present data. The corresponding calculated cross section plots are shown

---

[3] The reader should remind that all the nuclear density distributions shown in this work do not contain such systematical error contribution (App. D p.113).

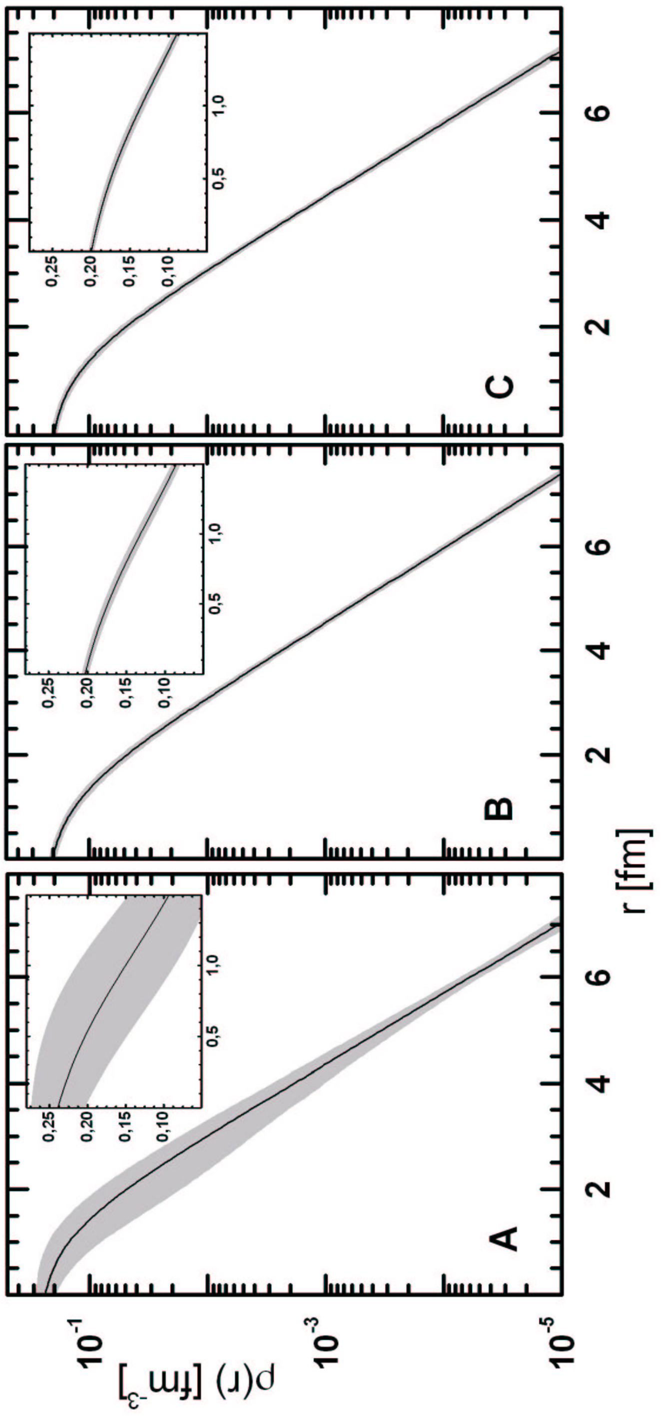

Figure 4.2: *Total nuclear matter density distributions of* ^6He *deduced with the WS fit parameters shown in table 4.1. Solid lines corresponding to results from fitting the low* t *data (A), the high* t *data (B) and the combined data (C) are shown together with the error corridor in light gray. Inserts give, in a linear scale, a more detailed view of the matter distribution around the center of the nucleus.*

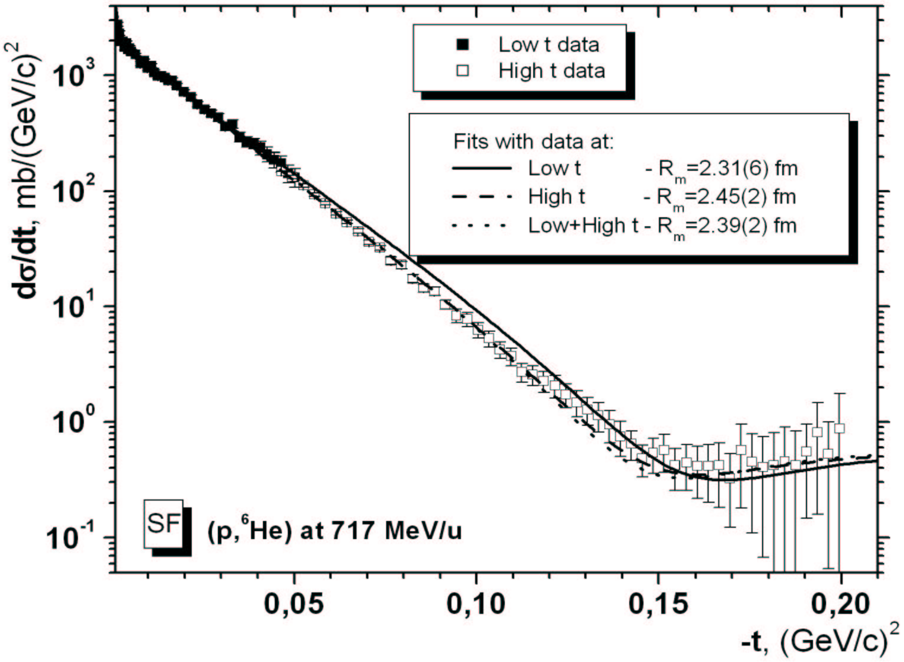

Figure 4.3: *Calculated differential cross sections versus the four-momentum transfer squared $-t$ from the SF parametrization of ^6He. The results use the data sets at low t, high t and the combined data set.*

in figure 4.5 and the matter density distributions in figure 4.6 where one notices the reduction of the error corridor due to the inclusion of the present data in the fit analysis.

Data	$R_m(fm)$	α	$\sigma_{m,\alpha}$	A, $[A_L, A_H]$	χ^2_r
Low t	2.29 (5)	0.08 (5)	0.875	1.04 (1)	0.76
Present	2.41 (3)	0.08 (1)	0.924	0.99 (2)	0.59
Combined	2.34 (2)	0.06 (1)	0.971	1.03 (1), 1.02 (2)	0.80

Table 4.3: ^6He *fit values for the GH parametrization. The results are shown separately for the low t and the present data in the two first rows and for the combined data set in the last row. The normalization factor A and its error is displayed for the two first cases while the two factors $A_{L,H}$ are shown for the last one (combined data set).*

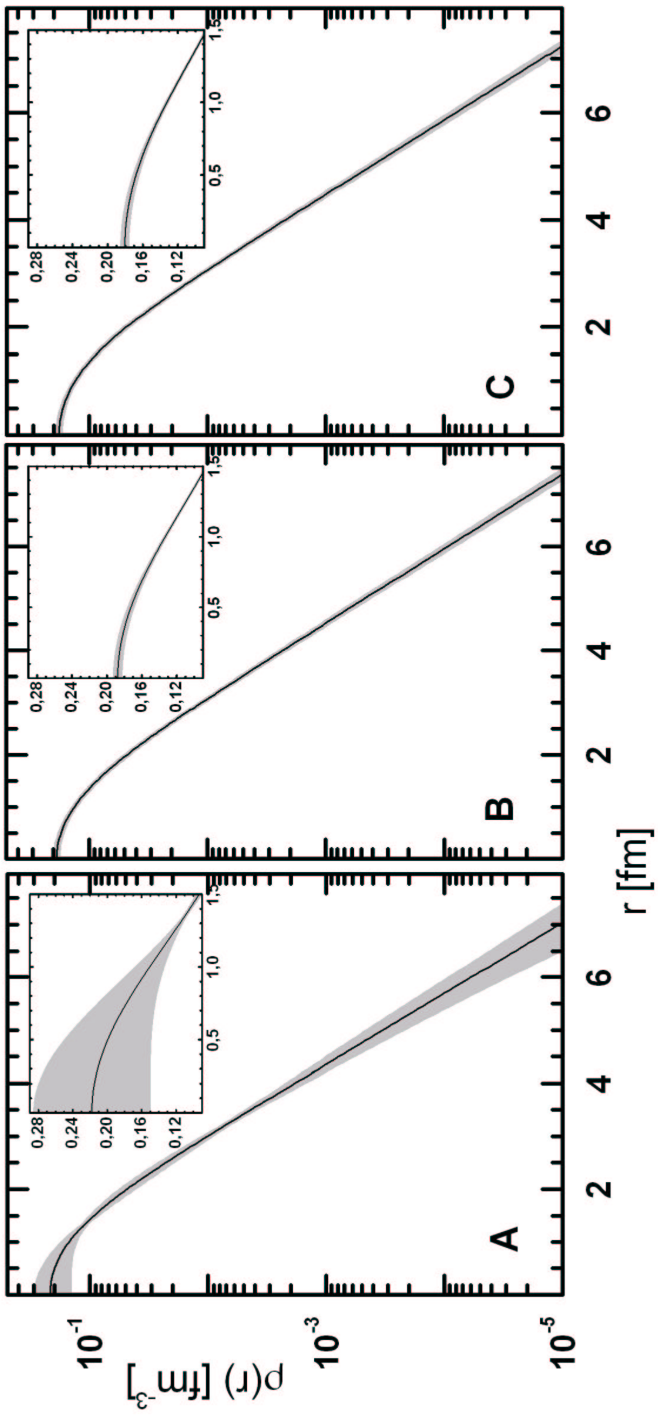

Figure 4.4: *Total nuclear matter density distributions of* ^{6}He *deduced with the SF fit parameters shown in table 4.2. Solid lines corresponding to results from fitting the low* t *data (A), the high* t *data (B) and the combined data (C) are shown together with the error corridor in light gray. Inserts give, in a linear scale, a more detailed view of the matter distribution around the center of the nucleus.*

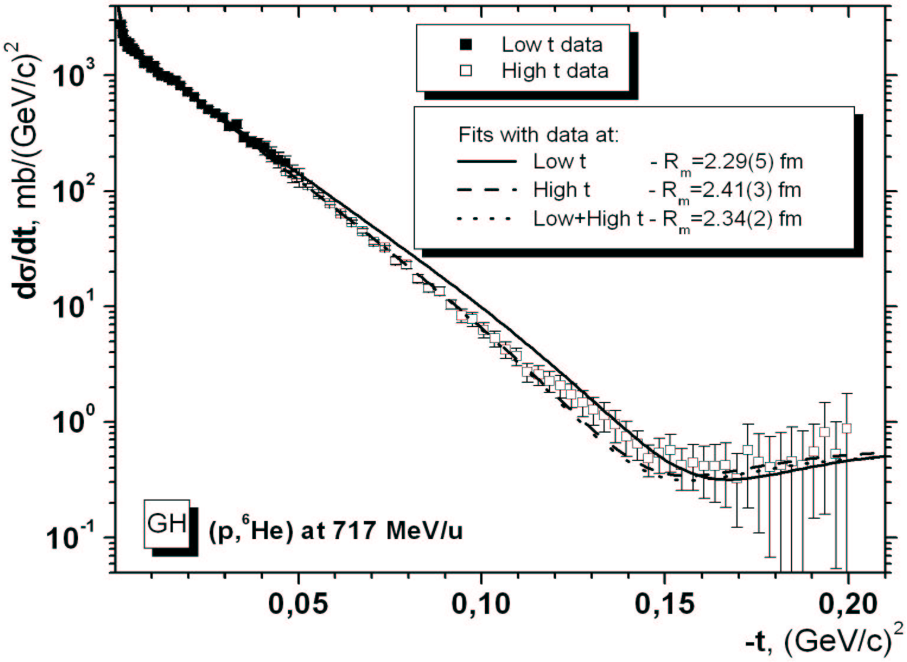

Figure 4.5: *Calculated differential cross sections versus the four-momentum transfer squared* $-t$ *from the GH parametrization of* ^6He. *The results use the data sets at low* t, *high* t *and the combined data set.*

4.4.2 Results for parametrizations which allow for a separate description of core and halo nucleons

In this section, cases where one allows different distributions for the core and halo nucleons will be discussed. The fit parameter values for the GG parametrization are shown in table 4.4. The relevant quantities shown are the matter radius $R_m \pm \sigma_m$, the core $R_c \pm \sigma_c$ and halo $R_h \pm \sigma_h$ radii as the two free descriptive parameters defined in Sec. 4.2.2.4 p.56 and the correlation parameter $\sigma_{c,h}$. All the fits show consistent results for R_c and R_h while the results for the total matter radius R_m are consistent only in the low t and the combined data cases.

An increase of precision is obtained when the fitted experimental data are extended to higher t values. The biggest improvement is noticed on the core radius where a factor 10 is gained while this factor is only 4 for the halo radius. The fit qualities are good as seen from the χ_r^2 values and from the comparison of the calculated cross sections with the experimental data (Fig. 4.7). The resulting density distributions of the total nuclear matter are shown in figure 4.8 where now, in addition, is displayed the equivalent core matter density distribution. The calculated error corridors show a noticeable gain in precision as already discussed, the best relative increase being observed at the nucleus periphery.

The parameter values for the GO parametrization are shown in table 4.5 where the relevant quantities shown are the same as for the GG parametrization. These values are consistent from one case to another and the corresponding calculated cross sections are shown in figure 4.9 where one remarks that even the fit curve from the low t data is able to describe relatively well the new data. The total and core matter density distributions for ^6He are shown in figure 4.10.

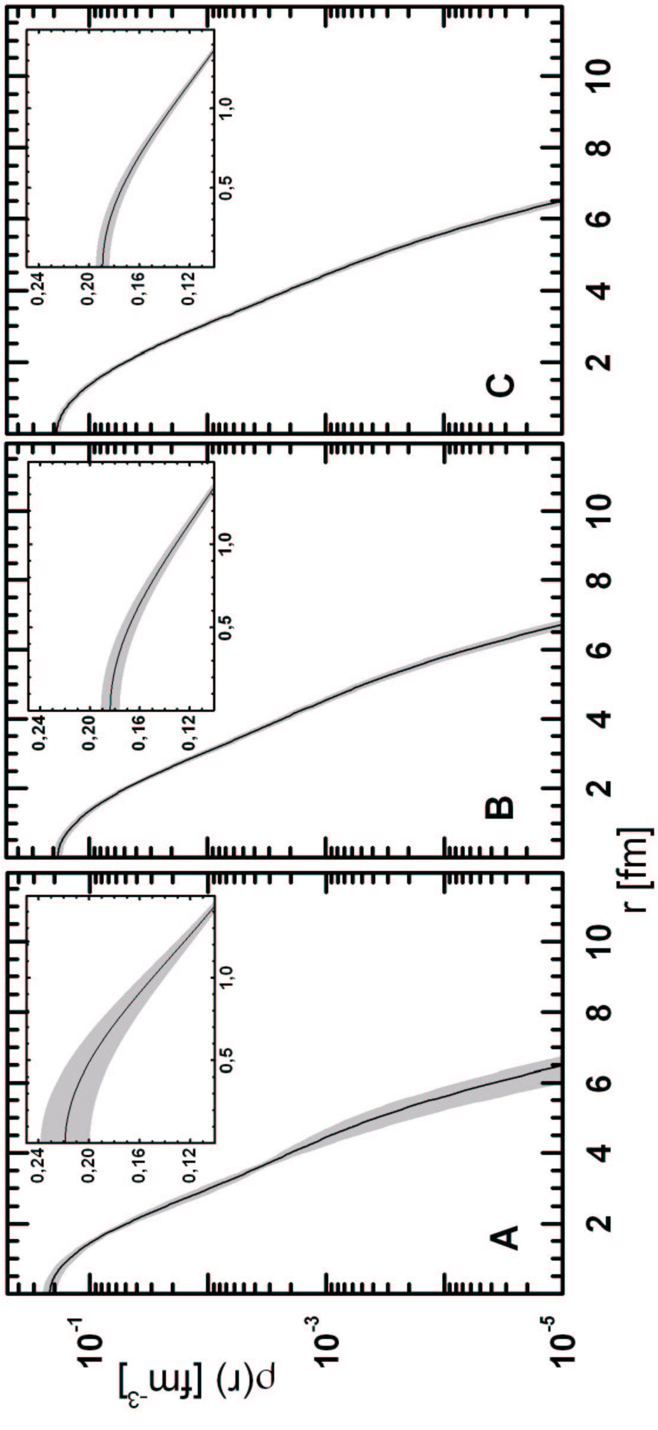

Figure 4.6: *Total nuclear matter density distributions of* ^6He *deduced with the GH fit parameters shown in table 4.3. Solid lines corresponding to results from fitting the low* t *data (A), the high* t *data (B) and the combined data (C) are shown together with the error corridor in light gray. Inserts give, in a linear scale, a more detailed view of the matter distribution around the center of the nucleus.*

Data	$R_m(fm)$	$R_c(fm)$	$R_h(fm)$	$\sigma_{c,h}$	A, $[A_L, A_H]$	χ_r^2
Low t	2.30 (5)	1.95 (10)	2.88 (27)	-0.951	1.04 (1)	0.77
Present	2.44 (4)	2.02 (1)	3.12 (9)	-0.146	0.99 (2)	0.53
Combined	2.36 (2)	2.02 (1)	2.93 (6)	-0.472	1.03 (1), 1.03 (2)	0.78

Table 4.4: *^6He fit values for the GG parametrization with R_c and R_h as the two free descriptive parameters. The results are shown separately for the low t and the present data in the two first rows and for the combined data set in the last row. The normalization factor A and its error is displayed for the two first cases while the two factors $A_{L,H}$ are shown for the last one (combined data set).*

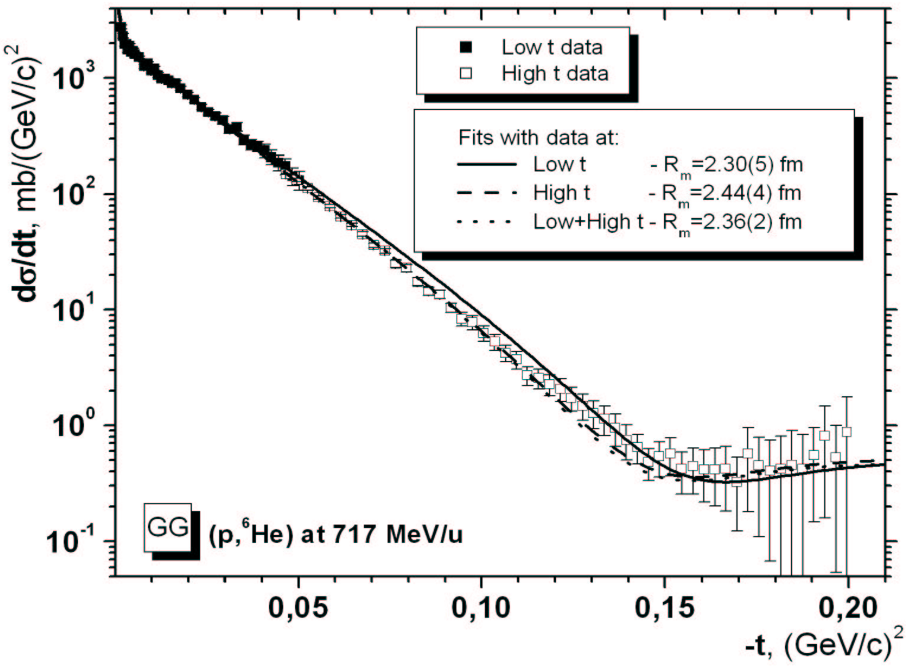

Figure 4.7: *Calculated differential cross sections versus the four-momentum transfer squared $-t$ from the GG parametrization of ^6He. The results use the data sets at low t, high t and the combined data set.*

Data	$R_m(fm)$	$R_c(fm)$	$R_h(fm)$	$\sigma_{c,h}$	A, $[A_L, A_H]$	χ_r^2
Low t	2.29 (5)	1.81 (8)	3.03 (21)	-0.934	1.04 (1)	0.76
Present	2.37 (2)	1.92 (1)	3.07 (5)	0.242	0.99 (2)	0.37
Combined	2.33 (2)	1.91 (1)	2.99 (4)	-0.042	1.03 (1), 1.02 (2)	0.63

Table 4.5: *^6He fit values for a GO parametrization with R_c and R_h as the two free descriptive parameters. The results are shown separately for the low (S105) and high (S174) t range and for the combined data sets in the last row. The normalization factor A and its error are displayed for the two first cases (one experimental data set) while the two factors $A_{H,L}$ are shown for the last one (combined data set).*

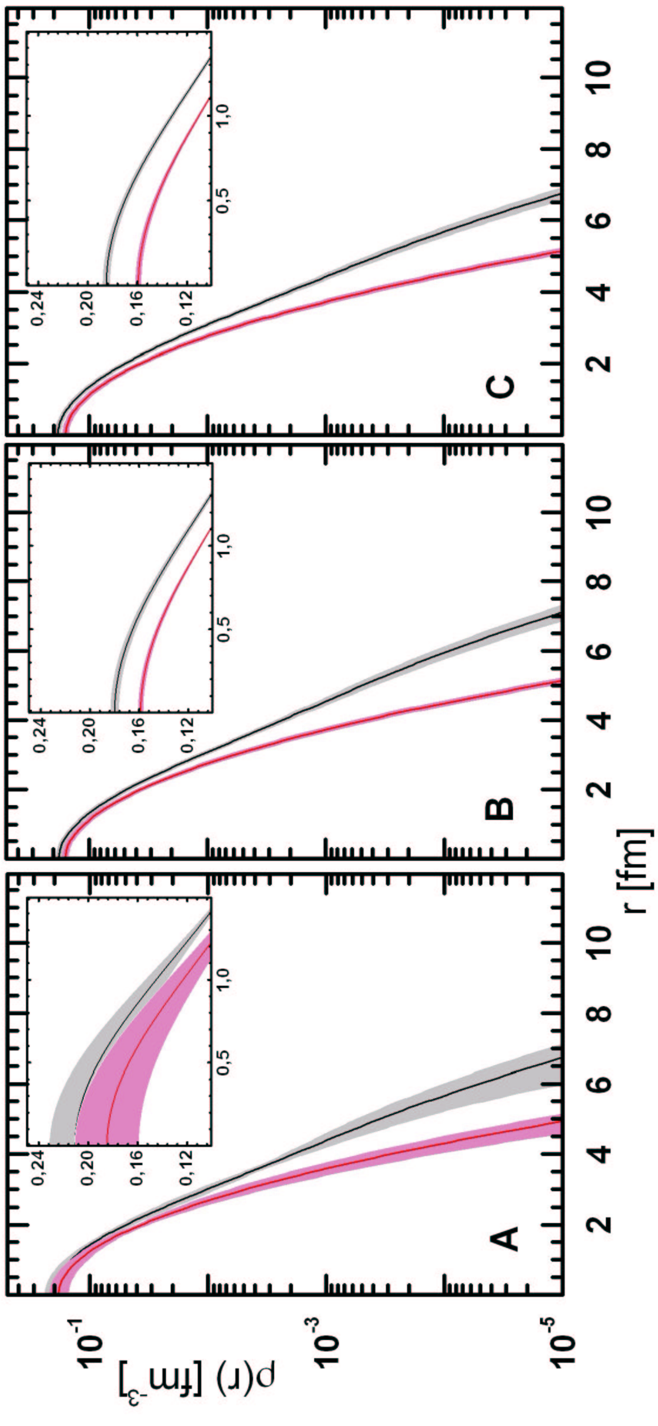

Figure 4.8: *Total (black) and core (red) nuclear matter density distributions of* ^{6}He *deduced with the GG fit parameters shown in table 4.4. Solid lines corresponding to results from fitting the low* t *data (A), the high* t *data (B) and the combined data (C) are shown together with the error corridor in light gray (total) and light pink (core). Inserts give, in a linear scale, a more detailed view of the matter distribution around the center of the nucleus. The total density distribution is normalized to the total number of nucleons while the core density is normalized to the number of core nucleons.*

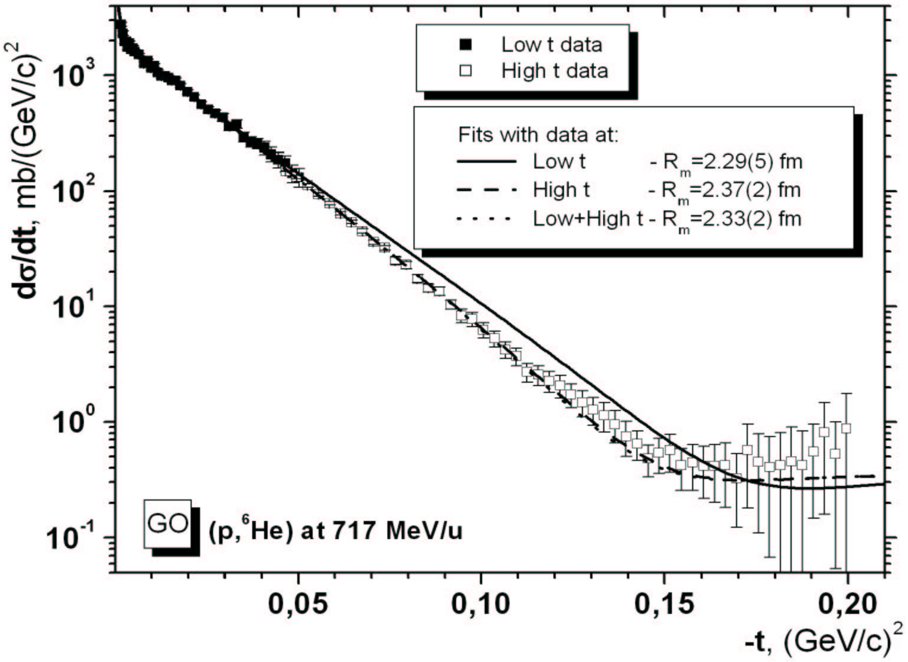

Figure 4.9: *Calculated differential cross sections versus the four-momentum transfer squared $-t$ from the GO parametrization of ^6He. The results use the data sets at low t, high t and the combined data set.*

4.4.3 Results discussion

To help the reader through these numerous results, the table 4.6 summarizes the different radii values, the normalization parameter(s) and the reduced chi-square only for the cases where low t and combined data were used. The obtained χ_r^2 and the resulting calculated cross sections prove that each parametrization is able to model the nuclear matter distribution. For all the performed fits, the A and $A_{L,H}$ values are also very close to 1 which provides the evidence of the good data normalization, the maximum observed deviation being 1% from one parametrization to another (low t data) and 3% (combined data).

Model	R_m (fm)	R_c (fm)	R_h (fm)	A_L A	A_H	χ_r^2
WS	2.39 (2) 2.30 (4)			1.02 (1) 1.03 (2)	1.01 (2)	0.82 0.75
SF	2.39 (2) 2.31 (6)			1.01 (1) 1.03 (1)	1.03 (2)	0.83 0.75
GH	2.34 (2) 2.29 (5)			1.03 (1) 1.04 (1)	1.02 (2)	0.80 0.76
GG	2.36 (2) 2.30 (6)	2.02 (1) 1.95 (10)	2.93 (6) 2.88 (27)	1.03 (1) 1.04 (1)	1.03 (2)	0.78 0.77
GO	2.33 (2) 2.30 (5)	1.91 (1) 1.81 (8)	2.99 (4) 3.03 (21)	1.03 (1) 1.04 (1)	1.02 (2)	0.63 0.76

Table 4.6: *Summary of the total, core and halo radii (R_m, R_c, R_h) values after fitting the experimental (p,^6He) elastic differential cross section at 717 MeV/u. For every model parametrization, the fit results from the combined data set (first line of each row) and from the low t data (second line) are presented. The normalization parameter(s) and the reduced chi-square are also reported. The errors shown do not contain the systematical uncertainty contribution coming from the Glauber calculation.*

Being very similar, the WS and SF parametrizations yield almost equal parameters within 1-2 % while the rms matter radii are equal in all employed cases: separate and combined data (Tabs. 4.1 p.58 and 4.2 p.59). If one considers the GG and GO parametrizations where the core and halo radii are available for different combinations of the data, an important gain in precision is obtained when the experimental data are extended to the high t domain. This gain in precision was indeed expected for it was the main motivation

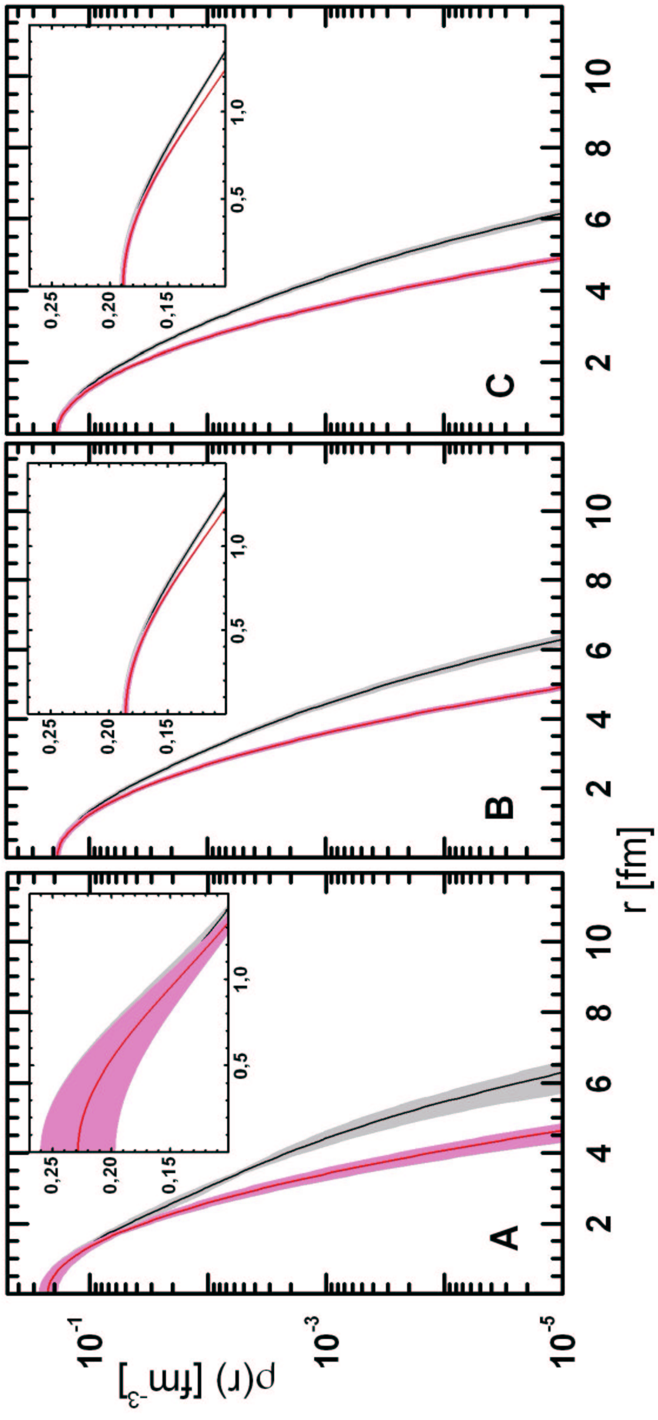

Figure 4.10: *Total (black) and core (red) nuclear matter density distributions of* ^{6}He *deduced with the GO fit parameters shown in table 4.5. Solid lines corresponding to results from fitting the low* t *data (A), the high* t *data (B) and the combined data (C) are shown together with the error corridor in light gray (total) and light pink (core). Inserts give, in a linear scale, a more detailed view of the matter distribution around the center of the nucleus. The total density distribution is normalized to the total number of nucleons while the core density is normalized to the number of core nucleons.*

of the present experiment to extend the measurement of the elastic cross section to the region of the first diffraction minimum in order to get a more precise view on the internal part of the studied nuclei.

Considering the total matter radius R_m, a reasonable consistency is obtained for all the cases which is an indication that the present analysis is practically model-free. The new data tend to slightly increase the matter radius for every used parametrization. The ^6He radius together with the core and halo radii were averaged from the different model parametrizations (Tab. 4.7). The weighted mean value R was calculated using the following formula:

$$R(^6He) = \frac{\sum R_i/\Delta R_i^2}{\sum 1/\Delta R_i^2} \tag{4.21}$$

which minimizes the contribution of those parametrizations with bigger uncertainty. Here the summation is made over the considered parametrizations i by using the corresponding radius R_i and its uncertainty ΔR_i. The uncertainty ΔR shown in the second position, is taken as the arithmetic mean[4] of the corresponding uncertainties. The deviation σ_R measures the spread of the different individual values to the mean value (models uncertainty). It is shown in the third position and was calculated with the following expression, N being the number of considered cases:

$$\sigma_R^2 = \frac{\sum (R_i - R)^2}{(N-1)^2} \tag{4.22}$$

Data		Low t	Combined
$R_m(fm)$	(1)	2.30 (6) (1)	2.36 (2) (3)
	[82]	2.30 (6) (1)	
$R_c(fm)$	(2)	1.87 (9) (10)	1.97 (1) (8)
	[82]	1.87 (10) (10)	
$R_h(fm)$	(2)	2.97 (24) (11)	2.97 (5) (5)
	[82]	2.99 (24) (12)	

Table 4.7: *Summary table showing the ^6He radii (total, core and halo) as determined from the combination of all models. Every result R (ΔR) (σ_R) shows respectively the mean radius, its uncertainty(3) and the deviation as defined in Eqs. 4.21 and 4.22 p.69. In the third column, the results obtained from our analysis of the low t data are compared to the original one appearing in [82].*
(1) Combination of WS, SF, GH, GG and GO while in [82], only the four last ones are used.
(2) Combination of GG and GO as in [82].
(3) ΔR does not contain the systematical uncertainty contribution coming from the Glauber calculation.

This presentation helps to make a direct comparison of the actual results with the ones concerning the analysis of the data at low t [82] where only the collection (WS-GO) was used. The analysis in [82] was fully reproduced as can be seen in the third column for all radii. Combining the actual measurement induces a slight increase of the total and core radii and a gain in precision in all the determined radii.

In sum up, from the results obtained with the all presented model parametrizations, including the systematical uncertainties, the deduced ^6He radii are R_m=2.36(6) fm, R_c=1.97(9) fm and R_h=2.97(8) fm. The systematical errors are due to uncertainties in the determination of the model input parameters σ_{pN}, ε_{pN} and β_{pN} which account for 0.01, 0.02 and 0.03 fm respectively and to an additional uncertainty in the t-scale determination which accounts for 0.02 fm.

The newly obtained radii have a much reduced uncertainty which is reflected on Fig. 4.11 where the nuclear matter density distributions from the model parametrizations WS, SF, GH, GG and GO are plotted. The error corridor, represented by a shaded area, was determined as the envelope resulting from the superimposition of all individual density uncertainties. Without including the systematical uncertainties on the pN amplitude parameters and for the case where combined data were used, a factor 6 in precision is gained on the nuclear density at the centre of the nucleus.

---

[4] Different parametrizations are used but the fitting data are common for all results, thus these values are not independent

In every case, low t and combined data, all parametrizations give a similar description of the nuclear matter in the region $r \leq 5\ fm$ while the WS and SF yield almost the same distribution even for $r \geq 5\ fm$. The difference between these parametrizations is well seen at the outer part of the nucleus where the same trend is observed, i. e. $\rho_{GO} \leq \rho_{GH} \leq \rho_{GG} \leq \rho_{WS} \simeq \rho_{SF}$, in the two cases.

The elastic proton scattering measurement at intermediate energies is not sensitive to describe the very far periphery of the nucleus commonly called “nuclear tail”. The low t region is expected to be the most sensitive to study this part of the nucleus. It is worth to mention that the inclusion of this density tail already predicted an absolute increase of 0.2 fm [83] and 0.15 fm [82] for ^6He compared to the values determined in this work by using only the low t region for fitting.

The total density distribution taken as an average from the different cited descriptions is shown in Fig. 4.12 for the low t and the combined data sets. The corresponding uncertainty is identical to the one in Fig. 4.11. The core density distribution taken as the mean result from the model parametrizations GG and GO is also displayed together with the matter density distribution of the free ^4He for which $R_m = 1.49\ fm$. The description is fairly similar in the two presented cases but with an uncertainty level much reduced in the case where the combined data are used[5]. In particular, the radial distribution of the α-core decreases at the center and becomes larger at the periphery, as compared to the ^4He nucleus case. As a result, the apparent size of the core is larger, $R_c = 1.97(9)\ fm$. This observation was already reported [82][6] and is interpreted as the result of the relative motion of the core around the nucleus center-of-mass.

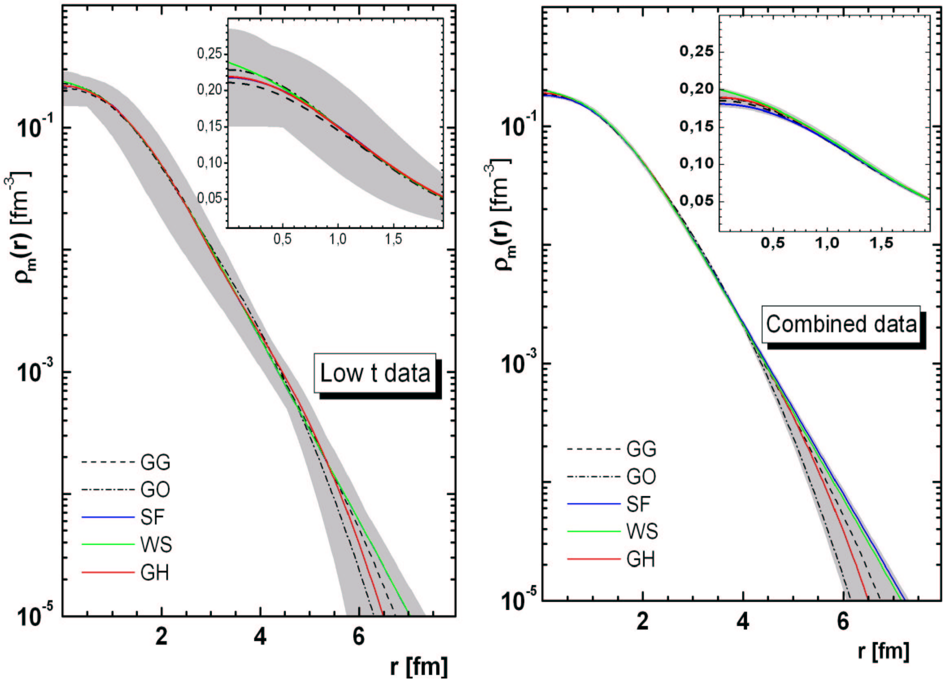

Figure 4.11: *Total nuclear matter density distributions of ^6He deduced from the model parametrizations WS, SF, GH, GG and GO. Results are shown from fits with the low t data (left part) and the combined data (right part). The error corridor (shaded area) is the envelope including the uncertainties from all parametrizations without systematical uncertainties in the parameters of the pN amplitudes used in the Glauber calculation. Inserts give, in a linear scale, a more detailed view of the density distribution around the center of the nucleus.*

---

[5] In fact, one remarks that in the case where the combined data are used, errors reduce to the difference between the GG and GO determinations

[6] The apparent size of the ^6He α-core was determined to be 1.88 (12) fm

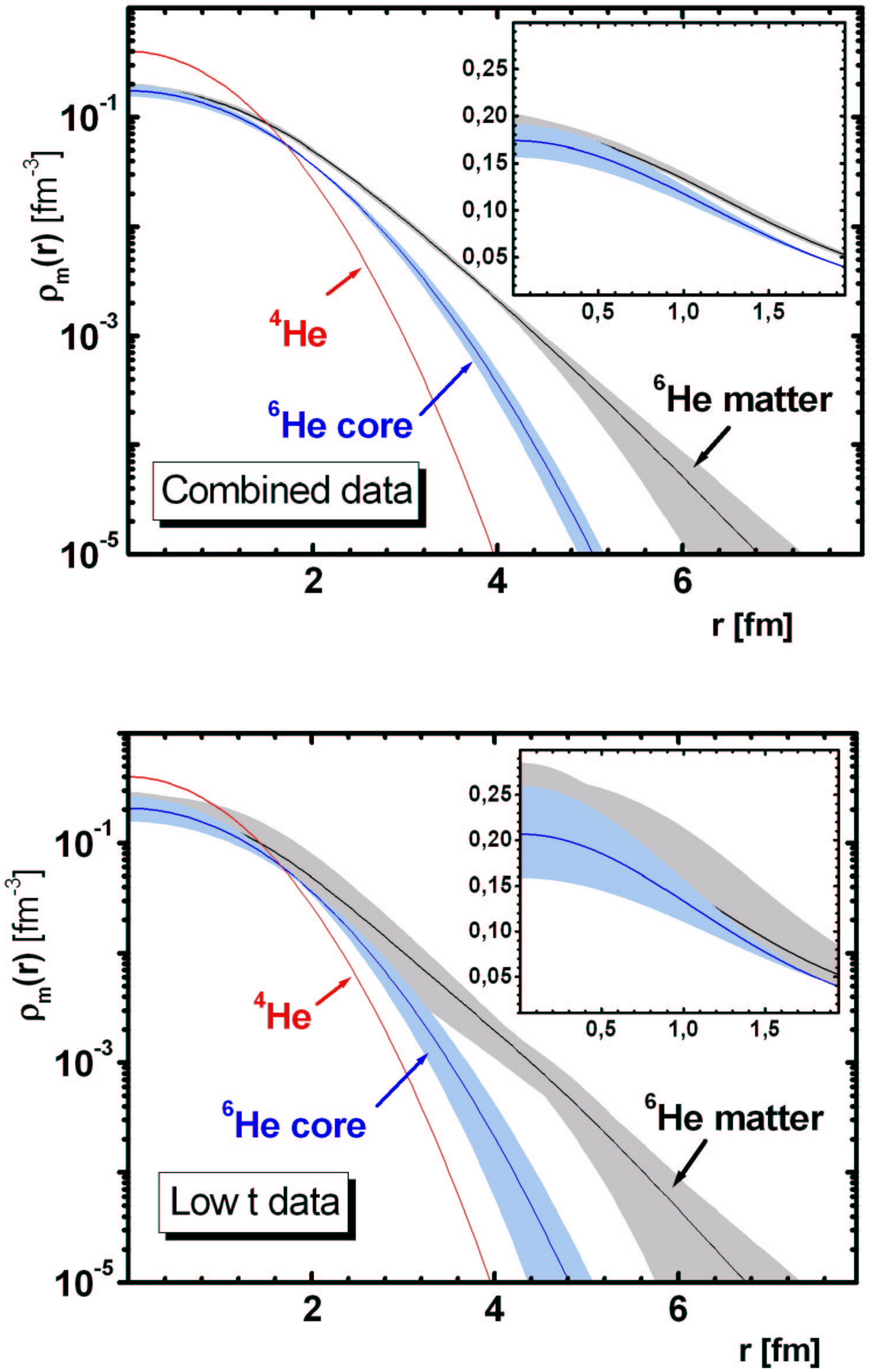

Figure 4.12: *The average total (black) and core (blue) matter density distributions of* ^6He *as results from fits with the low* t *data (bottom figure) and the combined data (top figure). The error corridor (shaded area) is the envelope including the uncertainties from all the cited parametrizations and is identical to the one shown in Fig. 4.11 for the case of the total nuclear matter. Inserts give, in a linear scale, a more detailed view of the density distribution around the center of the nucleus. These distributions are compared to the case of free* ^4He *shown in red.*

4.5 Results for ^8He

As for ^6He, one will present first model parametrizations assuming the same density distribution for all nucleons, then models having a separate description for core and halo nucleons. The style of presentation is similar to that of ^6He in order to facilitate the interpretation and concerns the results from data at low t, high t (present data) and the combined data.

4.5.1 Results for parametrizations which have a common description for all nucleons

The parameter values for the WS parametrization are shown in table 4.8. The results concern the fits performed with the low t data in the first row, the present data in the second row and finally the combined data from both experiments in the last one. The quantities shown are from left to right: the matter radius $R_m \pm \sigma_m$, the two free descriptive parameters $R \pm \sigma_R$ and $a \pm \sigma_a$ (Sec. 4.2.2.1 p.55), the correlation parameter $\sigma_{R,a}$, the normalization parameters A, $A_{H,L}$ and the reduced chi-square χ^2_r. As for ^6He, ^8He shows obviously a large diffuseness compared to its half-density radius especially when only data at low t are used.

The obtained χ^2_r values and the resulting calculated cross sections shown in figure 4.13 prove that the fit quality is worse as compared to the ^6He case. The fit performed with the data at low t fails to describe present data. Both fits performed with the data at high t and with the combined data underestimate the elastic cross section for $t \geq 0.15 (GeV/c)^2$.

Data	$R_m(fm)$	$R(fm)$	$a(fm)$	$\sigma_{R,a}$	A, $[A_L, A_H]$	χ^2_r
Low t	2.49	0.00 (94)	0.69 (4)	-0.988	0.96 (1)	1.02
Present	2.49 (5)	1.15 (8)	0.63 (2)	-0.958	0.97 (3)	0.96
Combined	2.44 (2)	1.24 (6)	0.61 (1)	-0.944	0.98 (1), 1.00 (2)	1.09

Table 4.8: ^8He *fit values for the WS parametrization. The results are shown separately for the low t and the present data in the two first rows and for the combined data set in the last row. The normalization factor A and its error is displayed for the two first cases while the two factors* $A_{L,H}$ *are shown for the last one (combined data set).*

The values determined with the data at high t seem to be consistent with the ones determined from the data at low t. One can even notice the considerable increase in the precision of parameters when the data are extended to the high t region. The last observation can be easily seen when looking to the deduced matter density distributions shown in figure 4.14. In every figure, the error limits set by the fit procedure are represented by the light grey corridor and do not include the contribution due to systematical errors from the pN amplitude parameters used in the Glauber calculation. This 'error corridor' is slightly reduced compared to the case of ^6He when taking the new data into account. The reader should notice the ordinate logarithmic scale which permits to visualize the densities over a wide range of values. Inserts give, in a linear scale, a more detailed view of the matter distribution at the nucleus center.

The resulting parameter values of the ^8He fit from the SF parametrization are shown in table 4.9 and the corresponding cross section plots in figure 4.15. The deduced density distributions are shown in figure 4.16 with the same observation on the gain in precision while extending the data to the high t region. The ^8He analysis shows particular values when the data at low t are used which must be considered with care, in particular the halfway radius $R = 0.00 \pm 0.73 fm$. In order to clarify this particular point, the initial value of the parameter R was varied in the range ±2 fm and the best χ^2_r was found to correspond to $R = 0$ and $a = 0.66 fm$ as shown in figure 4.17.

There are certainly inherent artefacts in the model exhibited only for this isotope which has a rather important halo component. These results must then be considered with more care. Finally, it is interesting

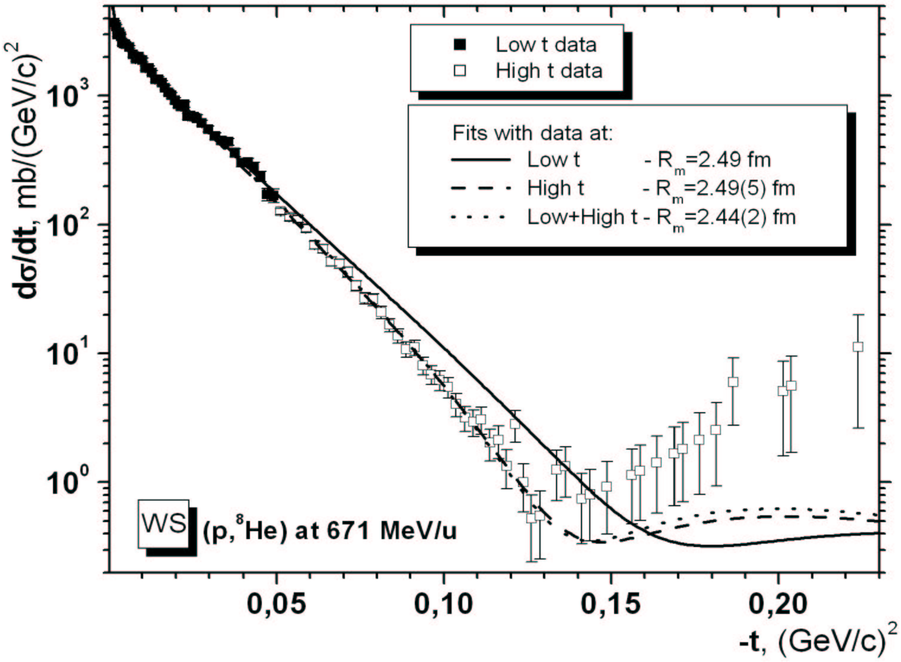

Figure 4.13: *Calculated differential cross sections versus the four-momentum transfer squared $-t$ from the WS parametrization of ^8He. The results use the data sets at low t, high t and the combined data set.*

to note that both the SF and the WS parametrizations give similar results when one uses the data at high t or the combined data sets.

Data	$R_m(fm)$	$R(fm)$	$a(fm)$	$\sigma_{R,a}$	A, $[A_L, A_H]$	χ^2_r
Low t	2.46	0.00 (73)	0.66 (1)	-0.028	0.97 (1)	1.04
Present	2.46 (4)	1.08 (10)	0.63 (2)	-0.965	0.97 (3)	0.95
Combined	2.44 (2)	1.20 (7)	0.61 (1)	-0.951	0.98 (1), 1.00 (2)	1.09

Table 4.9: *^8He fit values for the SF parametrization. The results are shown separately for the low t and the present data in the two first rows and for the combined data set in the last row. The normalization factor A and its error is displayed for the two first cases while the two factors $A_{L,H}$ are shown for the last one (combined data set).*

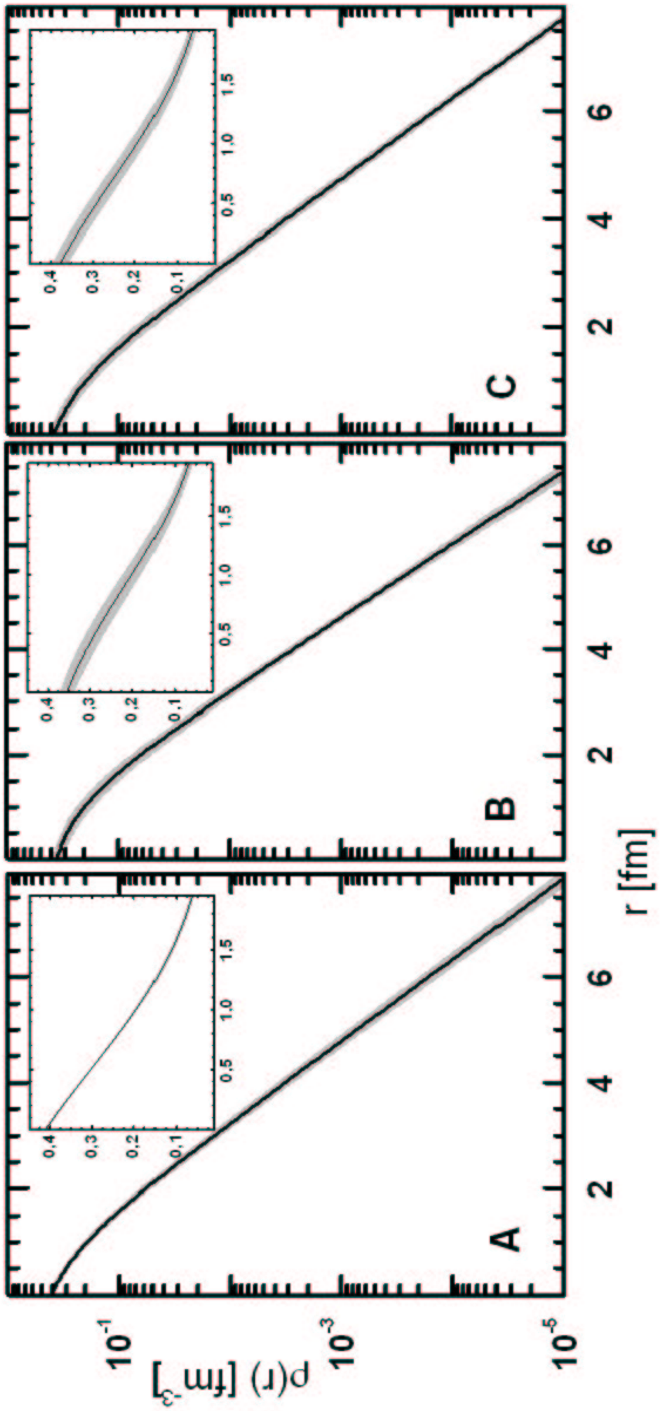

Figure 4.14: *Total nuclear matter density distributions of* ^8He *deduced with the WS fit parameters shown in table 4.8. Solid lines corresponding to results from fitting the low* t *data (A), the high* t *data (B) and the combined data (C) are shown together with the error corridor in light gray. Inserts give, in a linear scale, a more detailed view of the matter distribution around the center of the nucleus.*

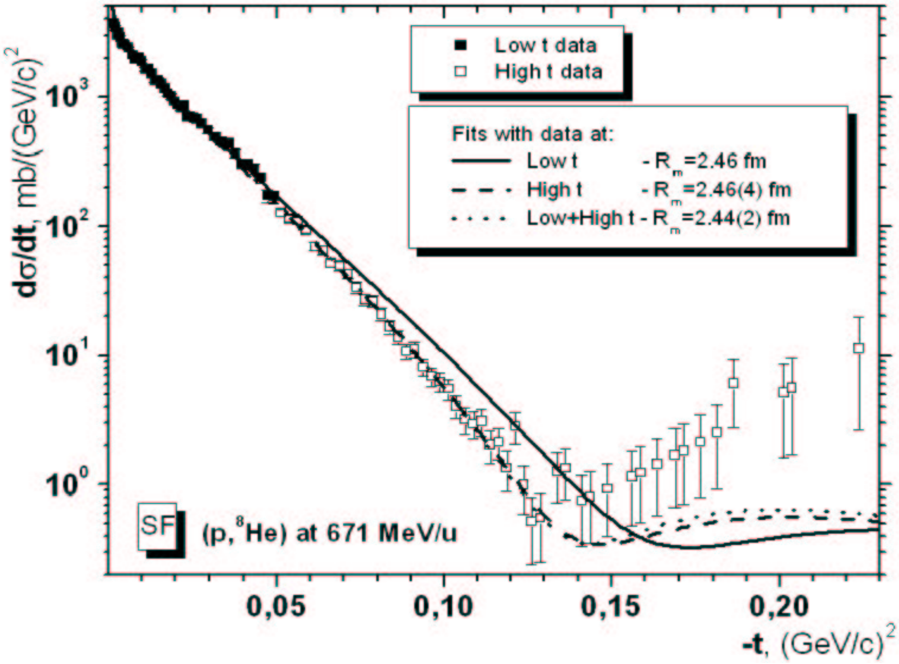

Figure 4.15: *Calculated differential cross sections versus the four-momentum transfer squared $-t$ from the SF parametrization of ^8He. The results use the data sets at low t, high t and the combined data set.*

The parameter values for the GH parametrization are shown in table 4.10. The relevant quantities shown are the matter radius $R_m \pm \sigma_m$, the halo parameter $\alpha \pm \sigma_\alpha$ as the two free descriptive parameters (Sec. 4.2.2.3 p.55) and the correlation parameter $\sigma_{m,\alpha}$. The corresponding calculated cross section plots are shown in figure 4.18 and the matter density distributions in figure 4.19.

Data	$R_m(fm)$	α	$\sigma_{m,\alpha}$	A, $[A_L, A_H]$	χ_r^2
Low t	2.48 (4)	0.16 (3)	0.866	0.96 (1)	1.01
Present	2.50 (6)	0.10 (2)	0.974	0.97 (2)	0.94
Combined	2.42 (2)	0.08 (1)	0.888	0.98 (1), 1.00 (2)	1.10

Table 4.10: ^8He *fit values for the GH parametrization. The results are shown separately for the low t and the present data in the two first rows and for the combined data set in the last row. The normalization factor A and its error is displayed for the two first cases while the two factors $A_{L,H}$ are shown for the last one (combined data set).*

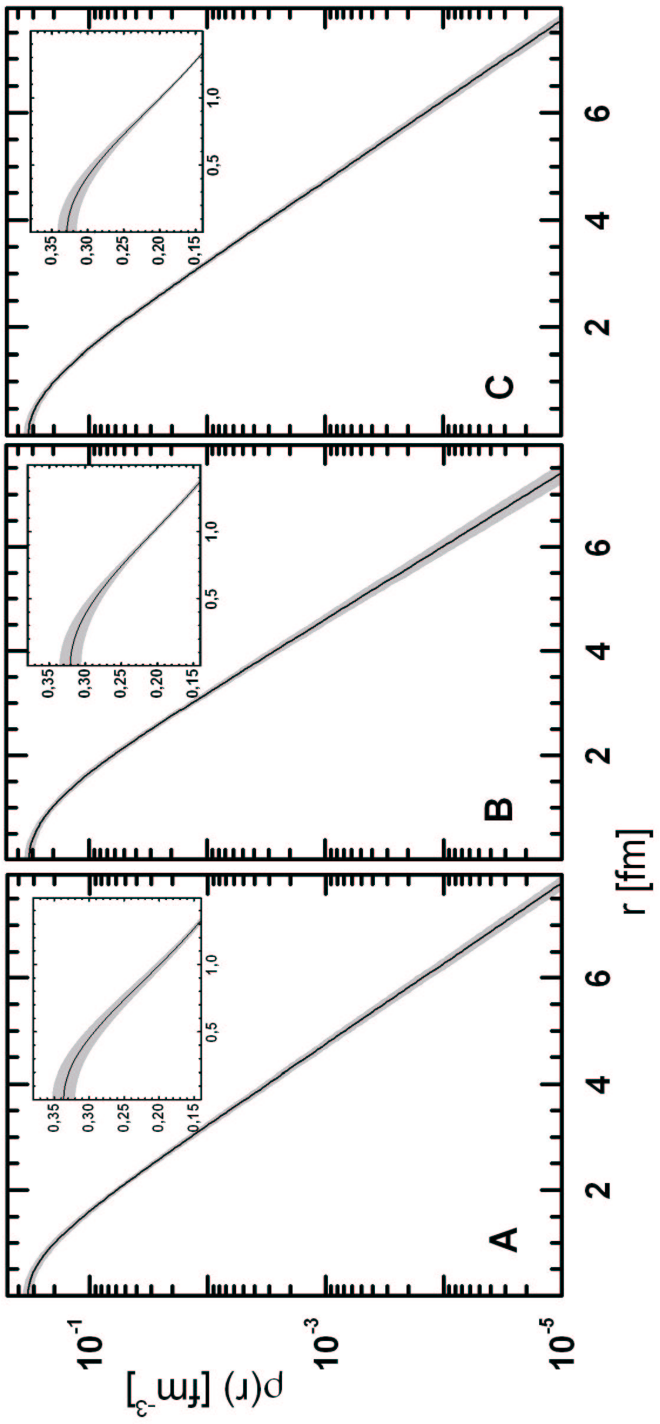

Figure 4.16: *Total nuclear matter density distributions of* ^{8}He *deduced with the SF fit parameters shown in table 4.9. Solid lines corresponding to results from fitting the low* t *data (A), the high* t *data (B) and the combined data (C) are shown together with the error corridor in light gray. Inserts give, in a linear scale, a more detailed view of the matter distribution around the center of the nucleus.*

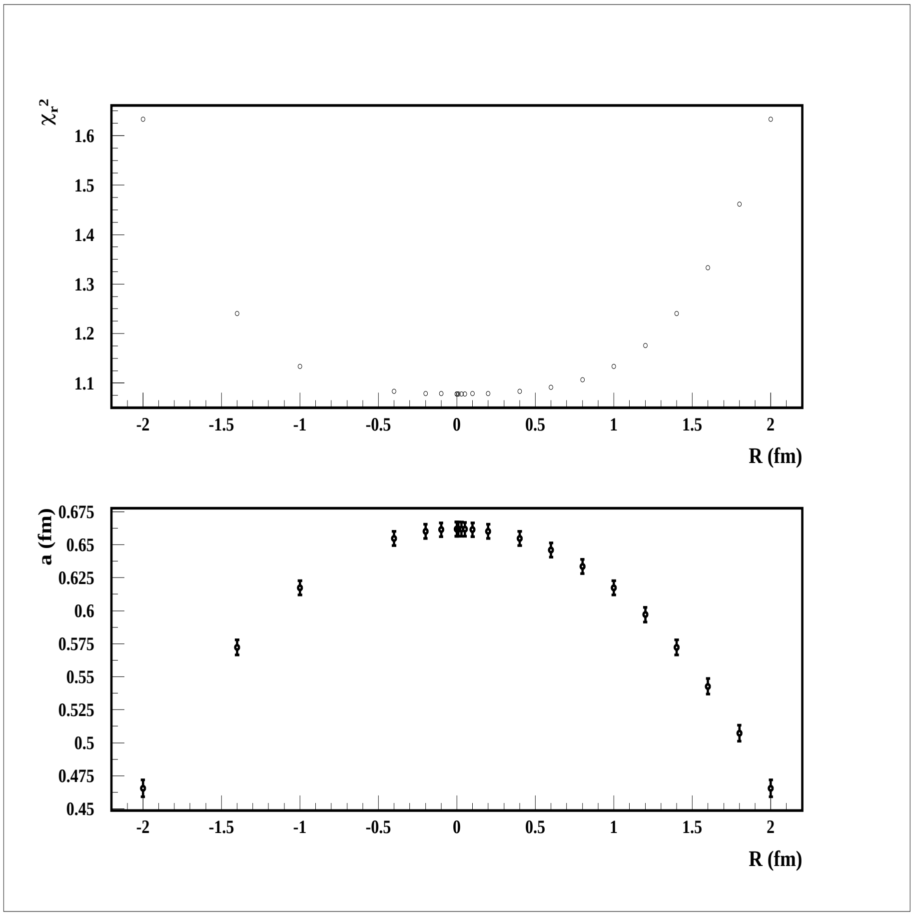

Figure 4.17: *Variation of the χ_r^2 (top) and the a parameter (bottom) versus the R parameter in fits using the SF parametrization and the experimental data limited to the low t range.*

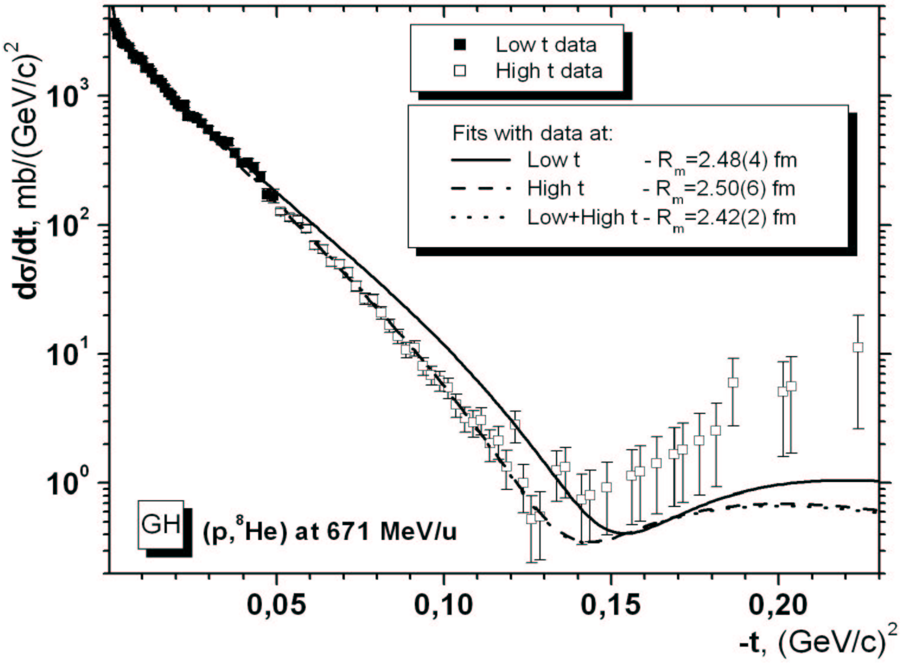

Figure 4.18: *Calculated differential cross sections versus the four-momentum transfer squared $-t$ from the GH parametrization of ^8He. The results use the data sets at low t, high t and the combined data set.*

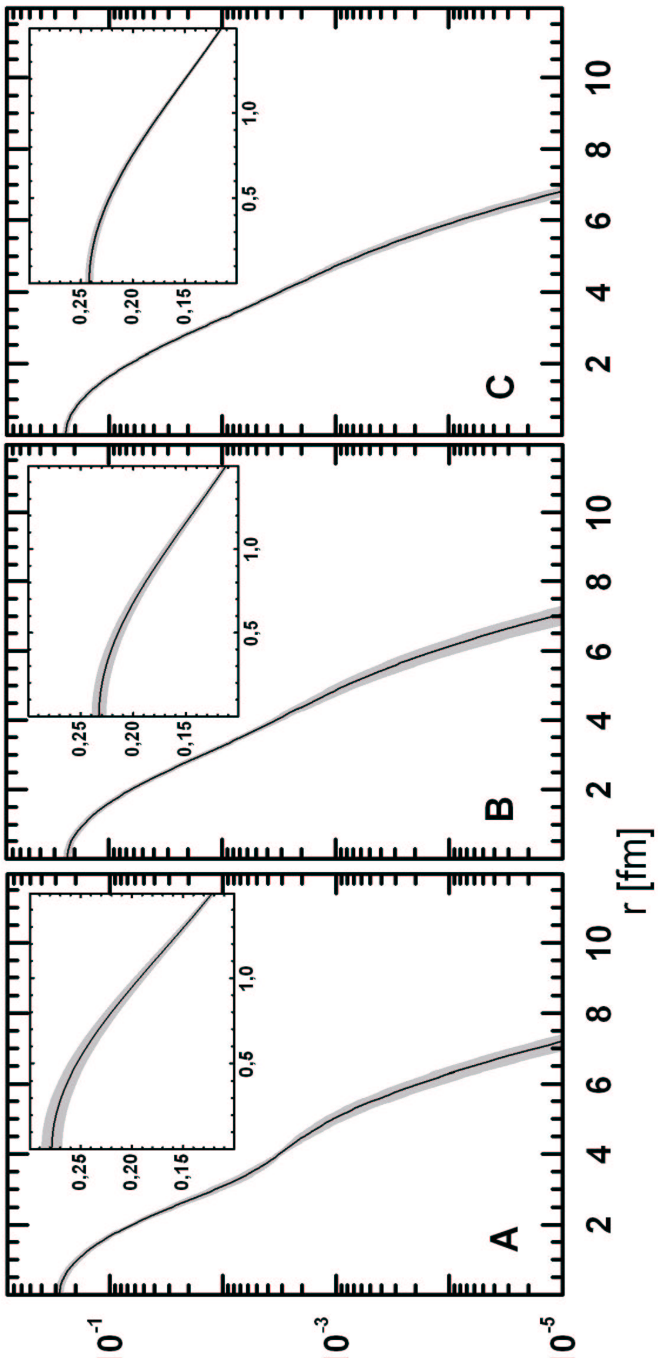

Figure 4.19: *Total nuclear matter density distributions of* ^{8}He *deduced with the GH fit parameters shown in table 4.10. Solid lines corresponding to results from fitting the low* t *data (A), the high* t *data (B) and the combined data (C) are shown together with the error corridor in light gray. Inserts give, in a linear scale, a more detailed view of the matter distribution around the center of the nucleus.*

4.5.2 Results for parametrizations which allow for a separate description of core and halo nucleons

The parameter values for the GG parametrization are shown in table 4.11. The relevant quantities shown are the matter radius $R_m \pm \sigma_m$, the core $R_c \pm \sigma_c$ and halo $R_h \pm \sigma_h$ radii as the two free descriptive parameters (Sec. 4.2.2.4 p.56) and the correlation parameter $\sigma_{c,h}$. If one includes the new data, a less pronounced halo structure is obtained according to the estimation of the ratio R_c/R_h. The fit qualities are rather good from the χ^2_r values and from the calculated cross sections shown in figure 4.20. The fits with the present and the combined data give the same description, in particular the calculated first minimum is compatible with the experimental result. They underestimate the data at $|t| \geq 0.15 (GeV/c)^2$ [7]. The density distribution plots are shown in figure 4.21 where now in addition, one displays the α-core density distributions. The gain in precision when extending the fitting data to the high t region is less pronounced as compared for ^6He.

Data	$R_m(fm)$	$R_c(fm)$	$R_h(fm)$	$\sigma_{c,h}$	A, $[A_L, A_H]$	χ^2_r
Low t	2.47 (4)	1.66 (7)	3.08 (9)	-0.875	0.97 (1)	1.03
Present	2.43 (3)	1.93 (1)	2.85 (6)	-0.503	0.98 (2)	0.94
Combined	2.40 (2)	1.93 (2)	2.79 (4)	-0.613	0.99 (1), 1.00 (2)	1.10

Table 4.11: ^8He *fit values for the GG parametrization. The results are shown separately for the low t and the present data in the two first rows and for the combined data set in the last row. The normalization factor A and its error is displayed for the two first cases while the two factors* $A_{L,H}$ *are shown for the last one (combined data set).*

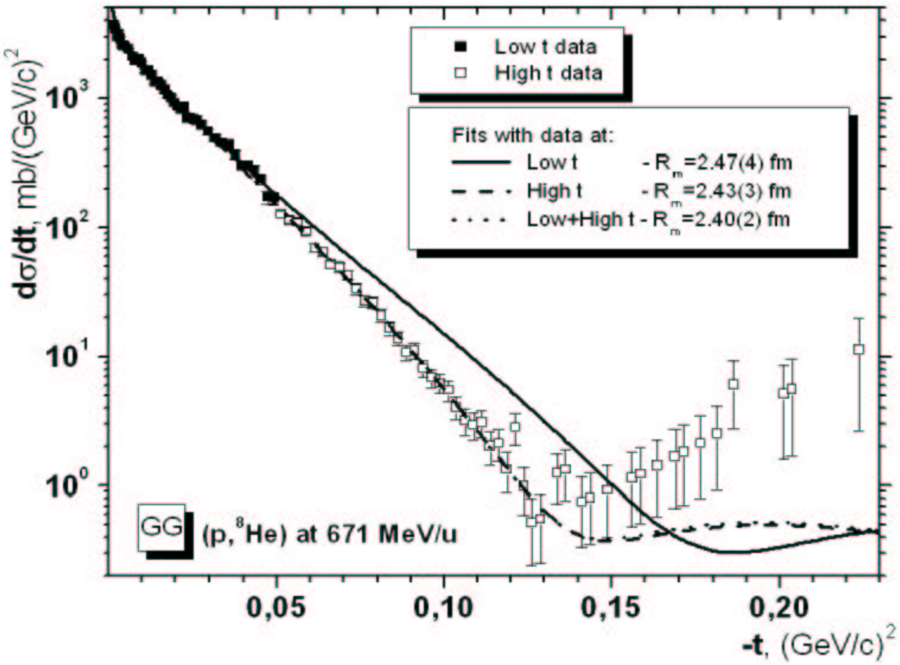

Figure 4.20: Calculated differential cross sections versus the four-momentum transfer squared $-t$ from the GG parametrization of ^8He. The results use the data sets at low t, high t and the combined data set.

---

[7] Actually this region, due to relatively high errors, has a little influence on the final results and as a proof, the same result was obtained after having skipped the data points in question.

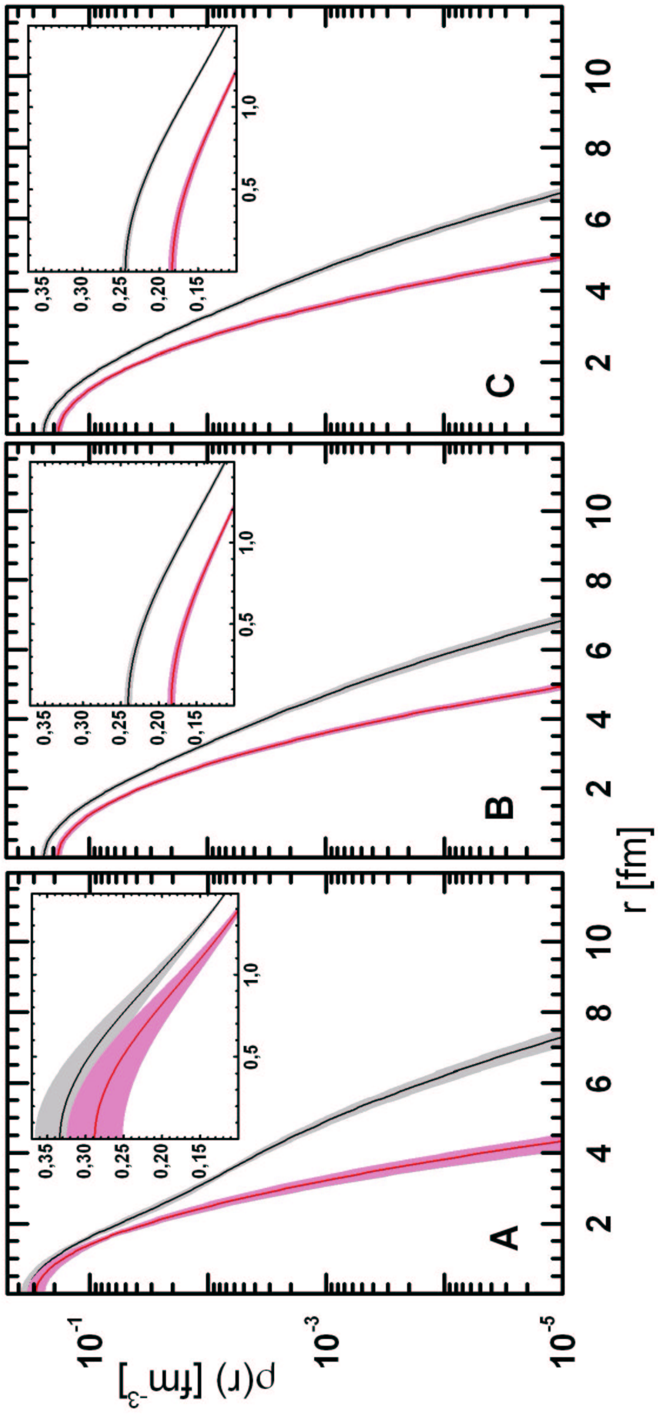

Figure 4.21: *Total (black) and core (red) nuclear matter density distributions of* ^{8}He *deduced with the GG fit parameters shown in table 4.11. Solid lines corresponding to results from fitting the low* t *data (A), the high* t *data (B) and the combined data (C) are shown together with the error corridor in light gray (total) and light pink (core). Inserts give, in a linear scale, a more detailed view of the matter distribution around the center of the nucleus. The total density distribution is normalized to the total number of nucleons while the core density is normalized to the number of core nucleons.*

The parameter values for the GO parametrization are shown in table 4.12. The relevant quantities shown are the same as in the GG parametrization. The corresponding calculated cross sections are shown in figure 4.22 where one notices that a very pronounced halo structure is obtained when only the data at low t are considered: this observation is confirmed by the matter density distributions plotted in figure 4.23 and by observing the variation of the ratio R_c/R_h from table 4.12.

Data	$R_m(fm)$	$R_c(fm)$	$R_h(fm)$	$\sigma_{c,h}$	A, $[A_L, A_H]$	χ_r^2
Low t	2.43 (3)	1.40 (7)	3.15 (7)	-0.841	0.97 (1)	1.04
Present	2.35 (2)	1.74 (1)	2.83 (4)	-0.170	0.98 (2)	0.98
Combined	2.35 (1)	1.73 (1)	2.83 (2)	-0.302	1.00 (1), 0.99 (2)	1.16

Table 4.12: ^8He *fit values for a GO parametrization. The results are shown separately for the low (S105) and high (S174) t range and for the combined data sets in the last row. The normalization factor A and its error are displayed for the two first cases (one experimental data set) while the two factors* $A_{H,L}$ *are shown for the last one (combined data set).*

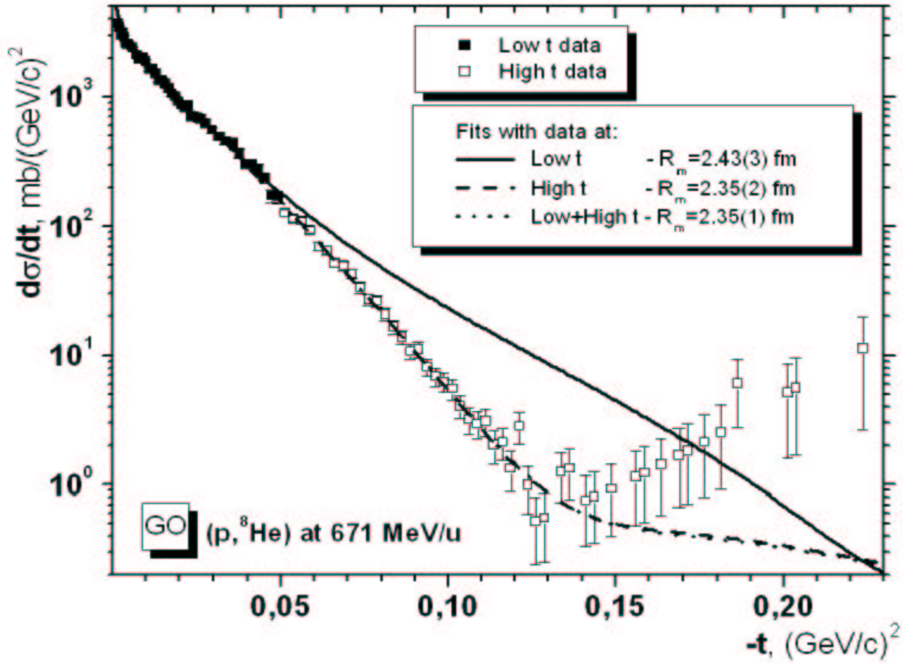

Figure 4.22: *Calculated differential cross sections versus the four-momentum transfer squared* $-t$ *from the GO parametrization of* ^8He*. The results use the data sets at low t, high t and the combined data set.*

4.5.3 Results discussion

As for ^6He, the table 4.13 summarizes the different results concerning the relevant radii, the normalization parameter(s) and the reduced chi-square. Compared to the ^6He case, the fit quality is worse. This fact is not fully understood now and can be attributed to the errors in the obtained data. The latter are still preliminary since large systematical errors arise from the background subtraction. This is a probable reason which will be investigated in the future.

The same remarks as for ^6He can be drawn here concerning the good absolute normalization of the experimental cross section. Yet one must recall that the fits made in the low t region are unable to describe

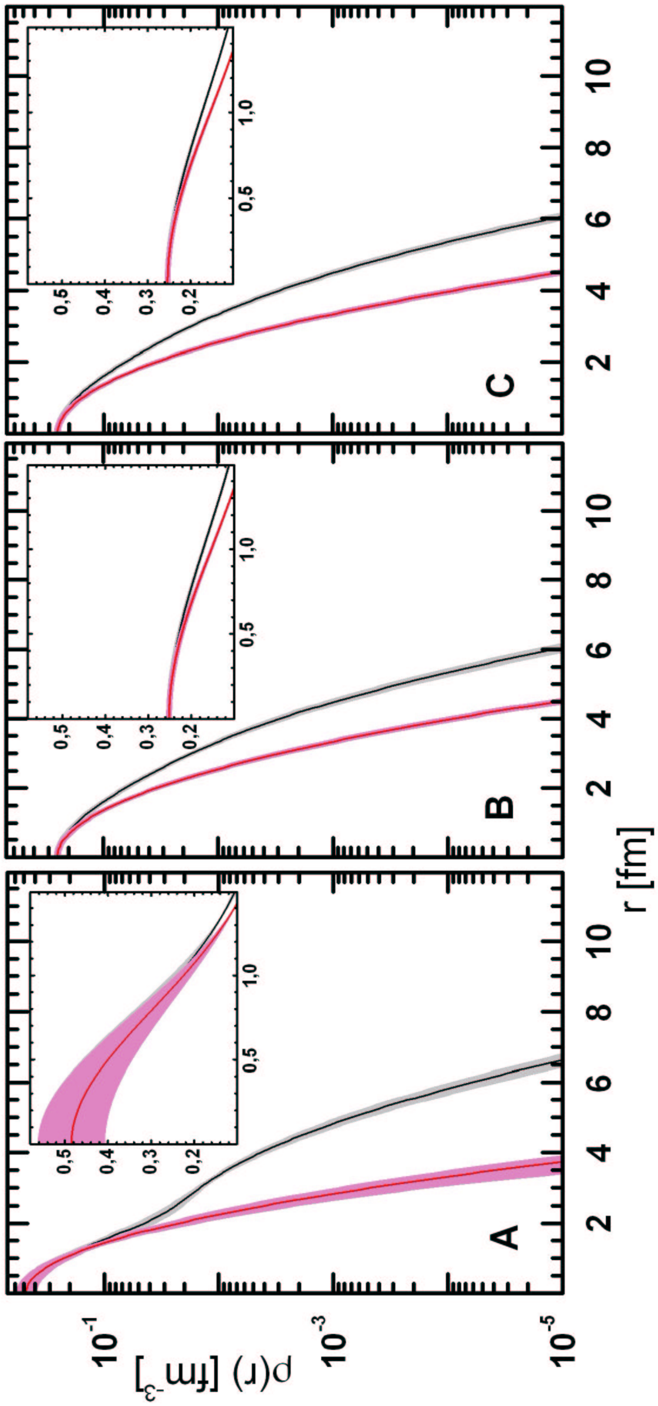

Figure 4.23: *Total (black) and core (red) nuclear matter density distributions of ^8He deduced with the GO fit parameters shown in table 4.12. Solid lines corresponding to results from fitting the low t data (A), the high t data (B) and the combined data (C) are shown together with the error corridor in light gray (total) and light pink (core). Inserts give, in a linear scale, a more detailed view of the matter distribution around the center of the nucleus. The total density distribution is normalized to the total number of nucleons while the core density is normalized to the number of core nucleons.*

the new data while this was not the case for ^6He. In addition, both fits performed with the data at high t and with the combined data underestimate systematically the measured elastic cross section for $t \geq 0.15(GeV/c)^2$. This deviation may be related to the correlation between nucleons which is, at present, taken into account in the Glauber calculation only in an approximate way. Their effects and especially the center-of-mass correlations (App. D p.113) are expected to be important in this region therefore, this can be a source of large systematical. An exact treatment of these correlations in the Glauber calculation will be included in the near future.

Model	R_m (fm)	R_c (fm)	R_h (fm)	$\frac{A_L}{A}$	A_H	χ_r^2
WS	2.44 (2) 2.49			0.98 (1) 0.96 (1)	1.00 (2)	1.09 1.02
SF	2.44 (2) 2.46			0.98 (1) 0.97 (1)	1.00 (2)	1.09 1.04
GH	2.42 (2) 2.48 (4)			0.98 (1) 0.96 (1)	1.00 (2)	1.10 1.01
GG	2.40 (2) 2.47 (4)	1.93 (2) 1.66 (7)	2.79 (4) 3.08 (9)	0.99 (1) 0.97 (1)	1.00 (2)	1.10 1.03
GO	2.35 (1) 2.43 (3)	1.73 (1) 1.40 (7)	2.83 (3) 3.15 (7)	1.00 (1) 0.97 (1)	0.99 (2)	1.16 1.04

Table 4.13: *Summary of the total, core and halo radii (R_m, R_c, R_h) values after fitting the experimental (p,^8He) elastic differential cross section at 671 MeV/u. For every model parametrization, the fit results from the combined data set (first line of each row) and from the low t data (second line) are presented. The normalization parameter(s) and the reduced chi-square are also reported. The errors shown do not contain the systematical uncertainty contribution coming from the Glauber calculation.*

A small increase of the precision on the radii is obtained when the present experimental data are included in the fit analysis. The obtained R_m values do not include any systematical uncertainty and still are relatively consistent. If one considers only the GG and the GO parametrizations, it is important to note that while the newly obtained R_h values are consistent withing the fit errors, the new R_c values are not. This fact, still not perfectly understood, might be related to the relative bad quality of the obtained fits where one clearly sees that the data are badly described. Another possible explanation can be drawn from the fact that the total experimental uncertainties are higher in the region of high t which is needed for a precise determination of R_c, thus inducing inconsistencies between the two parametrizations. This last reason does not concern the halo radius R_h which is sensitive to the cross section in the region of low transfered momentum.

From the comparison of the quantity R_c/R_h, one concludes that the relative contribution of halo matter decreased. This observation can also be made when looking to the mean values deduced from all models as shown in table 4.14.

Data		S105 [14]	Combined
$R_m(fm)$	(1) [82]	2.45 (4) (2) 2.45 (4) (1)	2.39 (2) (2)
$R_c(fm)$	 [82]	1.53 (7) (18) 1.55 (7) (18)	1.77 (2) (17)
$R_h(fm)$	 [82]	3.12 (8) (5) 3.09 (8) (6)	2.82 (4) (3)

Table 4.14: *Summary table showing the ^8He radii (total, core and halo) as determined from different model combinations. Every result R (ΔR) (σ_R) shows respectively the mean radius, its uncertainty(2) and the deviation as defined in Eqs. 4.21 and 4.22 p.69. In the third column, the results obtained from our analysis (first line of each row) of the low t data are compared to the original ones appearing in [82] (second line).*
(1) The collection GH+GG+GO was used for the low t data while the combination SF+GH+GG+GO was used in Ref. [82] (low t) and for the combined data.
(2) ΔR does not contain the systematical uncertainty contribution coming from the Glauber calculation.

The main observation here concerns the total size obtained after combining the two data sets which, being still consistent with the value published in Ref. [82], decreases slightly. For the final determination of the matter radius, the SF parametrization is taken into account. In conclusion, from the results obtained with the presented model parametrizations in Tab. 4.13, the deduced ^{8}He radii, including systematical errors due to the uncertainties of the Glauber model input parameters, are R_m=2.39(5) fm, R_c=1.77(18) fm and R_h=2.82(7) fm.

The nuclear matter density distributions are plotted in Fig. 4.24 together with the error corridor determined as the total contribution from all uncertainties. In the case where combined data are used for fitting, all parametrizations give a similar description of the nuclear matter in the region $r \leq 4\ fm$ except of the GO distribution which is systematically lower. The final uncertainty is, as expected, reduced for the case where combined data are used; a factor 3 is gained in the vicinity of the nucleus center.

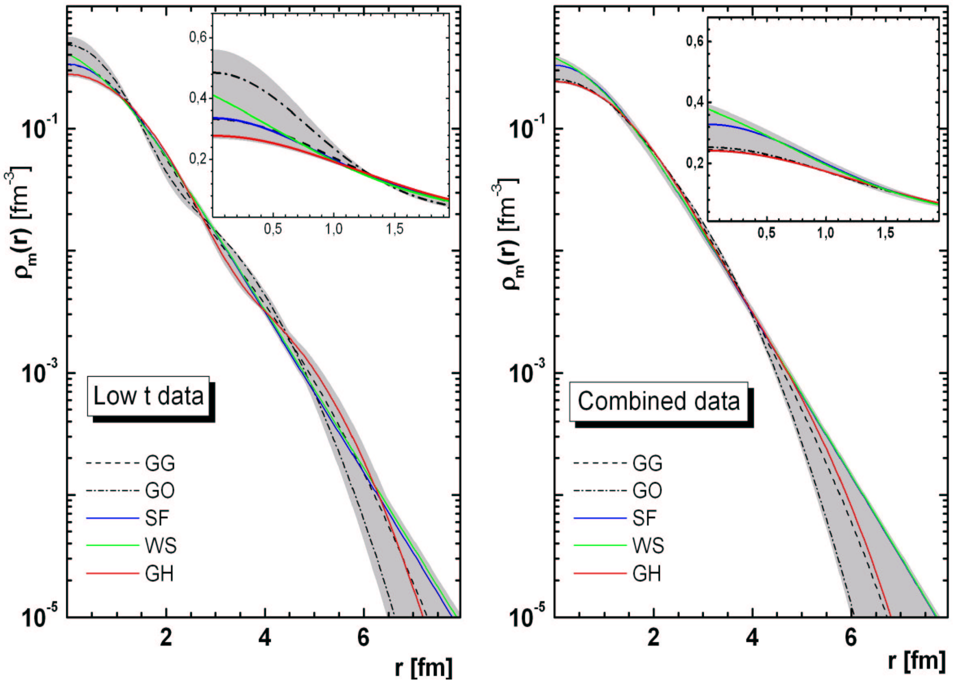

Figure 4.24: *Total nuclear matter density distributions of ^{8}He deduced from the model parametrizations WS, SF, GH, GG and GO. Results are shown from fits with the low t data (left part) and the combined data (right part). The error corridor (shaded area) is the envelope including the uncertainties from all parametrizations without systematical uncertainties in the parameters of the pN amplitudes used in the Glauber calculation. Inserts give, in a linear scale, a more detailed view of the density distribution around the center of the nucleus.*

It was already concluded [82] that the apparent size of the ^{8}He core is larger as compared to the free ^{4}He (1.49 fm), due to the center of mass motion effect despite the fact that the obtained value $R_c = 1.55(15)$ fm still bears some uncertainty. With the new value $R_c = 1.77(18)\ fm$ and despite the large error, this observation can be definitely confirmed in the case of ^{8}He. This effect is clearly visible if one looks to the mean distribution of the core matter density (Fig. 4.25) in the two cases: low t and combined data.

By combining the results obtained from the two nuclei, one can see the effect of stronger correlations from the four valence neutrons of ^{8}He against two only for ^{6}He by comparing their effective core radii $R_m(^{4}He) \leq R_c(^{8}He) \leq R_c(^{6}He)$. It affects the core motion by reducing its amplitude and as a result, the core size is smaller in ^{8}He.

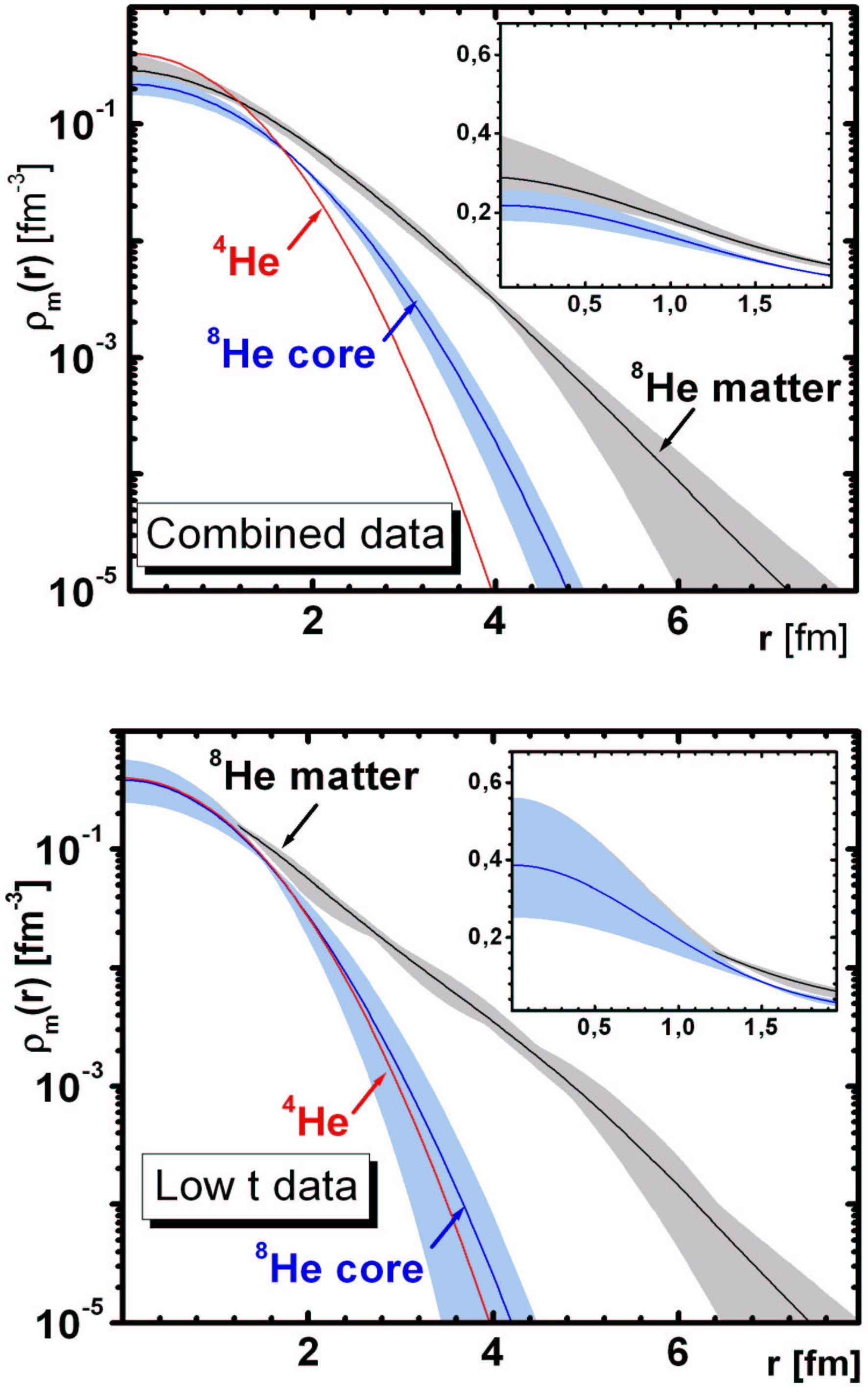

Figure 4.25: *The average total (black) and core (blue) matter density distributions of* ^{8}He *as results from fits with the low* t *data (bottom figure) and the combined data (top figure). The error corridor (shaded area) is the envelope including the uncertainties from all the cited parametrizations and is identical to the one shown in Fig. 4.24 for the case of the total nuclear matter. These distributions are compared to the case of free* ^{4}He *shown in red.*

4.6 Test of theoretical model calculations by the present data

The present data permit, in addition, to examine the matter density distributions predicted by available microscopic theoretical calculations. These density distributions are used as an input for Glauber calculations. The obtained "theoretical" differential elastic cross sections are compared to the experimental data thus providing a test of the model predictions and of the NN (nucleon-nucleon) force types used in those models. The results from three models are presented in the following sections.

Before doing that, it would be interesting to compare the obtained cross sections with the extreme cases of a hard core described in the COSMA model [59] and a completely dissolved core. This is shown in figure 4.26. The $(p,^6He)$ data lie in between which means that a precise theoretical description of the ^6He nucleus should lead to an intermediate structure. The $(p,^8He)$ is less straightforward and any discussion should be preceded by an additional detailed study.

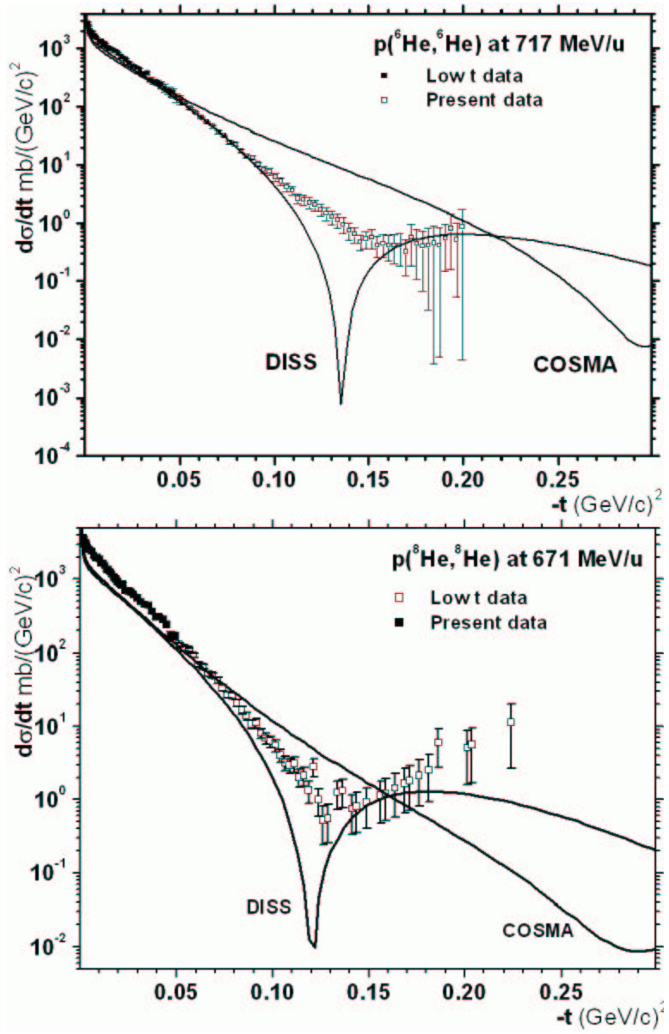

Figure 4.26: *Comparison of the experimental differential cross sections of the elastic $(p,^6He)$ (top) and $(p,^8He)$ (bottom) scattering to the calculated ones using the two extreme descriptions seen in the introduction (COSMA and DISS)*

4.6.1 Few-body calculations

The ^6He nucleus is treated as a three-body (α+n+n) system [19], the main approximation being to neglect explicit consideration of the internal degrees of freedom of the four-nucleon core. These are treated approximately in the model through the use of phenomenological N-core effective interactions. The total wave function is then the sum of the three Faddeev components $\Phi = \Phi_{12} + \Phi_{c1} + \Phi_{c2}$ where each component is labeled by the interacting particle pair, c being the core and $1, 2$ being the valence neutrons. A representative selection of the Faddeev ground state wave function models and the corresponding density distributions were calculated [84] following the methods described in [19]. According to different calculations of the corresponding $(p,^6He)$ cross sections at low t [82, 84] it was concluded that the FC model is the best description for the ^6He nucleus.

The calculated cross sections were all extended to high transfered momentum in order to be compared with the present data as shown in figure 4.27. As seen, the agreement is fairly well while the first minimum is well reproduced despite the relative discrepancy in the corresponding radii. One should notice that in order to reproduce the experimental data on reaction cross section, the authors of Ref. [84] needed an increased halo radius for ^6He, suggesting 2.71 ± 0.04 fm while they proposed 2.50 fm [83] in order to describe the data on proton elastic scattering at low t.

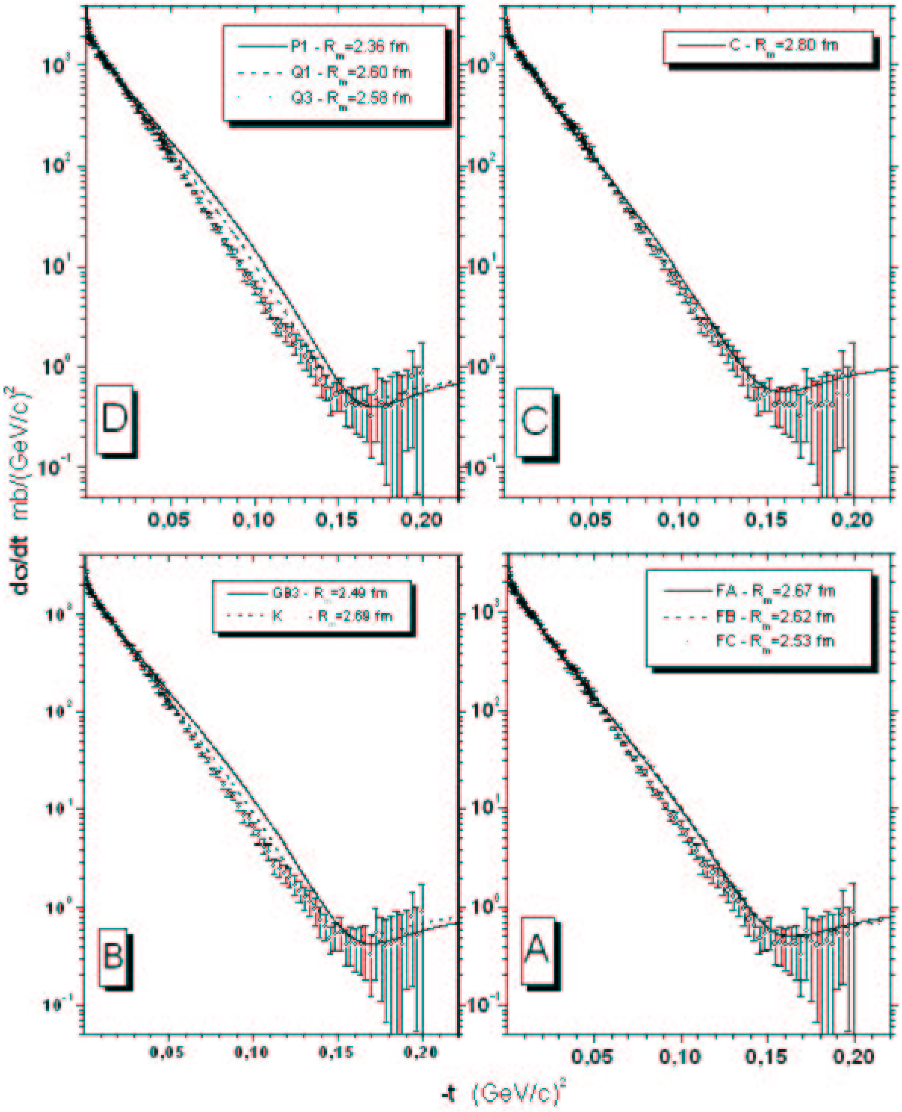

Figure 4.27: $p(^6He,^6He)$ *calculated differential cross sections at 717 MeV/u using the Glauber method with, as an input, matter density distributions calculated with the few-body model assuming different nuclear forces. The force types and the corresponding radii shown here are commented in table II of Ref. [84]. The data at low t (open squares) and at high t (black squares) are displayed for comparison.*

4.6.2 Boson dynamic correlation model

The ground state density distribution of ^6He is determined within the boson dynamic correlation model (BDCM) which describes the ground states of light nuclei in terms of microscopic correlated clusters [85, 86]. The valence neutrons interact via the neutron-neutron interaction without exciting the closed-shell reference nucleus which remains in its ground state. The interaction between the valence and the core particle is taken into account through the possible excited states of the core. The main driving idea is that the deformation of the nuclear core might reshape at high momenta the tail of the nuclear matter distribution.

The calculated cross sections are compared to the experimental ones in the left part of Fig. 4.28. The corresponding calculated matter distributions used here are shown in the right part of Fig. 4.28. They have typical oscillations due to the basic assumptions used in this model. Three assumptions were used leading to an increasing total matter radius [86]:

1. only the term L=0 in the interaction of the system (valence neutrons, excited core) yielding $R_m = 2.36$ fm (solid curve)
2. all the permitted components L=0,1,2,3,4 are considered giving $R_m = 2.41$ fm (dashed curve)
3. the core excitation was altered in order to allow for larger spin-orbit terms to be included. The result is a much increased matter radius $R_m = 2.60$ fm (dash-dotted curve)

While these densities reproduce well the data at low momentum transfer, for the whole scattering range, the best agreement is obtained for the last case showing the importance of including such core excitations and summing over a large number of interacting terms. In particular, the first diffraction minimum is reproduced only when including larger spin-orbit terms. The assumptions 1 and 2 yield the same differential cross section in the considered range.

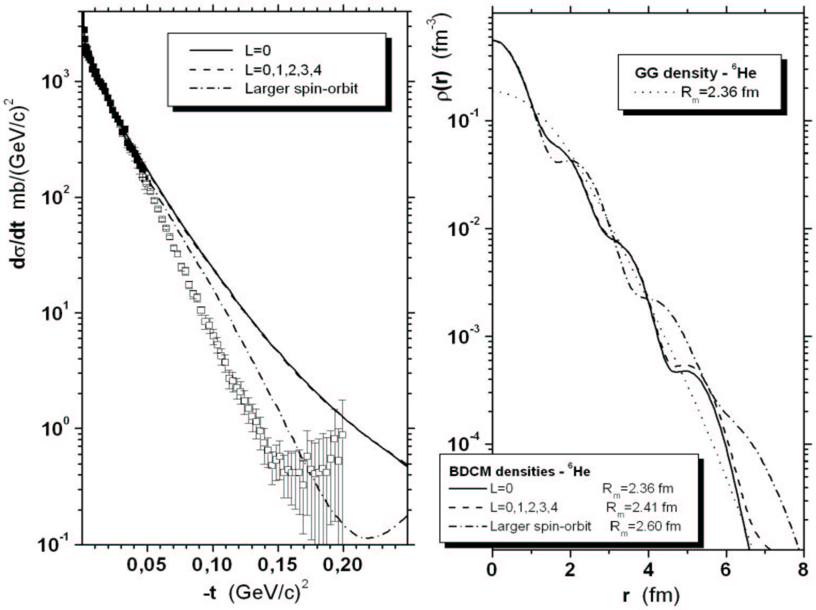

Figure 4.28: $p(^6He,^6He)$ *calculated differential cross sections at 717 MeV/u using the Glauber method in the whole data range (left) using the matter densities (right) calculated with the BDCM model under different assumptions (see text). The complex structure of these densities is compared to a GG density distribution. The data at low t (open squares) and at high t (black squares) are displayed for comparison.*

4.6.3 Refined resonating group method

The matter density distributions are calculated in the frame of the RRGM theory [87] using an effective nucleon-nucleon force introduced by Csoto (CS). The Csoto and Csoto2 correspond respectively to a one and a double gaussian parametrization of the α-core. Another NN force type from Stoewe and Zahn [88, 89, 90, 91] was also used with several variants abbreviated as follows:

- SZ and SZ2: omits the central force terms in the odd parity singlet and triplet states of the NN two-body force. The α-core wave function is parametrized with a single and double gaussian respectively.
- SZV2 and SZV22: includes all terms. The α-core wave function is parametrized with a single and double gaussian respectively. The repulsive force of these terms increases the phase space which leads to a somewhat larger matter radius.

The calculated cross sections compared to the measured ones are shown in Figs. 4.29 and 4.30 for ^6He and ^8He respectively. They deviate much more as compared to the two previous models. They succeed to describe the data at very small t and to a minor degree, at the first diffraction minimum.

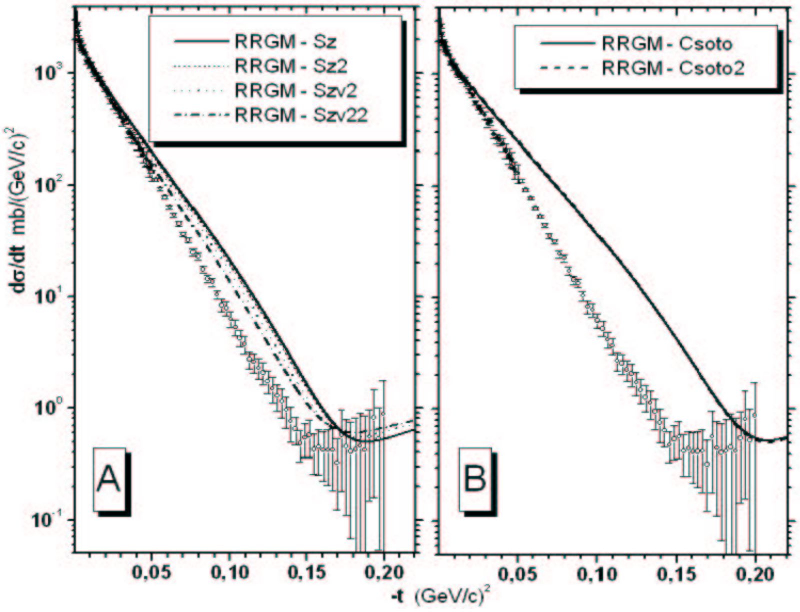

Figure 4.29: *Comparison of the experimental data with the calculated differential cross sections for* $p(^6He,^6He)$ *at 717 MeV/u using microscopic matter density distributions from the RRGM with various NN forces (see text for details)*

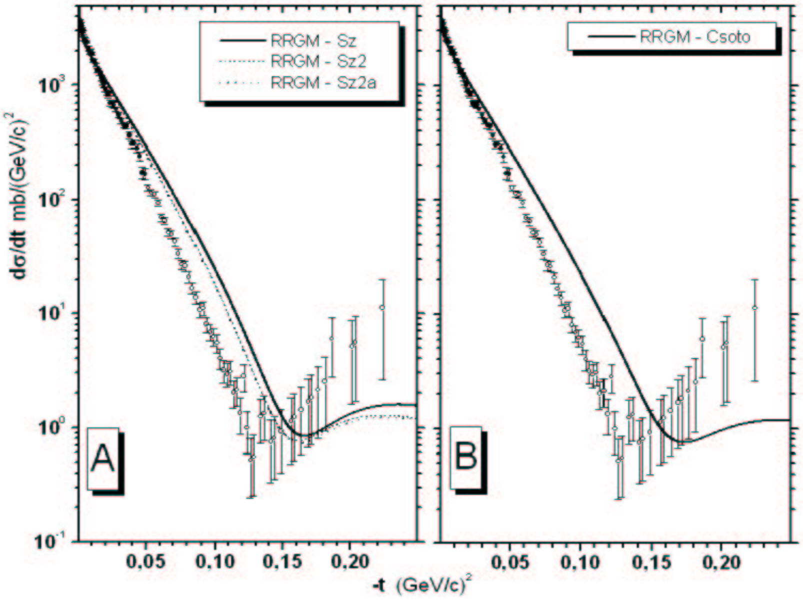

Figure 4.30: *Comparison of the experimental data with the calculated differential cross sections for* $p(^8He,^8He)$ *at 671 MeV/u using microscopic matter density distributions from the RRGM with various NN forces (see text for details)*

Chapter 5

CONCLUSION AND PERSPECTIVES

Many previous experimental results proved that the $^{6,8}He$ nuclei show a clear signature of neutron halos. In particular the study of nuclear matter density distributions using intermediate energy proton elastic scattering at low transfered momentum $0.002 \leq |t| \leq 0.05 (GeV/c)^2$ [82, 14] was sensitive to the outer structure of these nuclei. In the work presented here, a deeper study of the inner part of these two nuclei was conducted in order to get a better perception on their structure. For this purpose, measurements were extended to the higher transfered momentum region $0.05 \leq |t| \leq 0.22 (GeV/c)^2$, typically to the first diffraction minimum by using exactly the same kinematical conditions. For the first time, a liquid-hydrogen target was successfully used in a reaction experiment with radioactive beams allowing measurements with a low background level. The new differential elastic cross sections obtained in this work agree well with the ones measured in the low t domain as seen from the region where both data overlap.

Cross sections were calculated within the assumption of Glauber multiple scattering theory and fitted to the data in order to get the best possible description. Different parametrizations to model the nuclear matter density distributions were used. The available experimental data at low and high t were analysed separately and together, in order to determine the influence of the measurement domain on the final density distribution. The individual matter rms radii determined with the present data are, in general, consistent with the ones determined from the data at low transfered momentum. For a given data set, the different parametrizations are compatible within errors if systematical uncertainties from the Glauber calculation are included, which proves that the procedure used here is practically model independent. Therefore, the final radii were taken as the weighted arithmetic mean of the individual values obtained from each model:

Nucleus	R_m(fm)	R_c(fm)	R_h(fm)
^6He	2.36 (6)	1.97 (9)	2.97 (8)
^8He	2.39 (5)	1.77 (18)	2.82 (7)

The size of^6He undergoes an increase of 0.06 fm while for ^8He it decreases by the same quantity as compared to the results from the low t data analysis in [82] which yielded respectively 2.30(7) fm and 2.45(7) fm for the nuclear matter radii. These two last values are still consistent with the ones determined in the present work. The small error bars can be related indirectly to the better knowledge of the overall matter density distributions after having performed a combined analyzes of the data at low and high t. These values have to be considered with the contribution of the so-called "nuclear tail" discussed in Ref. [83, 82] since intermediate energy protons are not sensitive to the nuclear medium in this region.

The present data enable one to get a new set of density distributions with a high precision level which might certainly be used as input for other experimental and theoretical studies (inelastic scattering, transition amplitudes, etc ...). As this was the main goal of the present work, the core radii were re-evaluated to $R_c(^6He) = 1.97(9)\ fm$ and $R_c(^8He) = 1.77(18)\ fm$ which can be compared to the previous values from [82]: $R_c(^6He) = 1.88(12)\ fm$ and $R_c(^8He) = 1.55(15)\ fm$. This use of these data will certainly make the present theoretical models of halo structure more stringently tested.

The effective core size R_c of both nuclei is bigger than the free ^4He size which is $R_m = 1.49\ fm$: this feature was already reported (Ref. [82]) in the case of ^6He and is confirmed by the new measurement. In the case of ^8He, this observation is possible only if the present data are taken into account. It is interpreted as the result of the relative motion of an α particle with an intrinsic size close to 1.49 fm around the core-halo center-of-mass (CM). The effect of the relative motion on the core size by increasing the number of the valence neutrons already predicted [92], can also be compared between ^6He and ^8He nuclei: adding more valence neutrons to the α core prevent it to extend more spatially which can be seen in the newly determined values $R_{c,^8He} \leq R_{c,^6He}$.

In addition, the data were compared to some theoretical microscopic approaches available in the existing literature since it is well known that the elastic scattering angular distribution is an excellent tool to validate calculated quantities such as the matter distribution and the total nuclear radius. The few-body calculations [84, 19] show a relatively good agreement. In general, all the calculations succeed to describe the first diffraction minimum within the experimental errors but show more or less a systematic deviation $((d\sigma/dt)_{calc} \geq (d\sigma/dt)_{exp})$ in the region before the first minimum. By examining the different model expectations on the location of the first minimum, it appears also of interest to extend those measurements to the region of the second diffraction maximum.

The experiment described here was also propeled by the idea to analyze the inelastic and break-up channels by measuring in coincidence the charged fragment and the recoil nucleus. In experiments using high energetic radioactive beams, this measurement was original and there is hope, once the full data analysis is completed, to get further information on the structure of $^{6,8}He$ nuclei.

A test measurement using the nearby stable isotope ^4He was originally planned but unfortunately, due to limited beam time, was not conducted in good conditions. Such data would provide an additional check of the present experimental procedure and data analysis method. ^4He is an important testing case for the validity of the present Glauber calculations in the region $t \geq 0.2\ (GeV/c)^2$. The basic assumptions of the model (Appendix D p.113) are valid only for $t \simeq 0$ and therefore, one must include several correlation effects which are expected to be non negligible in the region of the present measurement. For this reason, a measurement and an analysis of proton elastic scattering at $\sim 700\ MeV/u$ on ^4He in the same domain is urgently needed. In addition to that, several other halo candidates are foreseen to be included in a future study, in particular the Li isotopes for which the data at low t are available and can be confronted to an extended measurement as was shown here. In such measurement, one must in particular separate the different channels where Li reaches its particle-excited states which is certainly a delicate task at intermediate energies.

Bibliography

[1] E. Rutherford, Proc. Manchester Liter. and Philos. Society IV **55**, 18 (1911).

[2] E. Rutherford, Phil. Mag. (6) **21**, 669 (1911).

[3] E. Rutherford, Phil. Mag. **37**, 581 (1919).

[4] C. J. Batty *et al.*, Advances in Nuclear Physics **19**, 1 (1989).

[5] J. L. Friedes *et al.*, Nucl. Phys. A **104**, 294 (1967).

[6] G. Alkhazov, S. Belostotsky, and A. Vorobyov, Phys. Rep. **42**, 89 (1978).

[7] S. J. Wallace, Advances in Nuclear Physics **12**, 135 (1981).

[8] P. G. Hansen, A. S. Jensen, and B. Jonsson, Annu. Rev. Nucl. Part. Sci. **45**, 591 (1995).

[9] N. A. Orr, Exotic nuclei - Haloes, in *Ecole Internationale Joliot-Curie 1997, 8-13 Septembre 1997*, Maubuisson, France, 1997, IN2P3, CNRS.

[10] K. Riisager, Rev. Mod. Phys. **66**, 1105 (1994).

[11] I. Tanihata, J. Phys. G.: Nucl. Part. Phys. **22**, 157 (1996).

[12] I. Tanihata *et al.*, Phys. Rev. Lett. **55**, 2676 (1985).

[13] I. Tanihata *et al.*, Phys. Lett. B **160**, 380 (1985).

[14] S. R. Neumaier *et al.*, Nucl. Phys. A **712**, 247 (2002).

[15] P. Egelhof, Prog. Part. Nucl. Phys. **46**, 307 (2001).

[16] I. Tanihata *et al.*, Phys. Lett. B **206**, 592 (1988).

[17] G. Audi and A. H. Wapstra, Nucl. Phys. A **565**, 66 (1993).

[18] G. F. Bertsch and H. Esbensen, Annals of Physics **209**, 327 (1991).

[19] M. V. Zhukov *et al.*, Phys. Rep. **231**, 151 (1993).

[20] R. N. Boyd and I. Tanihata, Physics Today **45**, 44 (1992).

[21] A. C. Mueller and B. M. Sherrill, Annu. Rev. Nucl. Part. Sci. **43**, 529 (1993).

[22] J. M. D. Auria, Studies with exotic nuclei at TISOL and ISAC-1, in *Proc. Int. Conf. on Exotic Nuclei and Atomic Masses, ENAM 95, June 19-23, 1995*, p. 821, Arles, France, 1995, Editions Frontières.

[23] K. Riisager *et al.*, Phys. Lett. B **235**, 30 (1990).

[24] M. J. G. Borge *et al.*, Z. Phys. A **340**, 255 (1991).

[25] M. J. G. Borge *et al.*, Nucl. Phys. A **560**, 664 (1993).

[26] L. V. Grigorenko *et al.*, Phys. Rev. C **57**, R2099 (1998).

[27] A. S. Formicher *et al.*, Z. Phys. A **351**, 129 (1995).

[28] J. J. Kolata *et al.*, Phys. Rev. Lett. **81**, 4580 (1998).

[29] Y. E. Penionzkevich, Investigation of very neutron-rich isotopes of the lightest elements, in *Proc. Int. Conf. on Exotic Nuclei and Atomic Masses, ENAM 95, June 19-23, 1995*, p. 269, Arles, France, 1995, Editions Frontières.

[30] M. Trotta *et al.*, Phys. Rev. Lett. **84**, 2342 (2000).

[31] G. M. Ter-Akopian *et al.*, Phys. Lett. B **426**, 251 (1998).

[32] R. Raabe *et al.*, Phys. Lett. B **458**, 1 (1999).

[33] R. Raabe *et al.*, Study of low-energy reactions with a post-accelerated radioactive ^{6}He ion beam, in *Proc. 3rd Int. Conf. on Exotic Nuclei and Atomic Masses, ENAM 2001, 2-7 july 2001*, Hämeenlinna, Finland, 2001.

[34] A. A. Korsheninnikov *et al.*, Experimental studies of light exotic nuclei, in *Proc. Int. Conf. on Exotic Nuclei and Atomic Masses, ENAM 95, June 19-23, 1995*, p. 207, Arles, France, 1995, Editions Frontières.

[35] S. V. Stepantsov *et al.*, Elastic scattering and neutron transfer reactions at interaction of 26 AMeV ^{8}He beam with protons, in *Proc. 3rd Int. Conf. on Exotic Nuclei and Atomic Masses, ENAM 2001, 2-7 july 2001*, Hämeenlinna, Finland, 2001.

[36] M. D. Cortina-Gil *et al.*, Elastic scattering and charge exchange reaction studies with ^{6}He, ^{10,11}Be, in *Proc. Int. Conf. on Exotic Nuclei and Atomic Masses, ENAM 95, June 19-23, 1995*, p. 275, Arles, France, 1995, Editions Frontières.

[37] A. A. Korsheninnikov *et al.*, Nucl. Phys. A **384**, 97 (1994).

[38] Y. Perier *et al.*, Phys. Lett. B **459**, 55 (1999).

[39] D. Aleksandrov *et al.*, Nucl. Phys. A **633**, 234 (1998).

[40] D. Aleksandrov *et al.*, Nucl. Phys. A **669**, 51 (2000).

[41] T. Aumann *et al.*, Nucl. Phys. A **640**, 24 (1998).

[42] T. Aumann *et al.*, Phys. Rev. C **59**, 1152 (1999).

[43] L. V. Chulkov, What can we learn from the fragmentation of halo nuclei ?, in *Exotic Nuclei 2001, 24-28 july 2001*, Baikal, Russia, 2001.

[44] H. Emling, J. Phys. G.: Nucl. Part. Phys. **24**, 1561 (1998).

[45] K. Markenroth *et al.*, Nucl. Phys. A **679**, 462 (2001).

[46] M. Meister *et al.*, Nucl. Phys. A **700**, 3 (2002).

[47] K. Suemmerer and D. J. Morrissey, in *Proceedings of the First International Conference, October 1989*, p. 122, Berkeley, CA, USA, 1989.

[48] S. J. Wallace and S. E. Woosley, Astrophys. J. Suppl. **45**, 389 (1981).

[49] T. Kobayashi *et al.*, Nucl. Phys. A **538**, 343c (1992).

[50] S. A. Goncharev *et al.*, RIKEN-AF-NP-163 (1993).

[51] A. A. Korsheninnikov *et al.*, Nucl. Phys. A **617**, 45 (1997).

[52] Y. E. Penionzkevich *et al.*, Elastic scattering of neutron and proton halo nuclei, in *Proc. Int. Conf. on Exotic Nuclei and Atomic Masses, ENAM 95, June 19-23, 1995*, p. 323, Arles, France, 1995, Editions Frontières.

[53] N. K. Skobelev *et al.*, Z. Phys. A **341**, 315 (1992).

[54] R. J. Smith *et al.*, Phys. Rev. C **43**, 761 (1991).

[55] G. Alkhazov *et al.*, Phys. Rev. Lett. **78**, 2313 (1997).

[56] A. V. Dobrovolsky *et al.*, Study of halo structure in radioactive He and Li nuclei with proton elastic scattering, in *Proc. Int. Conf. Nuclear Physics at Border Lines, 21-24. May. 2001*, pp. 224–233, Lipari (Messina), Italy, 2002, World Scientific, Singapore.

[57] O. G. Grebenjuk *et al.*, Nucl. Phys. A **500**, 637 (1989).

[58] L. V. Chulkov, C. A. Bertulani, and A. A. Korsheninnikov, Nucl. Phys. A **587**, 291 (1995).

[59] M. V. Zhukov *et al.*, Phys. Rev. C **50**, R1 (1994).

[60] C. Bertulani and H. Sagawa, Nucl. Instrum. Methods A **588**, 667 (1995).

[61] A. G. Sitenko, *Theory Of Nuclear Reactions* (World Scientific, 1990).

[62] H. Geissel *et al.*, Nucl. Instr. and Meth. B **70**, 286 (1992).

[63] T. Schwab, GSI-91-10 preprint (1991).

[64] P. Egelhof, Pramana Journal Of Physics **53**, 365 (1999).

[65] K. Suemmerer *et al.*, Phys. Rev. C **42**, 2546 (1990).

[66] K. Suemmerer and B. Blank, Phys. Rev. C **61**, 034607 (2000).

[67] GASSIPLEX-PCB manual, *http://star.physics.yale.edu/star-rich/gassiplex.html*.

[68] Y. T. Borzunov *et al.*, PTE **3**, 542 (1984).

[69] P. Chesny *et al.*, CEA internal document (2000).

[70] Storage and Use of Flammable Gases for Experiments at Jefferson Lab, *http://www.jlab.org/ehs/manual/EHSbook-364.html*.

[71] BC-408, premium plastic scintillator, *http://www.bicron.com/bc408.htm*.

[72] E. Berdermann *et al.*, GSI 88-08 Report ISSN 0171-4546 (1988).

[73] W. R. Leo, *Techniques for nuclear and particle physics experiments* (Springer-Verlag, 1987).

[74] M. P. Malkov, *Handbook for physical and technical basics of cryogenics* (Energoatomizdat, 1985).

[75] Simulation of gaseous detectors, *http://consult.cern.ch/writeups/garfield/*.

[76] R. Serber *et al.*, Phys. Rev. **72**, 1008 (1947).

[77] R. J. Glauber*Lectures in theoretical physics - High-energy collision theory* Vol. I (W. E. Brittin, Interscience, New York, 1959).

[78] R. S. Mackintosh, Rep. Prog. Phys. **40**, 731 (1977).

[79] E. Arnold *et al.*, Phys. Lett. B **281**, 16 (1992).

[80] Y. N. Eldyshev *et al.*, Yad. Fiz. **16**, 506 (1972).

[81] Y. N. Eldyshev *et al.*, Sov. J. Nucl. Phys. **16**, 282 (1973).

[82] G. Alkhazov *et al.*, Nucl. Phys. A **712**, 269 (2002).

[83] J. S. Al-Khalili *et al.*, Phys. Rev. C **57**, 1846 (1998).

[84] J. S. Al-Khalili *et al.*, Phys. Rev. C **54**, 1843 (1996).

[85] M. Tomaselli *et al.*, Phys. Rev. C **62** (2000).

[86] M. Tomaselli *et al.*, Phys. Rev. C (2002).

[87] H. M. Hoffmann, **273**, 243 (1987).

[88] J. Wurzer, *Mikroskopische Beschreibung von Halokernen*, PhD thesis, Diplomarbeit, University of Erlangen, 1994.

[89] J. Wurzer and H. M. Hoffmann, Phys. Rev. C **55**, 688 (1997).

[90] J. Wurzer, *Untersuchungen zu den Neutron Halo Kernen unter den Helium und Lithium Isotopen*, PhD thesis, University of Erlangen, 1997.

[91] T. Mertelmeier and H. M. Hoffmann, Nucl. Phys. A **459**, 387 (1986).

[92] G. P. Kamuntaviõius, Phys. Rev. C **56**, 191 (1997).

[93] J. S. Gordon and E. Mathieson, Nucl. Instr. and Meth. **227**, 267 (1984).

[94] E. Gatti *et al.*, Nucl. Instr. and Meth. **163**, 83 (1979).

[95] G. Velichko, CERN, CMS note 2000/022 (2000).

[96] R. J. Glauber, Theory of high energy hadron-nucleus collisions, in *Proceedings of the 3rd International Conference on high energy physics and nuclear structure*, New York, USA, 1970.

[97] J. Saudinos *et al.*, Annual Review of Nuclear Science **24**, 341 (1974).

[98] A. G. Sitenko, Vestnik Acad. Nauk Ukr. SSR **12**, 9 (1971).

[99] A. G. Sitenko, Fiz. Elem. Chastits At. Yadra **4**, 546 (1973).

[100] A. G. Sitenko, Fortschr. Phys. **22**, 453 (1974).

[101] R. J. Glauber, Usp. Fiz. Nauk **103**, 641 (1971).

[102] C. J. Joachain and C. Quigg, Rev. Mod. Phys. **46**, 279 (1974).

[103] G. Alkhazov, PNPI preprint 2302 (1999).

[104] Y. Ogawa *et al.*, Phys. Lett. B **543**, 722 (1992).

[105] J. A. McNeil *et al.*, Phys. Rev. C **27**, 2123 (1983).

[106] S. R. Neumaier, *Untersuchung der nuklearen Dichverteilungen der neutronenreichen Kerne ^{6}He und ^{8}He mittels elastischer Protonsstreuung in inverser Kinematik bei Energien um 700 MeV/u*, PhD thesis, Fachbereich Physik, TH Darmstadt, 1995.

[107] H. Lesniak and L. Lesniak, Nucl. Phys. B **38**, 221 (1972).

Appendix A

Coordinate determination

The complete formalism concerning the determination of the chamber local coordinates can be found in references [93, 94]. A first step consists of searching the strip with the maximum charge Q_2 . The immediate neighboring strips are analyzed, then the next ones. The corresponding charges are then Q_0 , Q_1 , Q_3 , and Q_4 as shown schematically in Fig. A.1. The corresponding coordinates of strip centers are then X_0 , X_1 , X_2 , X_3 , and X_4 (respectively Y_0 , Y_1 , Y_2 , Y_3 , and Y_4) in the case of an X plane (resp. a Y plane). This set of five charges or less defines one cluster. Experience shows that adding more charges from the other neighbors neither changes the position value nor increases the precision. Particularly, one observed during the test runs that in the case of clusters with an odd number of fired strips, there was no difference if 3 or 5 strips were used in the calculation algorithm.

For the same event, the same process searches then for other possible clusters. In the case of ^6He run, one observed 80 % of single cluster events, as compared to 19 % of double cluster events. Events with 3, 4 and 5 clusters amounted for less than 1 %. No higher number of clusters per event was observed. All the clusters which appeared in all the chambers, were analyzed. The "ghost" clusters were identified later during the vertex search and rejected from the analysis (Sec. 3.2.2 p.41).

In the second step, every cluster is analyzed to get its position coordinate. The total charge Q is computed and then the maximum charge is compared to the other ones. In the most cases, odd clusters were fixed with 3 strips. In the other cases, even clusters were identified with 4 strips. During this stage in particular, one insured that starting from the strip with the maximum charge, the other charges decrease on both sides as typically shown in Fig. A.1.

As an example (Fig. A.2), less than 1 % of the clusters show a typical two-peak structure: these were interpreted as events where the particle was most probably accompanied by δ electrons produced before the interaction in the chamber. These events were removed from the final analysis.

Still at this stage, a special correction was added to those clusters where the strip with maximum charge was overloaded. This was the case for 5-10 % of the clusters and was mainly due to the low resolution of the flash ADCs used with the strips. For this purpose and using the remaining "good" clusters, one made the correlation of the maximum charge Q_2 to the quantity $(Q_1+Q_3)/Q_2$ which is simply the ratio of the charges from the two immediate neighbors to the maximum. The correlation plot between (Q_1+Q_3) and Q_2 is shown in figure A.3. These calibration coefficients were used to interpolate the real charge of the overloaded strips with maximum charge Q_2.

The final position was determined using the differential method [95]. For the x plane and for a 3 strips cluster it is given by:

$$X = X_0 + X^{(0)}.(1 + C.\frac{(Q_2 - Q_1).(Q_2 - Q_3)}{Q^2}) \tag{A.1}$$

where

$$X^{(0)} = \frac{a}{2}.\frac{Q_3 - Q_1}{2Q_2 - Q_1 - Q_3} \tag{A.2}$$

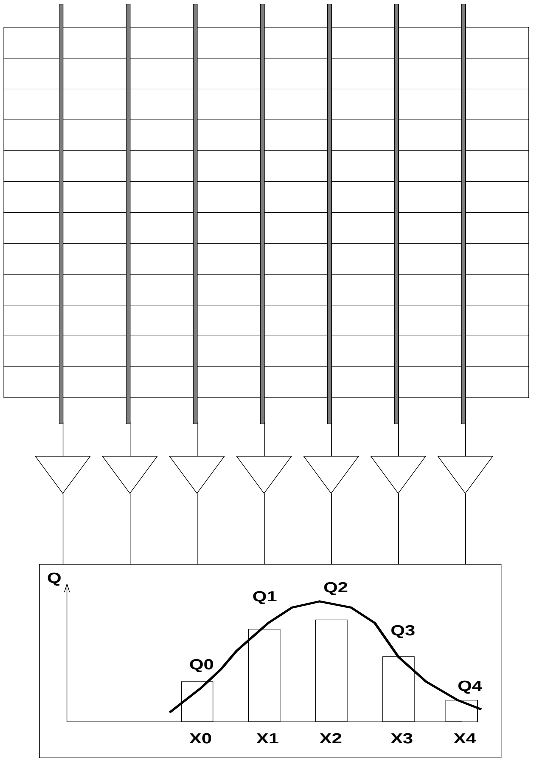

Figure A.1: *Schematic structure of a cluster of cathode strip charges after the search process where one has $Q_0 \leq Q_1 \leq Q_2$ and $Q_4 \leq Q_3 \leq Q_2$*

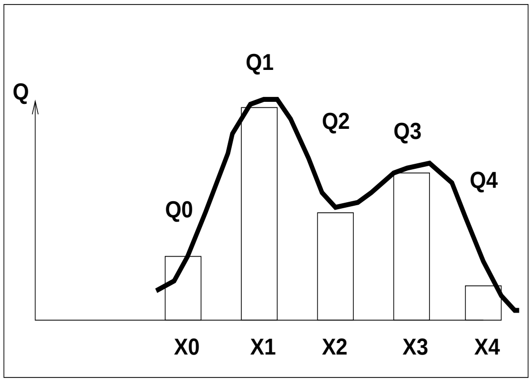

Figure A.2: *Typical cluster where the particle is accompanied by δ electrons*

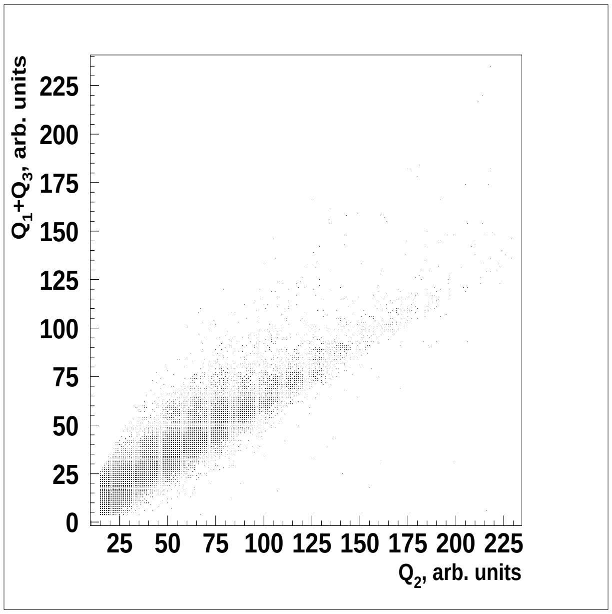

Figure A.3: *Correlation plot of $(Q_1 + Q_3)$ to Q_2 showing the regular relationship between these two quantities when there is no overload. If Q_2 exceeds the maximum charge allowed in the flash ADC while Q_1 and Q_3 are below, this property is used to find the right charge value.*

Here $Q = Q_1 + Q_2 + Q_3$, a is the cathode strip pitch[1] and X_0 is the coordinate of the strip center with maximum charge. In a differential method with 4 strips one has:

$$X = X_0 + X^{(0)}.(1 + C.\frac{(Q_2 - Q_4).(Q_3 - Q_1)}{Q^2}) \tag{A.3}$$

where

$$X^{(0)} = \frac{a}{2}.\frac{Q_3 + Q_4 - Q_1 - Q_2}{Q_2 + Q_3 - Q_1 - Q_4} \tag{A.4}$$

Here $Q = Q_1 + Q_2 + Q_3 + Q_4$ and X_0 is the coordinate between the strip with maximum charge and the immediate neighbor with the highest charge. The same formulae are used for the Y coordinate. C is a parameter depending on the geometry of the plane considered. Its value is adjusted by approaching the coordinate value obtained from the previous equations to the one obtained from a fit (induced method in Refs. [93, 94]). Several typical clusters were used to check the final value[2]. This method enables one to get the position with a precision of 150 μm.

---

[1] $a = ND_W$ where N is the number of cathode wires per strip and D_W is the distance between two wires (Fig. 2.8 p.25)

[2] Computations were also made for a partial set of the data using the induced charge method ([94],[95]) which is based on a more complete formalism but consumes much more computing time. One noticed a negligeable difference in the final position values and no valuable increase in the precision.

Appendix B

Error determination on θ_S and t

The scattering angle $\theta_S \equiv \theta$ is given by:

$$\theta = \sqrt{\theta_x^2 + \theta_y^2} \tag{B.1}$$

where the plane angles are determined from:

$$\theta_x = \theta_{x,out} - \theta_{x,in} \tag{B.2}$$

$$\theta_y = \theta_{y,out} - \theta_{y,in} \tag{B.3}$$

where the subscripts in and out refer to the incident and scattered tracks respectively. These input and output angles are related to the different coordinates x_i and y_i where i=1,2,3,4 refer to the chamber number as:

$$\theta_{x,in} = \arctan\left(\frac{x_2 - x_1}{z_{2x} - z_{1x}}\right) \tag{B.4}$$

$$\theta_{x,out} = \arctan\left(\frac{x_4 - x_3}{z_{4x} - z_{3x}}\right) \tag{B.5}$$

$$\theta_{y,in} = \arctan\left(\frac{y_2 - y_1}{z_{2y} - z_{1y}}\right) \tag{B.6}$$

$$\theta_{y,out} = \arctan\left(\frac{y_4 - y_3}{z_{4y} - z_{3y}}\right) \tag{B.7}$$

For a chamber i, z_{ix} and z_{iy} refer to the z position of the X and Y coordinates planes respectively. We had $z_{2x} - z_{1x} = 196.9cm$, $z_{4x} - z_{3x} = 209.7cm$, $z_{2y} - z_{1y} = 196.9cm$ and $z_{4y} - z_{3y} = 228.8cm$. According to the error propagation formula on the variable $\theta = f(\theta_x, \theta_y)$ [73] :

$$(\Delta\theta)^2 = \left(\frac{\partial f}{\partial \theta_x}\right)^2 (\Delta\theta_x)^2 + \left(\frac{\partial f}{\partial \theta_y}\right)^2 (\Delta\theta_y)^2 \tag{B.8}$$

where we have neglected the covariance term. The corresponding random variables have a gaussian probability density distribution and the quantities $\Delta\theta$, $\Delta\theta_x$ and $\Delta\theta_y$ refer to the full width at half maximum (FWHM) of those distributions. The 'FWHM error' Δi can then be related to the variance or 'rms error' σ_i (i=θ, θ_x, θ_y) by $\Delta i = 2.36\sigma_i$.

From Eq. B.1 one has :

$$\frac{\partial f}{\partial \theta_x} = \frac{1}{2}\left(\theta_x^2 + \theta_y^2\right)^{-1/2} 2\theta_x = \frac{\theta_x}{\theta}$$

and similarly :

$$\frac{\partial f}{\partial \theta_y} = \frac{\theta_y}{\theta}$$

Then the expression of $\Delta\theta$ becomes :

$$\Delta\theta = \frac{\left(\theta_x^2 \Delta\theta_x^2 + \theta_y^2 \Delta\theta_y^2\right)^{1/2}}{\theta} \tag{B.9}$$

From Eqs. B.2 and B.3 one has :

$$\Delta\theta_x = \{(\Delta\theta_{x,out})^2 + (\Delta\theta_{x,in})^2\}^{1/2} \tag{B.10}$$

$$\Delta\theta_y = \{(\Delta\theta_{y,out})^2 + (\Delta\theta_{y,in})^2\}^{1/2} \tag{B.11}$$

From Eq. B.4 and taking $\tan\theta \simeq \theta$ for $\theta \ll 1$ one has :

$$\begin{aligned}\left(\frac{\Delta\theta_{x,in}}{\theta_{x,in}}\right)^2 &= \left(\frac{\Delta(x_2 - x_1)}{x_2 - x_1}\right)^2 + \left(\frac{\Delta(z_{2x} - z_{1x})}{z_{2x} - z_{1x}}\right)^2 \\ &= \frac{(\Delta x_2)^2 + (\Delta x_1)^2}{(x_2 - x_1)^2} + \frac{(\Delta z_{2x})^2 + (\Delta z_{1x})^2}{(z_{2x} - z_{1x})^2}\end{aligned}$$

Taking now :

$$\Delta x_i = \Delta x \simeq 0.15mm \tag{B.12}$$

$$\Delta y_i = \Delta y \simeq 0.15mm \tag{B.13}$$

$$\Delta z_{ix} = \Delta z_{iy} = \Delta z \simeq 5mm \tag{B.14}$$

for i=1,2,3,4 one has then :

$$\Delta\theta_{x,in} = \sqrt{2}\theta_{x,in}\left(\frac{(\Delta x)^2}{(x_2 - x_1)^2} + \frac{(\Delta z)^2}{(z_{2x} - z_{1x})^2}\right)^{1/2} \tag{B.15}$$

$$\Delta\theta_{x,out} = \sqrt{2}\theta_{x,out}\left(\frac{(\Delta x)^2}{(x_4 - x_3)^2} + \frac{(\Delta z)^2}{(z_{4x} - z_{3x})^2}\right)^{1/2} \tag{B.16}$$

$$\Delta\theta_{y,in} = \sqrt{2}\theta_{y,in}\left(\frac{(\Delta y)^2}{(y_2 - y_1)^2} + \frac{(\Delta z)^2}{(z_{2y} - z_{1y})^2}\right)^{1/2} \tag{B.17}$$

$$\Delta\theta_{y,out} = \sqrt{2}\theta_{y,out}\left(\frac{(\Delta y)^2}{(y_4 - y_3)^2} + \frac{(\Delta z)^2}{(z_{4y} - z_{3y})^2}\right)^{1/2} \tag{B.18}$$

The absolute and relative errors are displayed in figure B.1 function of the scattering angle and the transfered momentum squared -t.

The error on the variable t was determined by linear interpolation for some θ typical values. A typical value at $\theta \simeq 1.17°$ with the worst precision $\Delta\theta/\theta \simeq 0.87\%$ gives $-t \simeq 0.0407 \pm 0.0007 (GeV/c)^2$ i. e. $|\Delta t/t| \simeq 1.87\%$. The cross section being determined by statistical evaluation in a serie of $[t_1, t_2]$ intervals for the central value $t_c = (t_1 + t_2)/2$, the maximum absolute error on the latter was estimated to be $0.001 (GeV/c)^2$ and taken for all the experimental points.

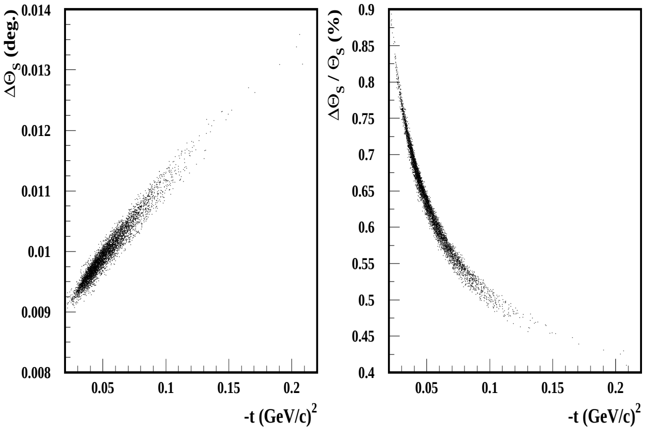

Figure B.1: *Absolute and relative experimental scattering angle errors versus the momentum transfered squared*$-t$.

Appendix C

Data acquisition

C.1 Electronics scheme

The signals from the counters (Fig. C.1) are processed to get the energy amplitude and time-of-flight information. The start for all TDC modules is produced from a coincidence between S1 and the STR (start) which is issued by the control unit CU (Sec. C.2 p.106). The logic signals are used to form the first level trigger which stands for a "beam event".

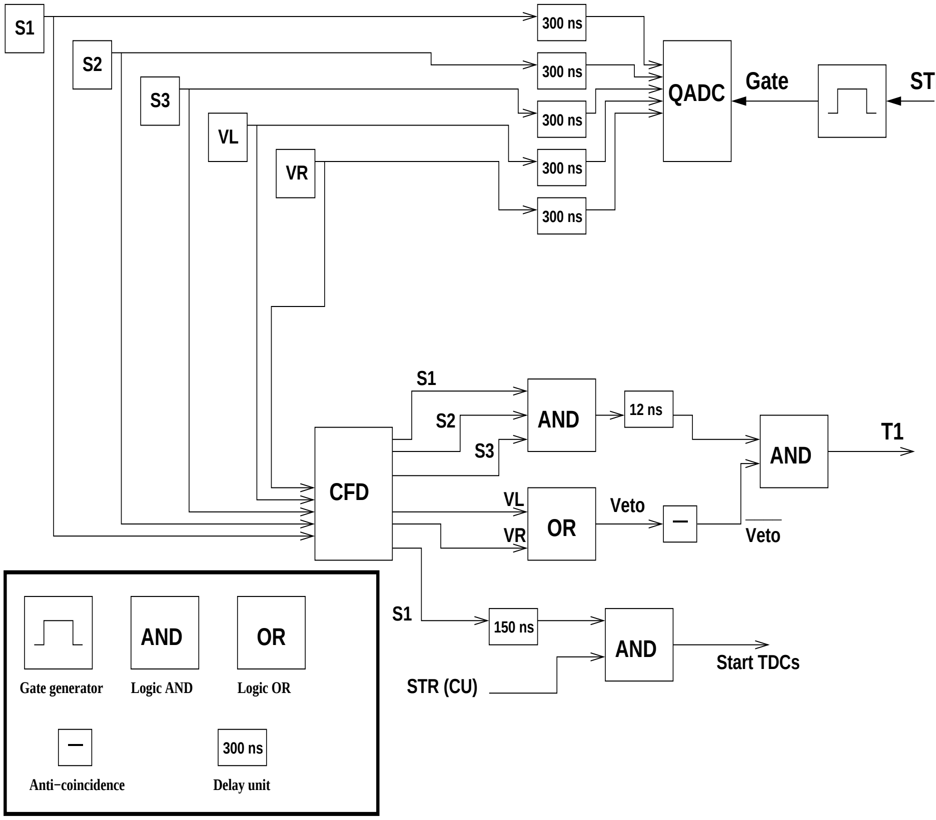

Figure C.1: *Electronic scheme showing the different lines from S1, S2, S3 and the veto (right VR and left VL) connected to a charge amplitude-to-digital converter (QADC). The same lines are sent to a constant fraction discriminator (CFD) unit and then to a time-to-digital converter (TDC) unit (not shown). The first level trigger signal T1 was used by the control unit (CU) for further processing.*

The energy signals from the anode planes of the chambers P5 and P6 (Fig. C.2) are used to record the charge amplitude and to produce logic signals through a leading edge discriminator (LED). The logic lines from the LED are used to produce the second level trigger T2 which signals the recoil particle passage. The "window anode" (WA) is a gate produced systematically from the STR (start CU). As an example, the signal P5X is produced from a coincidence of the anode signal AX5 and the gate WA. The coincidence of the four planes determines the passage of a recoil particle.

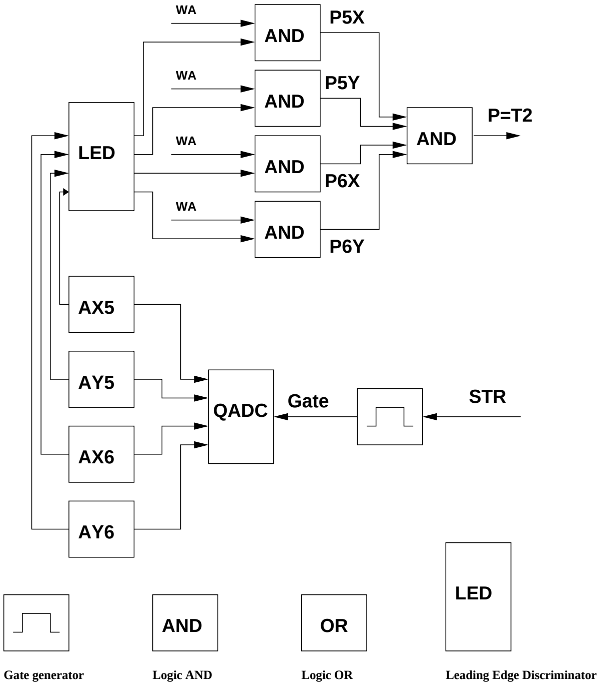

Figure C.2: *The MWPCs P5 and P6 electronic scheme - Second level trigger*

The rates of the most useful logic signals were recorded by a set of CAMAC scalers which are simply counting modules reset after each event cycle (Tab. C.1). The first set is called "real-time" and corresponds to the real incident rate reduced of course by the intrinsic dead time of either the corresponding detector or the electronic channel. The other set is called "live-time" and corresponds to what can be really treated by the DAQ system. Most of these signals were presented in this section while the other will be introduced in the section C.2.

These statistics were very helpful in order to optimize the DAQ system efficiency, i. e. to have a high recorded events rate for a given incident flux. In other words, the parameters (incident beam rate, gate widths, ...) are set in order to have the lowest DAQ dead time.

C.2 Electronics processing

In addition to the so called "real event" which is used to study the scattering, two other types of events were used (Tab. C.2). The "test event" was used to gather online calibration information for the MWPCs and pedestal information for all the QADCs while the "prescaled event" was registered to help to determine the total number of incident beam particles used in the cross section calculation. Every event type was identified by a specific pattern register. For every event type, the data cycle is explained in the next sections.

C.2.1 Real event cycle

The data processing logic for a real event is managed through a dedicated control unit (CU) shown schematically in figure C.3. The different inputs (resp. outputs) shown in red (resp. black) on the left (resp. right) side.

After having received a T1 signal it produces a 'busy' window W1 of about $2.5\mu s$ (Fig. C.4). Before that, the CU was inhibited (INH) during $3.6\mu s$, long enough to prevent any likely pile up event.

Name	Function	RT	LT
Timer	Clock generator	●	●
S1	S1 counter	●	●
S2	S2 counter	●	●
S3	S3 counter	●	●
B1	S1 $\bigwedge$ S2	●	●
B	S1 $\bigwedge$ S2 $\bigwedge$ S3	●	●
VL	Left veto counter	●	●
VR	Right veto counter	●	●
Veto	VL $\bigwedge$ VR	●	●
T1≡Beam	B $\bigwedge$ anti veto	●	●
Beam1	B1 $\bigwedge$ anti Veto	●	●
P5X	P5 X plane		●
P5Y	P5 Y plane		●
P6X	P6 X plane		●
P6Y	P6 Y plane		●
T2≡P	P5X $\bigwedge$ P5Y $\bigwedge$ P6X $\bigwedge$ P6Y		●
T1PS	T1 $\bigwedge$ P		●
Test	TEST event		●
LAM	Look At Me		●
STR	Start		●
EKR	Event Killed by Rationer		●

Table C.1: *List of real-time (RT) and/or live-time (LT) scalers. The symbol $\bigwedge$ is used for a logic AND meaning a time coincidence of the corresponding logic signals. In particular, T1 and T2 show respectively the rate of beam and scattering events.*

Event type	Contribution in %
Real Event	97.38
Test Event	0.12
Prescaled Event	2.50

Table C.2: *Contribution, in %, of different event types relative to the total event number.*

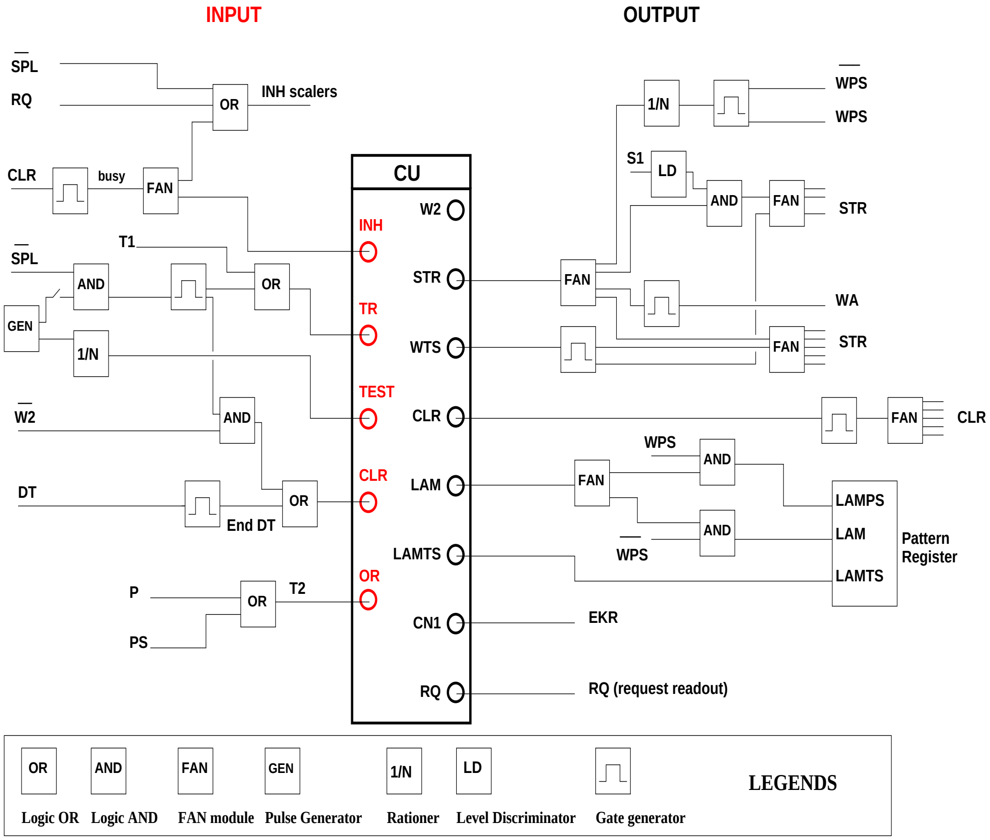

Figure C.3: *General scheme of the control unit (CU) showing the different input (in red) and generated logic signals*

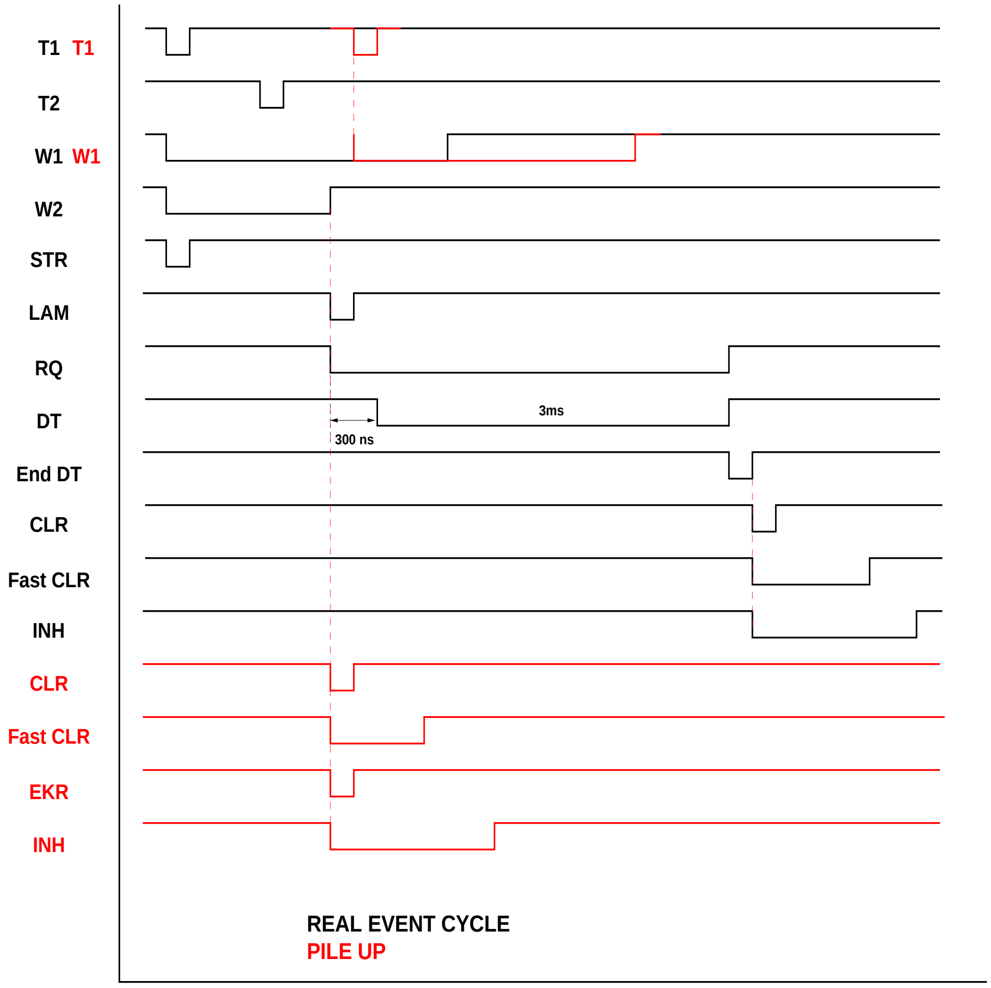

Figure C.4: *A real event chronogram together with a pile up event*

A 'working' window W2 of about $1.8\mu s$ is produced; the system is then expecting to receive a possible second level trigger T2 pulse. The W2 window appears only if W1 was triggered by a valid candidate T1 event; a pile up event or a test event will not produce it. One start (STR) is then issued which serves to initialize some modules and to produce some specific pulses; as an example the ARM signal needed for the Fastbus QADCs (Sec. C.2.4) is produced from the STR pulse. A LAM (Look At Me) is generated which will define the event pattern register, an RQ (Register of Question) window is opened and sent to the DAQ main trigger module (TM). The CU is then busy for data readout and no other event can be accepted. The main trigger module issues a dead time (DT) of about 3 ms for the data readout. After the readout of all the channels has been achieved an 'End DT' pulse is produced by a gate generator and sent to the CLR input of the CU. A CLR (20ns) and a 'fast CLR' (125ns) are sent to initialize all the modules. The CU is inhibited and then the system is ready for the next cycle. This event type is called 'real event' in the next sections. If no T2 appears during W2 time gate a CLR is immediately generated and from that point the cycle follows the same steps as the previous case.

If after a first T1 is received another T1 (pile up event) comes within the time window W1, it produces another similar window. The precedent T1 is refused and no second W2 window is generated. A fast CLR is generated after the first W2 which clears the system for another cycle. One EKR (Event Killed by Rationer) pulse is issued and counted for further use.

In conclusion, one can affirm that the DAQ system efficiency depends on the relative rates of the number of start events N_{STR} and events killed by rationer N_{EKR}. The monitor $N_{STR} - N_{EKR}$ being the number of events truly recorded, the optimization procedure needs to fix a beam rate for which the ratio $(N_{STR} - N_{EKR})/N_{STR}$ is maximal.

C.2.2 Test event cycle

These are special events for the MWPCs calibration purposes (Sec. 2.3.1.4 p.26) and also used to monitor the pedestal peak position for about 500 QADC channels. A clock generator triggers the TEST input of the CU at a frequency of 10/64 Hz and then the CU TS flip flop switches from state 1 to 0 (Fig. C.5). It will switch back to state 1 when all the test cycle is achieved.

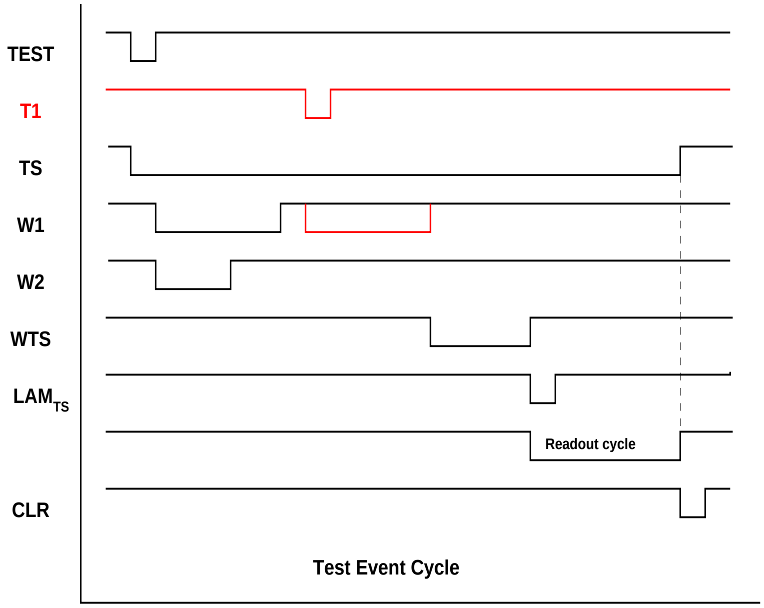

Figure C.5: *Test event cycle*

The CU waits for any current W2 gate to end than is enabled (Enable Test : ETS). This trigger disables the production of a W2 window for any next real event which means that the system is disabled to receive any. If another T1 comes within ETS, W1 is still issued[1]. The CU test module waits then its end to generate a WTS window of about $1\mu s$. A start STR signal is produced and a LAM_{TS} is sent from the CU to the pattern register module. The system follows then the same procedure as for a real event data cycle.

C.2.3 Prescaled event cycle (PS)

These were a partial set of the data generated only by the beam trigger, recorded every $k_{PS} = 2^{15}$ real events. The checking and the determination of several quantities by requiring a direct beam condition is obvious in such an experiment. The logic follows the same procedure as the test event since one works with only one trigger level with the window WPS and the LAM_{PS} signal.

The total number of beam particles

First, the total number of prescaled events is determined by integrating the ^{A}He energy peak from the counter S2 (and S1 for comparison). In the case of ^{6}He, due to the overlap with the ^{9}Li component this procedure induces errors and yields 34695 ± 135 (0.39% relative uncertainty) and 7200 ± 12 (0.17%) for the full and empty target runs respectively. Despite the low statistics in the empty target run, the errors are lower because the ^{9}Li is much rarer and thus less disturbing. These numbers are simply amplified by the factor k_{PS} in order to get the corresponding total number of particles.

C.2.4 Fastbus system

The time of flight (TOF) and amplitude data information from the two scintillator walls were digitized by fastbus modules Lecroy 1875 TDCs and 1885F QDCs respectively. The readout of the data needed four basic signals as shown in figure C.6. The Arm (60 ns width) signal enables the TDC modules. All the analog (amplitude) pulses are expected within a Gate of about 990 ns. The digital (TOF) pulses which play the role of start signals, are expected within a window of about 630 ns closed by a common Stop (100 ns width) signal. After the data conversion and readout by the main DAQ processor (VME type), a Clear signal resets the system.

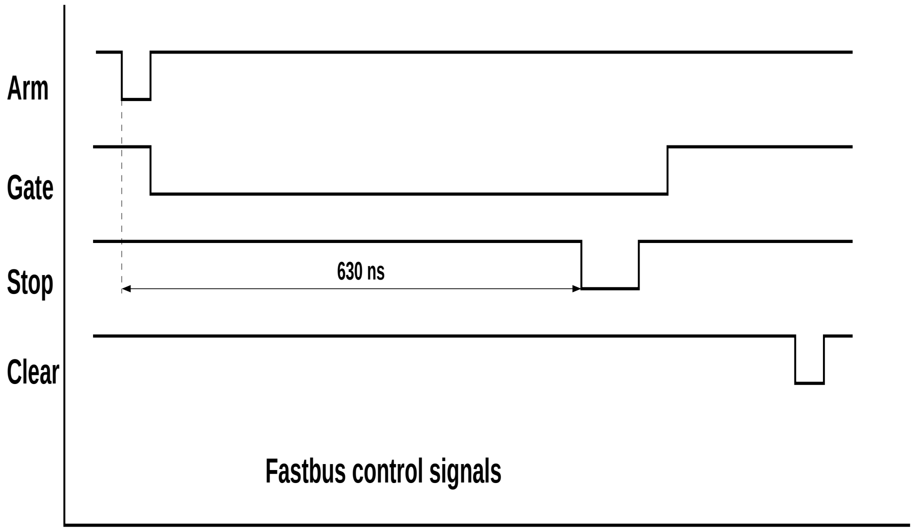

Figure C.6: *Timing diagram for the fastbus control signals*

---

[1] W1 cannot be disabled by any signal. It is always produced when a T1 pulse is in the CU trigger (TR) input

Appendix D

An overview of the Glauber-Sitenko theory

The high particle interactions are of a diffraction nature (see e. g. Chap. 4 of reference [61]). In order for the diffraction phenomenon to occur, the colliding particles relative motion wavelength must be shorter than the interaction length. The interpretation of the collision depends primarily on the relative incident energy and on the colliding particles.

In the case of the interaction of a nucleon with medium and heavy nuclei, the diffraction nature appears for energies in the order of or higher than 10 MeV. For such energies, the nucleon free path in the nuclear matter is much shorter than the nuclear dimension and the nucleus can be treated as an absorbing black body. The diffraction nuclear phenomena are then described in the same manner as one does in optical diffraction. In a higher energy regime, the free path in the nuclear matter becomes comparable with the nucleus dimension. The latter is then regarded as an optically semi-transparent body. At sufficiently high nucleon energies for which the incident nucleon wavelength is much shorter than the nucleon-nucleon interaction range, the scattering by the nucleus must be considered as multiple diffraction scattering by individual nucleons.

The general theory of high-energy diffraction nuclear processes involving composite particles was developed by Glauber [6, 77, 96, 97] and independently by Sitenko and its applications can be found in the review papers [98, 99, 100, 101, 102]. The multiple scattering Glauber theory enables, at high energies, to link in an unambiguous way the nuclear matter density distribution to the elastic differential cross section. Beside the proton-nucleus elastic scattering [6], one can also describe the inelastic and breakup processes [6, 103, 104]. For the actual work, we will reduce ourselves to the description of the proton-nucleus elastic scattering where the differential cross section is defined as :

$$\frac{d\sigma_{el}}{d\Omega} =\mid F_{el}(\mathbf{q}) \mid^2 \tag{D.1}$$

where $\mid F_{el}(\mathbf{q}) \mid$ denotes the p-nucleus elastic scattering amplitude and $\mathbf{q}$ being the transfered momentum vector

$$\mathbf{q} = \mathbf{q}_i - \mathbf{q}_f \tag{D.2}$$

between the initial and final projectile particle momenta vectors. In the case of an elastic scattering $\mid \mathbf{q}_i \mid=\mid \mathbf{q}_f \mid= \hbar k$ ($\hbar = h/2\pi$, h is the Planck constant and k is the projectile's incident wave number in the two particles CM system), the module q can be expressed as :

$$q = 2k\sin(\theta/2) \tag{D.3}$$

where θ is the CM scattering angle. The differential cross section can be expressed in terms of the second

Mandelstam invariant[1],[2] $-t = q^2$ as:

$$\frac{d\sigma}{dt} = \frac{\pi}{k^2}\frac{d\sigma}{d\Omega} \tag{D.4}$$

The scattering amplitude is given by:

$$F(\mathbf{q}) = \frac{ik}{2\pi}\int e^{i\mathbf{q}.\mathbf{b}}\left\{1 - \prod_{i=1}^{A}\left[1 - \gamma_{pN}(\mathbf{b} - \mathbf{s}_i)\right]\right\}\rho_A(\mathbf{r}_i)d^3\mathbf{r}_1 d^3\mathbf{r}_2 ... d^3\mathbf{r}_A d^2\mathbf{b} \tag{D.5}$$

also known as the Glauber combination law for the profile functions.

$\mathbf{b}$ is the impact vector which lies in the plane perpendicular to the projectile's direction

$\gamma_{pN}(\mathbf{b} - \mathbf{s}_i)$ are the profile functions for the pairwise pN (proton-nucleon, N=p, n) interactions

$\mathbf{s}_i$ i=1, 2, ..., A, are the transverse nucleons coordinates (projections of the nucleons vector positions $\mathbf{r}_i$ on the plane perpendicular to the projectile's direction)

$\rho_A(\mathbf{r}_i) \equiv \rho_A(\mathbf{r}_1, \mathbf{r}_2, ..., \mathbf{r}_A)$ is the nuclear many-body density

D.1 Nucleon-nucleon profile functions

The incident proton is a free particle thus its wave function (noted wf) can be associated to a plane wave $e^{i\mathbf{q}.\mathbf{r}}$ as shown in figure D.1.

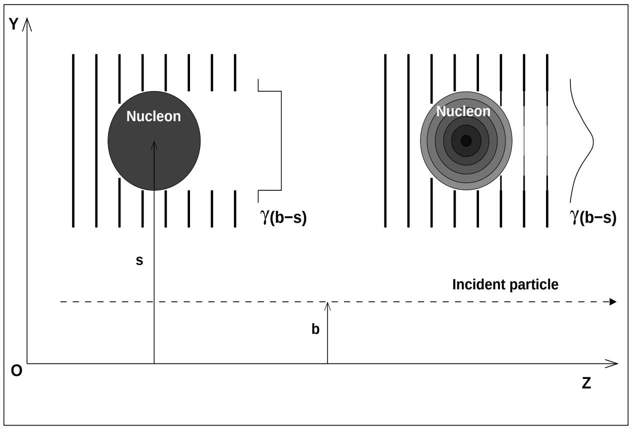

Figure D.1: *Scattering of a free particle with impact parameter b on a given nucleon located at s from the incident trajectory. The incident plane wave function (wf) is symbolized by parallel lines whose thickness show the amplitude. The nucleon profile function $\gamma(b - s)$ describes how this amplitude is attenuated. Two schematic cases are considered: first (left), the nucleon is a black box which absorbs completely the incident wf and second (right), the nucleon has a continuous matter distribution increasing from the periphery to the center. In the latter case, the profile function is a continuous function with a maximum at the center of the nucleon.*

The z-axis passes at the center-of-mass (CM) of the target nucleus ${}^A_Z X$ and is parallel to the direction of the incident proton. For a given target nucleon i, located at $\mathbf{s}_i$, the pN profile function $\gamma_{pN}(\mathbf{b} - \mathbf{s}_i)$ might be understood as a measure of the continuous absorption of the projectile wf amplitude. By 'continuous' absorption, one means that it varies continuously from the far periphery to the center of the target nucleon. By contrast, one may imagine the extreme case of a 'black sphere' target nucleon of a radius r_n where the absorption is null for $\mid \mathbf{b} - \mathbf{s}_i \mid \leq r_n$ and uniform elsewhere; γ_{pN} is then similar to a rectangular function.

The profile function $\gamma_{pN}(\mathbf{b})$ can be related to the corresponding pN scattering amplitude $f_{pN}(\mathbf{q})$ by the following equation:

$$\gamma_{pN}(\mathbf{b}) = \frac{1}{2\pi ik}\int e^{i\mathbf{q}.\mathbf{b}} f_{pN}(\mathbf{q}) d^2\mathbf{q} \tag{D.6}$$

---

[1] Since we deal here only with elastic scattering, we will remove from now on the subscript 'el'

[2] One uses generally the convention c=ℏ=1

where the integration is carried out in the plane perpendicular to the z-axis. According to the Glauber idea, the interaction of high energy protons from nuclei can be described using the information on the free nucleons scattering. In principle, the nucleon-nucleon (NN) scattering operator is a sum of few terms each one taking into account a specific effect occuring during the interaction, e. g. spin dependence and charge exchange processes [6]. Only the scalar parts of the pN scattering amplitudes were considered. At high energy, they are parametrized as:

$$f_{pN}(\mathbf{q}) = \frac{ik}{4\pi}\sigma_{pN}(1 - i\varepsilon_{pN})e^{-q^2\beta_{pN}/2} \tag{D.7}$$

σ_{pN} is the total pp (pn) elastic cross section

$\varepsilon_{pN} = \frac{Re[f_{pN}(0)]}{Im[f_{pN}(0)]}$ is the ratio of real to imaginary part of the forward pp (pn) scattering amplitude

β_{pN} are known as the slope parameters

For the purpose to make simple calculations, the parameters σ_{pN}, ε_{pN} and β_{pN} were calculated from interpolations of those values determined from a phase shift analysis (PSA) [105]. The interpolation used a sum of two gaussians and a second degree polynom and was performed in the energy range [0.2 - 1] GeV [106]. For q=0, the amplitude imaginary part is related to the total interaction cross section (optical limit theorem) as:

$$Im\left[f_{pN}(0)\right] = \frac{k}{4\pi}\sigma_{int} \tag{D.8}$$

Note

If one assumes for simplicity, spin and isospin amplitude independence, than one derives the following expression for the pN profile function:

$$\gamma_j(\mathbf{b}) = \frac{1}{ik}\int_0^\infty J_0(qb)f_j(q)S(q)qdq \tag{D.9}$$

where the formfactor $S(q)$ can be related to the matter distribution $\rho(r)$ as:

$$S(q) = 4\pi\int_0^\infty \rho(b)b^2\frac{\sin(qb)}{qb}db \tag{D.10}$$

D.2 Profile function Γ

In equation D.5, one can identify the profile function Γ as:

$$\Gamma(\mathbf{b}, \mathbf{r}_1, \mathbf{r}_2, ..., \mathbf{r}_A) = 1 - \prod_{i=1}^{A}\left[1 - \gamma_{pN}(\mathbf{b} - \mathbf{s}_i)\right] \tag{D.11}$$

which is originally defined as:

$$\Gamma(\mathbf{b}, \mathbf{r}_1, \mathbf{r}_2, ..., \mathbf{r}_A) = 1 - \exp^{i\chi(\mathbf{b}, \mathbf{r}_1, \mathbf{r}_2, ..., \mathbf{r}_A)} \tag{D.12}$$

where the total eikonal phase χ is the sum of phases due to scattering of individual nucleons:

$$\chi(\mathbf{b}, \mathbf{r}_1, \mathbf{r}_2, ..., \mathbf{r}_A) = \sum_{i=1}^{A}\chi_i(\mathbf{b} - \mathbf{s}_i) \tag{D.13}$$

One has then:

$$\gamma_i(\mathbf{b}) = 1 - \exp^{i\chi_i(\mathbf{b})} \tag{D.14}$$

The two-particle phase shift $\chi_i(\mathbf{b})$ for a scattering due to a potential $U_i(\mathbf{r}_i)$ is given by:

$$\chi_i(\mathbf{b}) = -\frac{1}{\hbar v}\int_{-\infty}^{+\infty} U_i(\mathbf{b}, z)dz \tag{D.15}$$

When the A-fold product in equation D.11 is expanded in powers of γ, it gives a scattering serie of A terms corresponding to single scattering, double scattering ... and so on, which were all taken into account. This multiple scattering serie does not include rescattering terms i. e. the scattering on the same nucleon more than once which contribution might be neglegted at high energy.

D.3 The Coulomb interaction

The Coulomb interaction is characterized by long-range forces, then its influence is important at higher impact parameter values and correspondingly, to lower values of θ and t. On the other hand, around 1 GeV/u, the real part of the pN strong interaction amplitude is negative which means repulsive forces; the two interactions interfere constructively which results in filling the diffraction minima [6].

One assumes [107] that the pp phase shift is a sum of a purely strong and Coulomb phase shifts:

$$\chi_p(\mathbf{b}) = \chi_p^{(S)}(\mathbf{b}) + \chi_p^{(C)}(\mathbf{b}) \tag{D.16}$$

where the Coulomb phase shift $\chi_p^{(C)}(\mathbf{b})$ may be calculated using equation D.15 with the Coulom pp potential. In our calculation we used, for simplicity, another equivalent approach which supposes that the total nuclear phase shift is the phase shift produced by the strong interaction alone and the shift caused by the interaction with the "averaged" nuclear Coulomb field. The exact analytical formulation may be found in references [6, 106].

D.4 Density corrections

The nucleons are assumed free (large inter-nucleon distance approximation) and fixed (sudden or adiabatic approximation) during the collision. This basic assumptions lead to inconsistencies between the calculated and the experimental differential elastic cross sections for the high momentum transfer, in particular for light systems like the ^4He nucleus [6]. The final cross sections might need corrections taking into account the nucleon correlations due to pairing or some other clusterization effects and certainly for the center-of-mass (CM) correlations.

Systematic uncertainties from the model input parameters

The total cross sections σ_{pN} and the real to imaginary ratios ε_{pN} are deduced from previous experimental works and are then known with relative uncertainties of 2% and 5% respectively. The parameter β is fixed by requiring $R_m(^4He) = 1.49\ fm$. The resulting cross sections and matter radii have then systematic uncertainties that one must estimate. This study was already performed in the range $-t \leq 0.05(GeV/c)^2$ [106] and shows that the uncertainties are expected to be less for $-t \geq 0.05(GeV/c)^2$. In this study, the variation of the cross section $\frac{d\sigma}{dt}$ was studied by varying the different parameters by 10% (see Fig. II.C.3 p. 23 in Ref. [106]). It was found that varying σ_{pN} by 10% induces a variation of 7% on $\frac{d\sigma}{dt}$ and that this effect is linear in the whole t range: this means that a global change of 1.4% is expected in the differential cross section when taking into account the experimental uncertainty of 2% in σ_{pN}.